Three-dimensional structure of the Na$^+$/H$^+$ antiporter from *Methanococcus jannaschii*.

Dissertation
Zur Erlangung des Doktorgrades
der Naturwissenschften

vorgelegt beim Fachbereich 14
Biochemie,Chemie und Pharmazie
der Johann Wolfgang Goethe Universität
in Frankfurt am Main

Von

Panchali Goswami

aus Guwahati, Indien

Frankfurt am Main 2009
(D30)

Die Arbeit wurde in der Abteilung Structurbiologie des Max-Planck-Instituts für Biophysik in Frankfurt am Main durchgeführt und vom Fachbereich Biochemie, Chemie und Pharmazie der Johann Wolfgang Goethe Universität als Dissertation angenommen.

Dekan: Prof. Dr. Dieter Steinhilber

1. Gutachter: Prof. Dr. Robert Tampé

2. Gutachter: Prof. Dr. Werner Kühlbrandt

Datum der Disputation: 10/06/2009

Table of contents

Abbreviations

Appendix

Curriculum Vitae

Acknowledgements

Abstract

Na$^+$/H$^+$ antiporters are ubiquitous membrane proteins involved in ion homeostasis and pH sensing. The amino acid sequence of one such antiporter, MjNhaP1, from *Methanococcus jannaschii*, shows a significant homology to eukaryotic sodium proton exchangers like NHE1 from *Homo sapiens* and SOS1 of *Arabidopsis thaliana* than to the well-characterized *Escherichia coli* NhaA or NhaB. MjNhaP1 shows activity at acidic pH unlike NhaA, which is active at basic pH. 13 transmembrane helices have been predicted to be present in NhaP1. A projection map, calculated by Cryo-EM of 2D crystals of MjNhaP1 grown at pH 4, showed it to be a dimer containing elongated densities in the centre of the dimer and a cluster of density peaks on either side of the dimer core (Vinothkumar et al., 2005). Incubation of 2D crystals at pH 8 on the EM grid resulted in well-defined conformational changes, clearly evident in a difference map as a major change in density distribution within the helix bundle (Vinothkumar et al., 2005).

The aim of this dissertation is to understand the working mechanism of MjNhaP1 by determining its three-dimensional structure. The aim was initially approached by structure determination by X-ray crystallography. The limitation for this method was the low expression yield, which was 0.5–0.7mg/ml (Vinothkumar et al., 2005). After various optimization trials, the expression yield of the recombinant protein could be elevated to 2-2.5mg of pure protein per litre of culture by the method of autoinduction (Studier et al., 2005). To obtain well diffracting 3D crystals, purification conditions (Vinothkumar et al., 2005) were modified. 3D crystals were obtained under various conditions, which has so far not diffracted X-Ray beyond 8Å.

Parallely, optimization of parameters (Vinothkumar et al., 2005) for 2D crystals formation was carried out. A combination of 1% DDM used for lipid solubilization, and 1% OG in the buffer of the purified protein produced 1-2 μm wide tubular 2D crystals of NhaP1. This batch of crystal proved to be the optimal for data collection at higher tilt angle with the electron microscope. A 3D map showed p22$_1$2$_1$ symmetry and revealed a tight dimer with an oval shape. The region in the central part of the dimer is composed of several tilted helices forming an interface between both monomers. On either side of the dimer interface, a group of six tightly packed helices form a bundle. This bundle contains three straight helices in the centre of the monomer and three helices in the periphery. Comparison of the structures of *E.coli* NhaA and *M. jannaschii* NhaP1 show substantial differences in length and slope of corresponding

helices between both antiporters. A 3D model of NhaP1 based on the 3D map revealed 13 helices, which has been named as A-M to distinguish it from the NhaA helices. Overlaying the X-ray structure onto the 3D map revealed that the disrupted helices IV and XI of NhaA superimpose two central helices at similar position in the 3D map of NhaP1. The disrupted helices IV and XI in the X-ray structure of NhaA have been proposed as the putative ion-binding and translocation site (Hunte C et al, 2005; Arkin IT et al, 2007; Screpanti & Hunte (2007). This motif appears to be present also in NhaP1, as suggested by the close fit of NhaA helices IV and XI on the putative helices E and L of the NhaP1 model. These two putative helices E and L in NhaP1 contain the highly conserved TDP and GPRVVP motif, which are crucial for antiporter activity (Hellmer et al., 2002, Hellmer et al., 2003). In the overlay, helix V of NhaA containing the two essential, conserved aspartates D163 and D164 fits the density of the putative helix F of NhaP1, which contains the conserved motif FNDP. The homologous D161 in the FNDP motif of NhaP1 is essential for transport activity as show by mutagenesis (Hellmer at al., 2003).

Significant differences are visible in the region of the dimer interface of the 3D map of NhaP1 occupied by helices VI, VII, and VIII in NhaA. This region shows an extra helical density (A) in the 3D map of NhaP1. By alignment of MjNhaP1 sequence with the amino acid sequences of several Na^{+}/H^{+} exchangers, it was evident that the additional helix (A) is located in the N terminus of NhaP1. In our sequence alignment, a putative hydrophobic segment corresponding to this additional helix A is present in other archaeal and eukaryotic antiporters but not in any of the bacterial ones. The N-terminus of the human Na^{+}/H^{+} exchanger NHE1 has been predicted to contain a highly hydrophobic signal peptide. This indicates the probability of the N-terminal helix A of NhaP1 to be an uncleaved signal peptide. Besides being a signal sequence targeting NhaP1 to the membrane, the map suggests that this helix might be involved in the formation of dimer contacts between both monomers.

A gene duplication event is evident in the 3D map of NhaP1, as not only the helices D, E, F and K, L, M are related by an inverted repeat but also the helices B, C and I, J are related. We present here the three-dimensional architecture of a Na^{+}/H^{+} antiporter from archaea. The presence of the 13th helix suggests the location of the N-terminus to be located in the cytosol and the C-terminus in the periplasm. This would orient NhaP1 in an inverted manner in the membrane in comparison to NhaA. Further structural information at higher resolution and biochemical and biophysical investigations are required to confirm the topology.

7

Zusammenfassung

Die Einstellung und Aufrechterhaltung des Gleichgewichts von Na^+-Ionen und Protonen wird bei lebenden Zellen - sowohl bei Pflanzen als auch bei Tieren und Mikroorganismen – hauptsächlich über Na^+/H^+ Austauscher gewährleistet. Na^+-Ionen und Protonen sind in Physiologie und Bioenergetik von lebensnotwendiger Bedeutung. Es wird davon ausgegangen, dass Na^+/H^+ Austauscher pH Sensoren besitzen, die bei Änderung des intrazellulären pH-Wertes die Austauschaktivität regulieren. Zudem leisten sie einen erheblichen Anteil bei der Regulation des Natriumflusses und des Zell-Volumens nach osmotisch bedingtem Zellschrumpfen (Pavel, 1998). Zusätzlich zu ihrer physiologischen Bedeutung sind eukaryotische Na^+/H^+ Austauscher ein wichtiges Angriffsziel für Medikamente, da sie in Pathologie und bei menschlichen Krankheiten eine entscheidende Rolle spielen. Beispielsweise konnte in einer Studie gezeigt werden, dass die Verabreichung von Cariporiden, einem Hemmstoff des menschlichen Na^+/H^+ Austauschers NHE1, nach dem Einsetzen eines Koronararterien-Bypasses eine signifikante Reduktion von Myokardinfarkten zur Folge hatte (Mentzer et al., 2003). Na^+/H^+ Austauscher ermöglichen Prokaryoten eine gewisse Salztoleranz und das Wachstum bei extremen pH-Werten, da Mikroorganismen ständig wechselnden Umweltbedingungen ausgesetzt sind (Padan, 2005).

Erste Einblicke in die Struktur von Na^+/H^+ Austauschern gingen aus der dreidimensionalen Elektronendichtekarte des *Escherichia coli* Austauschers NhaA hervor, welche über Elektronenkristallographie erhalten wurde (Williams, 2000). Es konnte gezeigt werden, dass NhaA 12 Transmembransegmente (TMS) besitzt und in der Lipidumgebung der 2D Kristalle ein Dimer bildet. Die später erhaltene Röntgenstruktur der inaktiven Konformation von NhaA bei pH 4,0 zeigte eine bislang einzigartige Faltung (Hunte et al., 2005): Die TMS IV und XI bestehen jeweils aus zwei halben Helices, die mit einem kurzen ungewundenem Abschnitt verbunden sind Diese unterbrochenen Helices kreuzen sich in der Mitte der Membran in entgegengesetzter Richtung. Allgemein ist die Insertion von polaren Helix-Termini energetisch ungünstig, da dieser Zustand eine Ladungskompensation benötigt und damit als ideal betrachtet wird, um Ionen anzuziehen und zu binden (Toyoshima et al., 2000),(Dutzler et al., 2002),(Yernool et al., 2004),(Hunte et al., 2005),(Yamashita et al., 2005).

Sequenzvergleiche haben gezeigt, dass MjNhaP1, der Na$^+$/H$^+$ Austauscher von *Methanocaldococcus jannaschii* eine Sequenzähnlichkeit von nur 10-16% zu dem *E. coli* NhaA besitzt, jedoch 18-21% zu den eukaryotischen Proteinen wie SOS1 (*Arabidopsis thaliana*) und NHE1 (*Homo sapiens*) (Hellmer et al., 2002). Die Aktivierung von MjNhaP1 erfolgt zwischen pH 6 und 7, eine Eigenschaft, die es mit dem menschlichen NHE1 teilt (Hellmer et al., 2002). Im Gegensatz dazu ist NhaA aus *E. coli* bei einem pH-Wert von über 7 aktiv, jedoch nicht bei niedrigerem pH (Padan et al., 2001). Die über Elektronenkristallographie erhaltene Projektionskarte von MjNhaP1 zeigt, dass das Protein in 2D Kristallen als Dimer vorliegt und dass innerhalb eines Monomers zwischen zwei Bereichen unterschieden werden kann - einem zentralen Bereich mit überwiegend verlängerten Dichten, die die Dimerisierungsfläche bilden und einem zentralen Cluster von vier bis sechs Dichten auf beiden Seiten des zentralen Kerns (Vinothkumar et al., 2005). Um die Auswirkung des pH-Wertes auf MjNhaP1 zu untersuchen, wurden elektronenmikroskopische Daten von 2D Kristallen gesammelt, die bei pH 4,0 und pH 8,0 inkubiert wurden. Aus den Daten wurde eine Differenzdichtekarte gezeichnet, die eine Reorientierung der Dichten im äußeren Helix-Bündel zeigte. Damit wurde belegt, dass Konformationsänderungen in MjNhaP1 pH-induziert hervorgerufen werden (Vinothkumar et al., 2005).

Für das Verständnis des Na$^+$/H$^+$ Austausches sind weitere strukturelle Informationen verschiedener Konformationen notwendig. Zudem kann das konservierte Muster der funktional wichtigen Faltung besser verstanden werden, wenn strukturelle und funktionelle Informationen homologer Proteine aus unterschiedlichen Domänen vorliegt. Folglich ist das Ziel der vorliegenden Dissertation die Bestimmung der dreidimensionalen Struktur des archaealen Na$^+$/H$^+$ Austauschers MjNhaP.

Das Gen Mj0057, welches das MjNhaP1 aus *Methanocaldococcus jannaschii* kodiert, wurde zur Expression mit einem C-terminalen His$_6$-tag in den Expressionsvektor pET26b kloniert (NhaP1$_{His}$) (Vinothkumar et al., 2005). Das bislang etablierte Protokoll zur heterologen Proteinexpression und Reinigung von MjNhaP ergab nur 0,5-0,7 mg reines Protein pro Liter Expressionskultur (Vinothkumar et al; 2005). Diese Menge war nicht ausreichend, um strukturelle Untersuchungen, insbesondere die 3D Kristallisation, durchzuführen. Aus diesem Grunde wurde die Proteinausbeute von NhaP1$_{His}$ durch Testen unterschiedlicher Parameter wie verschiedene Konstrukte, *E. coli* Stämme, Induktionszeitpunkte, Expressionstemperaturen, Menge an IPTG Induktorzugabe und Medien optimiert.

Die deutlichste Verbesserung wurde bei Zellen gefunden, die bei der Expression in Autoinduktionsmedium (AI) (Studier., 2005) gewachsen sind. NhaP1$_{His}$, das in AI exprimiert wurde, ergab schließlich 2-2,5 mg reines Protein pro Liter Kultur. Die Proteinreinigung erfolgte nach dem zuvor beschriebenen Protokoll mittels Ni^{2+}-NTA Affinitätschromatographie (Vinothkumar et al., 2005) mit folgenden Modifikationen: (a) Waschen der Membranen mit harnstoffhaltigem Puffer, (b) Verwendung eines größeren Volumens an Waschpuffer und (c) Verwendung eines ansteigenden Imidazolgradienten im Waschschritt zur Entfernung von Verunreinigungen.

3D Kristallisationsexperimente wurden mit monodispersem NhaP1$_{His}$ durchgeführt. 3D Kristalle wurden bei verschiedenen Bedingungen erhalten und Optimierungen dieser Bedingungen wurden mit unterschiedlichen Fällungsmittel wie Polyethylenglykolen und MPD bei variierenden Konzentrationen durchgeführt. Verschiedene Additive wurden eingesetzt, um die Kristallgröße und Form zu verbessern. Die Beugung der 3D Kristalle war jedoch nicht besser als 8Å.

Eine alternative Technik zur Strukturbestimmung von Membranproteinen ist die Cryo-Elektronenkristallographie. Diffraktionsmuster oder Bilder von 2D Kristallen, die sich durch Rekonstitution von gereinigtem Protein in einer nativen Lipidumgebung bilden, werden dabei bei verschiedenen Kippwinkeln aufgenommen. Eine 3D Rekonstruktion mittels der erhaltenen Daten gibt Informationen über die 3D Architektur des Proteins. NhaP1$_{His}$ formt tubuläre 2D Kristalle bei pH 4,0 (Vinothkumar et al., 2005). Diese Kristalle waren jedoch schmal und dadurch nur begrenzt für die Datenaufnahme geeignet. Es wurden intensive Versuche zur Optimierung der bestehenden Kristallisationsbedingungen durchgeführt. Protein, dass in Anwesenheit von 1,5% OG gereinigt wurde, ergab schließlilch tubuläre Kristalle von 0,8-1,0 µm Breite. Die Erniedrigung der Salzkonzentration von 200 auf 50 mM im Dialysepuffer führte zu einer Zunahme der Breite auf 1-1,5 µm. Diese 2D Kristalle eigneten sich am besten zur Datenaufnahme bei hohen Kippwinkeln. Für die Berechnung der 3D Mappe von MjNhaP1 wurden über 70 Bilder bei verschiedenen Kippwinkeln (0-45°) aufgenommen. Die Mappe zeigt eine p22121 Symmetrie. Wie bereits in der Projektionsmappe gezeigt wurde (Vinothkumar et al., 2005), bildet NhaP1$_{His}$ ein festes Dimer mit einer ovalen Form aus. Die Region im zentralen Teil des Dimers besteht aus unterschiedlich orientierten Helices, die eine Kontaktfläche der beiden Monomere ausbilden. Die weiter außen gelegene Region eines jeden Monomers wird durch ein Bündel von sechs dicht gepackten Helices gebildet, wobei drei aufrecht stehende Helices zentral liegen und weitere drei an der Außenseite.

Zum Verlgeich von *E. coli* NhaA und *M. jannaschii* MjNhaP1 wurde die Röntgenstruktur von NhaA mit der 3D Mappe von NhaP1$_{His}$ manuell überlagert. Während die zentralen Dimer-Kontaktflächen der Monomere gravierende Unterschiede zwischen den beiden Austauschern aufweisen, unterscheidet sich die außen gelegene Region mit dem Helix-Bündel hauptsächlich in der Länge und der Neigung der Helices. In der Region des äußeren Helixbündels mit den unterbrochenen Helices IV und XI von NhaA befinden sich ebenfalls zwei Helices von NhaP1$_{His}$ Signifikante Unterschiede werden in der Region der Dimer-Kontaktfläche deutlich, die eine - im Vergleich zu NhaA - zusätzliche Dichte zeigt.

Durch Sequenzvergleiche der Aminosäuresequenzen von MjNhaP1 und verschiedener Na$^+$/H$^+$ Austauschern wurde ersichtlich, dass die zusätzliche Helix am N-Terminus von NhaP1$_{His}$ lokalisiert ist. Um die Helixnummerierung von NhaP1$_{His}$ der von NhaA anzugleichen, wurde die zusätzliche Helix als Helix 0 bezeichnet. Die Sequenzvergleiche zeigen weiterhin, dass es auch bei anderen archaealen und eukaryotischen Transportern einen der Helix 0 ensprechenden hydrophoben Bereich gibt. In bakteriellen Na$^+$/H$^+$ Austauschern ist dieser Bereich hingegegen nicht vorhanden. Es wurde vorhergesagt, dass der N-Terminus des menschlichen Na$^+$/H$^+$ Austauschers NHE1 ein hydrophobes Signalpeptid enhält. Dies deutet darauf hin, dass die N-terminale Helix 0 von NhaP1$_{His}$ ein nicht-prozessiertes Signalpeptid sein könnte. Neben der Möglichkeit, dass diese Helix eine Signalsequenz ist, über die NhaP1 zur Membran geleitet wird, weist die 3D Mappe darauf hin, dass diese Helix and der Bildung des Dimerkontakts zwischen den beiden Monomeren involviert sein könnte. Eine höheraufgelöste Struktur und ergänzende biochemische Experimente sind vonnöten, um die Rolle der zusätzlichen Helix zu verstehen.

Die unterbrochenen Helices IV und XI von NhaA wurden als mögliche Ionen-Bindestellen und Ort der Translokation vorgeschlagen [(Hunte C et al, 2005; Arkin IT et al, 2007; Screpanti & Hunte (2007)]. Eine entprechende Anordnung scheint auch bei NhaP1 zu existieren, was durch eine Überlagerung dieser Helices IV und XI mit den entsprechenden Helices von NhaP1$_{His}$ ersichtlich ist. Die Helices IV und XI von NhaP1 enthalten die beiden hoch-konservierten TDP bzw. GPRVVP Motive. Mutationen von D132 des TDP und R347 des GPRVVP Motivs führen zu einem Verlust der Austauscheraktivität. Die Unterbrechung der Helices kann jedoch aufgrund der limitierten Auflösung in der z-Richtung nicht klar gezeigt werden, was auch der Fall bei der 3D Mappe von NhaA war (Williams 2000).

Die Überlagerung der Röntgenstruktur von NhaA mit der 3D Mappe von NhaP zeigt außerdem, dass Helix V von NhaA, welche die beiden essentiellen, konservierten Aspartate D163 und D164 enthält, mit der als Helix V bezeichneten Dichte von MjNhaP1, übereinstimmt. Diese Helix enthält das konservierte FNDP Motiv. Die Aspartate D163 und D164 dieser Helix wurden als wichtige Reste vorgeschlagen, welche an der Kontrolle des Zugangs und an einer Bindung beteiling sind. Auch das homologe D161 des FNDP Motivs von NhaP1 ist essentiell für die Transportaktivität, wie durch Mutationsstudien gezeigt wurde (Hellmer., 2003).

Die Helices III, IV und V von NhaA lassen sich mit den Helices X, XI und XII gut übereinanderlagern, was darauf schließen lässt, dass sie durch Gen-Duplikation entstanden sind. Eine vergleichende Analyse mit NhaP1 zeigt, dass wahrscheinlich auch NhaP1 durch solch eine Genduplikation entstanden ist. Bei NhaP1 stehen nicht nur die Helices III, IV und V mit X, XI und XII durch invertierte Wiederholung (*inverted repeats*) in Beziehung, sondern auch die Helices I und II mit VIII und IX. Ob gesagt werden kann, dass die Helices VI, VII und auch die Helix 0 durch Genduplikation enstanden ist, hängt von der Interpretation der 3D Mappe ab.

Wir zeigen hier die dreidimensionale Architektur eines Na$^+$/H$^+$ Austauschers aus einem Archaebakterium. Durch die dreizehnte Helix kann angenommen werden, dass der N-Terminus im Cytosol und der C-Terminus im Periplasma lokalisiert ist. Diese Anordnung lässt darauf schließen, dass NhaP1 im Vergleich zu NhaA,in entgegengesetzter Orientierung in die Membran eingebettet ist. Um die Topologie zu bestätigen sind weitere strukturelle Informationen mit besserer Auflösung und biochemischen und biophysikalischen Untersuchungen nötig.

1 Introduction

1.1 Biological membranes

The biological membrane is a hydrophobic film, which encloses the cell, forming its boundary and isolating it from the surrounding environment. The physical basis of spontaneous membrane formation is due to the propensity of hydrophobic moieties to self-associate and hydrophilic moieties to interact with an aqueous environment, thus enabling cells to isolate their internal constituents from the exterior. This formation of cellular compartments leads to segregation of biochemical reactions and their performance with high efficiency by restricting the dissemination of reaction products (Meer, 2008).

A wide variety of proteins and lipids form the biological membrane, making it a well-organized assembly. The relative proportion of lipids and protein differ greatly in different membranes. For example, myelin membrane is composed of ~80% lipid and ~20% protein whereas inner mitochondrial membrane contains ~75% protein and ~25% lipids (Jain, 1988). The bulk of lipid in the bilayer provides the environment for the hydrophobic membrane proteins. These deeply embedded proteins are termed intrinsic or integral membrane proteins. There exists another kind of proteins termed extrinsic or peripheral membrane proteins, which are associated with the exoplasmic or cytoplasmic leaflet of the bilayer. The contacts between integral membrane proteins and lipids are very tight to maintain the seal of the membrane as a permeability barrier (Luckey, 2008).

1.2 Membrane transport mechanisms

1.2.1 Membrane bioenergetics

One major role of biological membranes is controlled influx and efflux of substances in and out of a living cell. The hydrophobicity makes the membrane semi-permeable and allows only selective transport of substances across it. The thermodynamic function known as the Gibbs free energy difference (ΔG) whose value depends on the current state of the system, governs the spontaneity of solute transport across cell membranes. This free energy is associated with the concentration gradient of a solute across the membrane and is termed its chemical potential difference. Additionally, for a charged solute, an electrical potential difference or membrane

potential ($\Delta\Psi$) is also generated due to the charge difference on both sides of the membrane bilayer. Hence, an electrochemical gradient ($\Delta\bar{\mu}$) influences the distribution of charged metabolites, which usually exist in a cell as weak acids or bases [Equation (1)].

$$* \Delta G = RT \cdot \ln \frac{[A]_{in}}{[A]_{out}} + zAF \cdot \Delta\Psi \quad \text{[Equation (1)]}$$

According to the chemiosmotic hypothesis (Mitchell, 1966) the electrochemical potential of H$^+$ ($\Delta\bar{\mu}_{H+}$) is harnessed for the synthesis of ATP and powers transport processes across membranes. Another membrane linked currency for transport, like the $\Delta\bar{\mu}_{H+}$, is the Na$^+$ electro chemical gradient, $\Delta\bar{\mu}_{Na+}$. For example, anaerobic bacteria as *Propionigenium modestum*, *Malonomonas rubra*, and *Clostridium* (renamed Caloramator) *fervidus* rely exclusively on Na$^+$ ions for their energy metabolism (Dimroth and Hilbi, 1997; Speelmans et al., 1993; W. Hilpert, 1984)

1.2.2   Different types of membrane transport mechanisms

Membrane transport can be of two kinds: non-mediated and mediated. Non-mediated membrane transport or passive diffusion occurs by random molecular motion that results in the transfer of a substance across the membrane. A chemical potential gradient is the driving force for non-mediated flow of a substance through a membrane. Bulk solvent flow, membrane charge, and degree of hydrophobicity of the diffusion barrier affect the mechanism of this passive diffusion. However, very few molecules and polar ions can cross the phospholipids bilayer in this manner. Hence, the other type of membrane transport, mediated transport, employs specialized membrane proteins for transporting metabolites down or against its concentration gradient across the bilayer. Based on these criterions and the driving force of the transport processes it is possible to distinguish between passive and active transport.
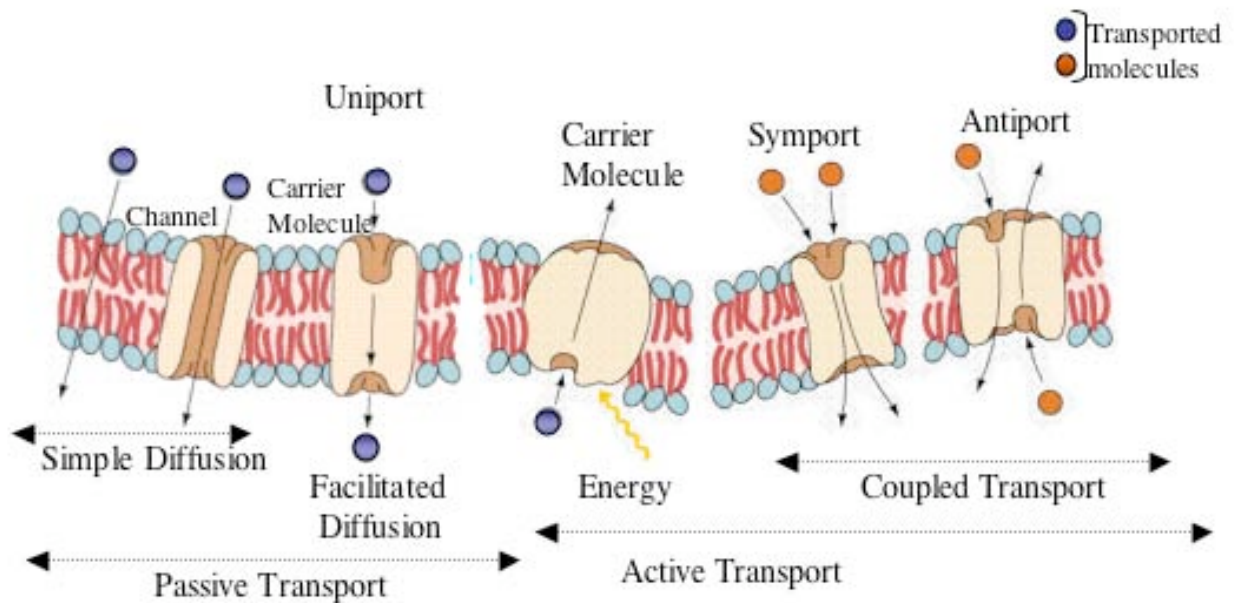
Figure 1 Schematic representation of the different transport systems across a lipid bilayer. The figure passive transport that occurs by simple or facilated diffusion and active transport where energy mediated transport occurs. [Image adapted from (Sadava, 2008)]

1.2.2.1   Passive transport

When transport of a solute across the bilayer occurs down its concentration and/or electrical gradient with no input of energy, the mechanism is known as passive transport. This kind of transport can take place by simple diffusion or facilitated diffusion via integral membrane proteins. A brief description of the different kinds of passive transport mechanisms is given below.

Ionophore

Ionophores are a diverse group of organic molecules that make the membrane permeable to ions. A class of ionophores known as carrier ionophores bind selectively to ions on one side of the membrane, and release them on the other side after diffusing through the hydrophobic bilayer. They return to the original side of the membrane to repeat the process. Ionophores are generally antibiotics of bacterial origin. Valinomycin, one of the best-characterized ionophoric antibiotics, is an example of a carrier ionophore that facilitates the passage of K^+ across membranes.

Another kind of ionophore known as channel ionophore forms transmembrane channels or pores for selective diffusion of ions.

Facilitated diffusion

In facilitated diffusion, the transport of a solute is mediated by its reversible combination with a carrier. This carrier–substrate complex shuttles between the inner and outer membrane leaflet releasing and binding the solute on either side. This kind of passive transport system is most effective when the cell is exposed to a fairly constant level of carrier substrate (Mueckler, 1994). The facilitative glucose transporters are the most thoroughly studied [reviewed in (Zhao and Keating, 2007)] facilitated diffusion transport system, which mediate the exchange of glucose between the blood and cytoplasm of the cell. Depending on the metabolic state of the cell as well as the organism facilitative glucose transporters may be involved in a net uptake or output of glucose from the cell.

Ion channels

Ion channels are characterized by a gating mechanism in response to stimuli, which open and close it. Ion channels in many cases are associated with diseases. A large number of medical drugs (1/3 of all marketed medicines), and animal and plant toxins target ion channels (Hille, 2001). Multifarious stimuli activate ion channels; ligands such as neurotransmitters, Ca^{2+} ions, and cAMP, mechanically by stretching the membrane, or electrically by changing the transmembrane voltage (Elinder et al., 2007). One such is the voltage gated Kv (K^+) channel which opens in response to the membrane potential and closes in a short time later through the action of a second gate that functions via a modified "ball-and-chain" mechanism (Armstrong, 1998).

1.2.2.2   Active transport

Active transporters couple solute transport to the input of energy (Csaky, 1965). Here, the movement of solute across a membrane against its concentration gradient or electric potential or both is a coupled chemical reaction. In most cases ATP-powered pumps or ATPases mediate "primary active transport" by deriving energy from ATP hydrolysis. The other type of active transport known as "Secondary active

transport" uses the energy stored in an electrochemical gradient generated by the ion-pumping ATPases.

ATP-Powered pumps

All ATP-powered pumps are transmembrane proteins with one or more binding sites for ATP located on the cytosolic side of the membrane. They hydrolyze ATP into ADP and Pi and transport ions or other molecules simultaneously. Therefore, the energy stored in the phosphoanhydride bond is not dissipated but rather used to move ions or other molecules against an electrochemical gradient. Different types of ATPases exist in nature. The well-studied P-type ATPases transport cationic calcium, sodium, potassium, copper across biological membrane through a reaction cycle that involves a covalent phosphorylated intermediate (Charnock JS, 1963; Post RL, 1965). They can also function as a "lipid flippase", like the erythrocyte Mg^{2+}-ATPase, by transferring lipids and maintaining lipid symmetry (Daleke, 2003). Another kind of ATPases known as V-ATPases is responsible for the acidification of intracellular compartments in eukaryotic cells (Forgac, 1998) and has been implicated in diseases like osteoporosis, renal acidosis and tumour metastasis. They are involved in proton translocation by hydrolyzing ATP. The largest class of ATPases commonly known as ABC transporters transport a wide variety of physiological substances. Certain foreign substances like pathogens, medication and drugs induce the expression of a definite class of ABC transporters known as multidrug resistance transporters (MDRs) in living cells.

Cotransporters or secondary transporters

Secondary transporters use the free energy stored in ion and/or solute gradients established by primary pumps to drive the transport of a solute across cytoplasmic or internal membranes of biological cells. This mechanism works by coupling the translocation of a solute to the translocation of one or more ions (H^+ or Na^+) that move down their own gradients, namely the proton motive force or Na^+ motive force, respectively. They are highly abundant and the amino acid sequences coding them are diverse. Secondary transporters are found for virtually every low molecular weight substance in nature (Sobczak and Lolkema, 2005). Cotransporters or secondary transporters are ascribed to an "alternative access mechanism" for

substrate translocation by which it is believed to have two alternating conformations (Figure 2E).

X-ray structures of several secondary transporters revealed different protein folds and molecular mechanisms. In the following section, a brief overview of some interesting structural features of various secondary transporters and their role in transport processes are discussed briefly.

1.3   Diverse structural folds and mechanisms of secondary transporters

The first information about the helix arrangement in a secondary transporter came from the 6Å electron microscopy map of the *E. coli* NhaA (Williams, 2000). It revealed 12 transmembrane helices arranged in two groups comprising of 6 helices each. However, high resolution structural information was available only after X-ray structure of the *E.coli* multidrug efflux transporter, AcrB, was solved (Murakami et al., 2002). It showed that the protein exists as a trimer with a periplasmic headpiece and a transmembrane part (Figure 2A). A pseudo-two-fold symmetry axis exists in each transmembrane domain, that is, the six N-terminal helices are symmetrically arranged with the six C-terminal helices. Three transmembrane α-helices, one from each protomer together forms a pore at the centre of the headpiece. The interface of the protomers contains three vestibules, which provides the pathway for the substrate to diffuse by way of lateral movement.

A different structural fold and evidence for the alternating access mechanism came with the structures of LacY (H$^+$/lactose symporter) and GlpT (glycerol-3-P-Pi exchanger) (Abramson et al., 2003a; Huang et al., 2003). Like AcrB, these transporters contained two homologous domains with six transmembrane segments. However, the tertiary structures are different from AcrB, indicating a different gene origin. The X-ray structure of mutant LacY showed a large hydrophillic cavity with substrate bound and facing the cytoplasm (Figure 2B). The periplasmic side was closed, suggesting one binding site that is alternately accessible to both sides of the membrane. The N and C terminal domains have a high degree of symmetry although very different sequences, suggesting that the domains arose by gene duplication. These two domains are linked to each other by a flexible loop and enclose the hydrophilic cavity. It appears that the structural changes between the outward and

inward facing conformation is mediated by rotation of the N- and C- terminal domain around the substrate binding site, thereby making the binding site accessible to each side of the membrane in an alternate manner (Abramson et al., 2003a).

The astonishing resolution of 1.35 Å of the trimeric ammonia transporter, AmtB, revealed a new motif with 11 transmembrane helices not homologous to any known membrane protein structure (Khademi et al., 2004). A quasi-two fold axis (up-to down) exists in the mid-plane of the membrane intersecting the threefold trimeric axis, which relates the transmembrane segment M1 to M5 and M6 to M10 (Figure 2C). Several membrane proteins like AmtB, GlpF and all aquaporins, the SecY protein of the translocon, and the ClC chloride channel show similar structural duplication with opposite polarity with respect to the membrane plane (Khademi et al., 2004). No significant overall conformational change of AmtB was revealed upon substrate binding. This is consistent with AmtB as a channel rather than as a transporter, which would harness alternating conformational states.

Another example of transporter versus channel comes from the glutamate transporter, Gltph, from the archaeon *Pyrococcus horikoshii* which harbours a gating mechanism mediated by two helical hairpins (Yernool et al., 2004). The helical hairpins form two re-entrant loops, which move to open and close access to the substrate-binding site. Pore-loops or re-entrant loops are commonly observed in other membrane proteins like potassium channel (Doyle et al., 1998) and members of the aquaporin family (Murata et al., 2000). Unlike AcrB, LacY and GlpT, Gltph has no internal homology within its eight transmembrane segments (Figure 2D).

Generally, integral membrane proteins are either α-helix bundles or β-barrel structures. In both cases, polar groups of the protein backbone are buried in the membrane and are saturated with internal hydrogen bonds, while non-polar side chains face the bilayer, resulting in thermodynamic stability of the membrane protein (White and Wimley, 1999). In principle, insertion of polar helix termini in the hydrophobic core is energetically unfavourable and such a motif needs to be stabilized by specific polar interactions (Screpanti and Hunte, 2007). However, there exists disrupted helices in certain membrane proteins where the helical structure is interrupted and the interjacent polypeptide chain forms an extended peptide in the middle of the membrane. The first case was revealed by the primary active transporter the Ca^{2+}-ATPase (Toyoshima et al., 2000) which contains a pair of parallel interrupted helices. This α-helical structural element was observed for four

secondary transporters: ClC H$^+$/Cl$^-$ exchanger from *E. coli* (Dutzler et al., 2002), Gltph, a eukaryotic glutamate transporter homologue (Yernool et al., 2004), LeuT$_{Aa}$, from *Aquifex aeolicus*, a bacterial homologue of Na$^+$/Cl$^-$-dependent neurotransmitter transporter (Yamashita et al., 2005) and NhaA, the main Na$^+$/H$^+$ exchanger of *E. coli* (Hunte et al., 2005a). In case of ClC H$^+$/Cl$^-$ exchanger and Glt$_{ph}$, the interrupted helices insert and exit the membrane bilayer at the same side acquiring a hairpin-like shape while in case of LeuT$_{Aa}$ and NhaA, they span the membrane from one side to the other.

Such unusual motifs are generally endowed with a functional role. The energetically unfavourable situation is either compensated by closely located amino acid residues with opposite charge or the partial charge may be exploited for ion attraction and binding. Since a Na$^+$/H$^+$ exchanger is subject of this PhD work, a detailed discussion of the functional implication of such a structural fold of secondary transporters will be given in a later part of this dissertation.
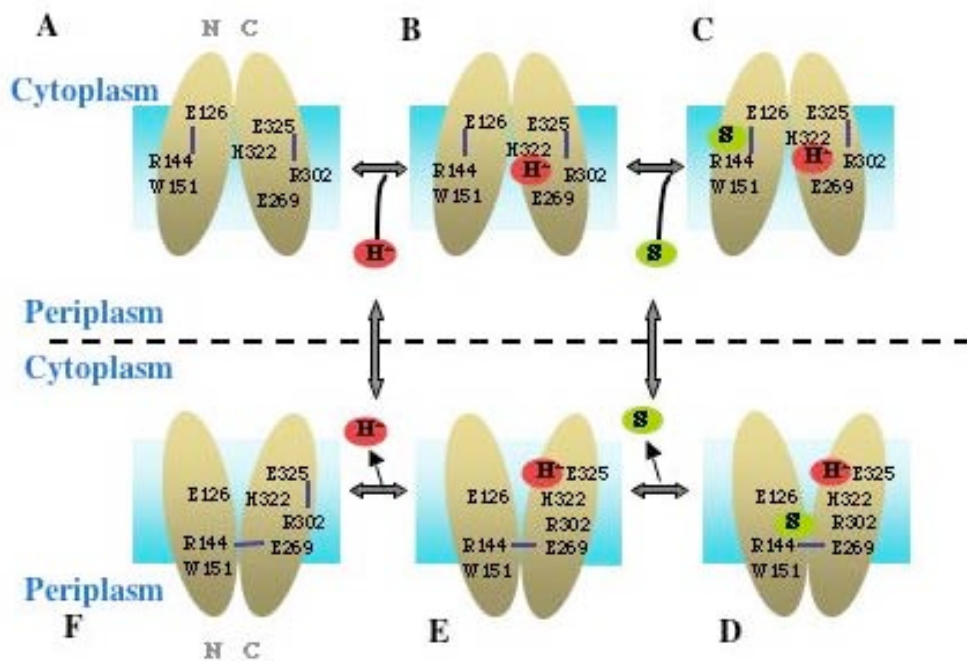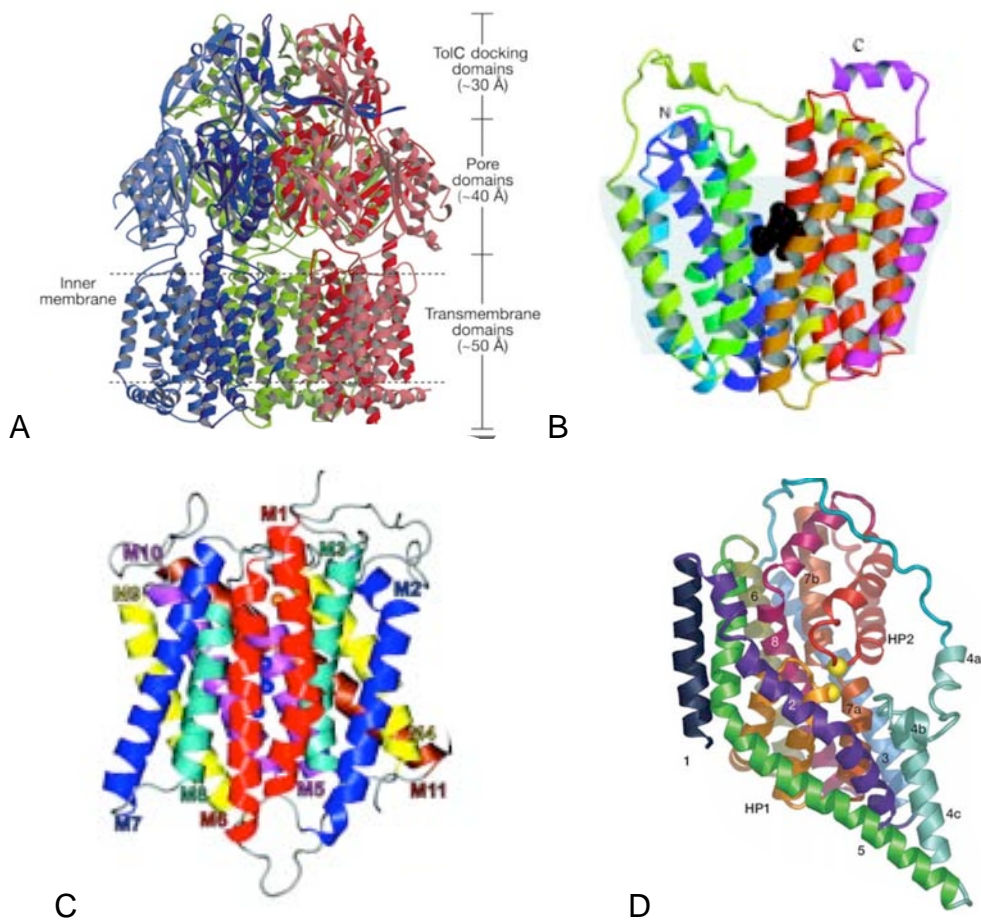
Figure 2   Structures of different type of secondary membrane transporters. Overall structures of A. AcrB (Murakami et al., 2002) B. LacY (Abramson et al., 2003b) C. AmtB (Khademi et al., 2004) D. Gltph (Yernool et al., 2004)   E.   A possible lactose/H$^+$ symport mechanism. Key residues are labeled and H-bonds are shown with blue lines. The H$^+$ and the substrate are shown in red and green circles [reproduced from (Abramson et al., 2003b)].

21

1.4   Na$^+$/H$^+$ exchangers

1.4.1   Functional role of Na$^+$/H$^+$ exchangers in living cell

Na$^+$ and H$^+$ are the most abundant ions in a living cell and they play a crucial role in different life processes. However, these ions can turn into potent stress factors if their concentration increases or decreases beyond a certain limit. In order to maintain a balance of these ions there exist a family of specialized membrane proteins called Na$^+$/H$^+$ exchangers. This exchange process couples the H$^+$ cycle and the Na$^+$ cycle operating in energy-transducing membranes (Skulachev, 1994). They were first reported by Mitchell and Moyle in *E.coli* and Brierley *et a*l. in mitochondria (Brierley, 1968; Mitchell, 1967; Mitchell, 1969).

Na$^+$/H$^+$ exchangers are ubiquitous and are indispensable in all domains of life, including animals, plants and microorganisms. Their physiological function varies depending on the cell type and surrounding environment. Higher eukaryotes contain a diverse repertoire of Na$^+$/H$^+$ exchangers (NHE) to regulate cytosolic pH. Na$^+$/H$^+$ exchangers protect eukaryotic cells from intracellular acidification and participate in regulation of sodium fluxes and cell volume after osmotic shrinkage (Pavel, 1998). Mammals such as *Homo sapiens* possess ten isoforms of Na$^+$/H$^+$ exchangers (NHE1-NHE10) in various tissues. The most predominant amongst these is the NHE1 isoform, which has several additional functions apart from pH regulation. It acts as an anchor that is involved in regulating cytoskeleton organization by binding several proteins in the plasma membrane where these proteins can interact functionally (Baumgartner et al., 2004). Besides these, NHE1 is required for normal cell growth, proliferation and differentiation (Wang, 1997).

In plants, soil salinity is a major abiotic stress for agriculture. Na$^+$ ions have adverse effects on K$^+$ nutrition, cytosolic enzyme activity, photosynthesis and metabolism. Three mechanisms function cooperatively to prevent the accumulation of Na$^+$ in the cytoplasm, i.e. restriction of Na$^+$ influx, active Na$^+$ efflux and compartmentation of Na$^+$ into the vacuole. The *Arabidopsis thaliana* AtNHX1 gene encodes a tonoplast Na$^+$/H$^+$ antiporter that functions in compartmentation of Na$^+$ into the vacuole. Overexpression of AtNHX1 has enhanced the salt tolerance of Arabidopsis plants (Apse et al., 1999).

Na$^+$/H$^+$ antiporters also play a crucial role in prokaryotes and are required for Na$^+$ tolerance and/or a capacity to grow at extreme pH (Padan, 2005). Bacteria grow in a wide range of pH, from pH1 in acidic sulphur springs to pH 11 in soda lakes, and

require a balanced cytoplasmic pH for optimal function and structural integrity of their cytoplasmic proteins. In bacteria, the proton motive force is converted into sodium gradients by Na^+/H^+ antiporters to drive energy-requiring processes like solute transport, movement of flagellar motors, transduce environmental signals into cell responses, and function in drug efflux (TetL and MdfA) (Krulwich et al., 2005). Like many other antiporters, Na^+/H^+ antiporters have also been implicated in virulence and/or epidemiology of pathogenic enterobacteria by affecting host and bacterial cell homeostasis (Padan, 2005) .

1.4.2   Classification of Na^+/H^+ exchangers

All Na^+/H^+ exchangers belong to the superfamily of monovalent cation/proton antiporters (CPA). This superfamily has three main subdivisions, named CPA1, CPA2 and NaT-DC (Na^+-transporting carboxylic acid decarboxylase) according to the nomenclature of the transport classification database established by Milton Saier (http://www.tcdb.org/). Each of these contains a unique set of ancestral prokaryotic genes. Although the CPA1 and CPA2 family have evolved and diversified in eukaryotes, only prokaryotic examples of the NaT-DC family are found. The CPA1 and CPA2 family are discussed below.

The CPA1 Family The CPA1 superfamily arose from ancestral NhaP genes in prokaryotes. NhaP mediates transport of Na^+ or Li^+ in exchange for H^+ in an electroneutral and pH dependent manner (Hamada et al., 2001; Hellmer et al., 2003). Sequences of members of the CPA1 family show that they vary in size. The bacterial proteins are generally 300-549 amino acids long while eukaryotic proteins are longer consisting of 541-894 residues. 10-13 putative transmembrane helices are predicted for these proteins (www.tcdb.org).
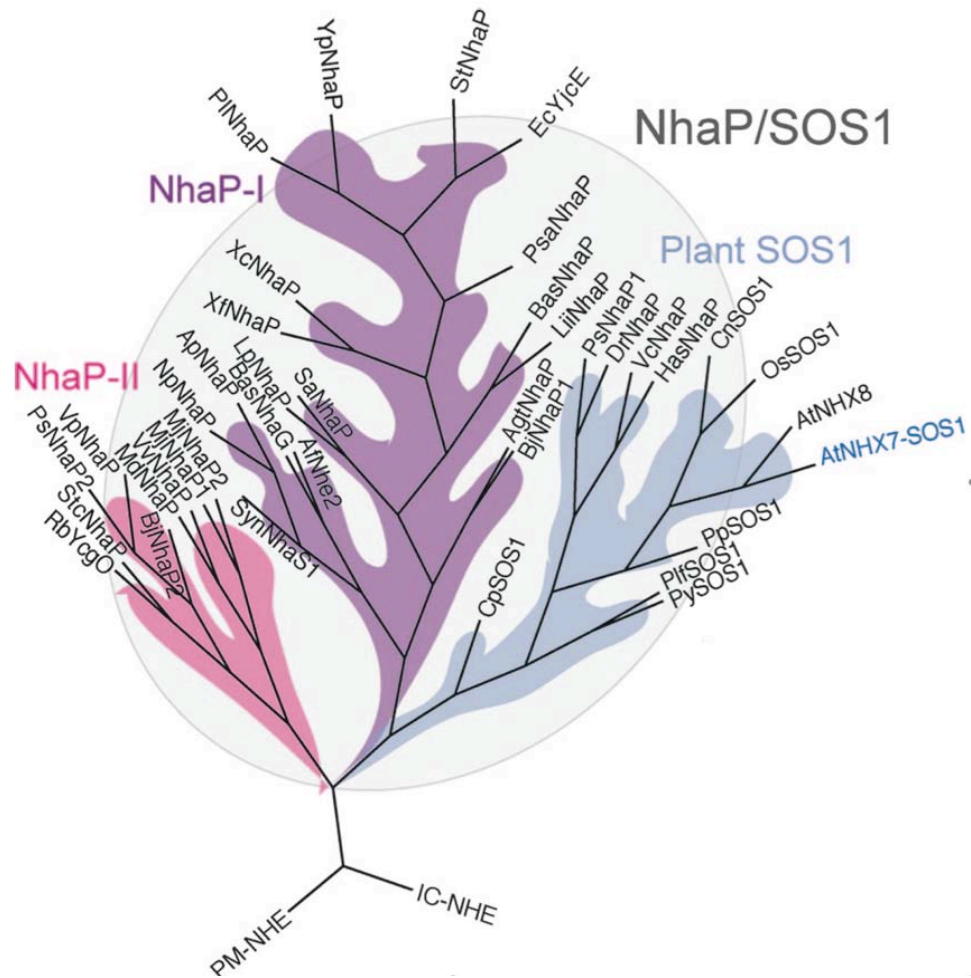
Figure 3 Phylogenetic tree of CPA1 transporters (Brett et al., 2005). Phylogenetic analysis was performed with 39 bacterial NhaP and eukaryotic SOS genes. The NhaP/SOS1 clade (shaded oval) is a CPA1 subfamily restricted to bacteria, protozoa, and plants and shows similarity to both Intracellular-NHE and Plasma membrane-NHE CPA1 subfamilies (indicated by lower 2 branches). It can be further divided into 3 clades: NhaP-I (shaded violet) and NhaP-II (shaded pink) gene clusters contain ancestral bacterial NHE genes, e.g. ApNhaP; and the plant SOS1 clade (shaded light purple) contains 8 plant and protozoan SOS1 genes, e.g. AtNHX7-SOS1 (blue text), as well as 4 related bacterial NhaP genes

The CPA1 family shows three principal clusters; proteins derived exclusively from animals form one cluster, the second includes all bacterial homologues and the third cluster includes one from *Arabidopsis thaliana*, one from *Homo sapiens* and two (*S. cerevisiae* and *S. pombe*) (www.tcdb.org). Multiple paralogs exist for many organisms; for example, *C. elegans has* seven and five are known for humans. Most of these paralogs have related sequences, and they belong to the animal specific

clusters. The generalized transport reaction catalyzed by functionally characterized members of the CPA1 family is (www.tcdb.org):

$$Na_{out}^+ + H_{in}^+ \rightleftharpoons Na_{in}^+ + H_{out}^+$$
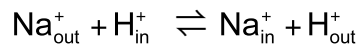
The CPA2 Family This is a large family with representatives from bacteria, archaea and eukaryotes. The CPA2 family comprises several clades, each consisting of a prokaryotic members that share common origins with some plant and animal homologs (Brett et al., 2005). CPA2 is broadly divided into NHA and CHX clades. The NHA family of related genes in animals are related to fungal NHA1 and these are likely to be Na^+, K^+/H^+ exchangers. There are two paralogs, NHA1 and NHA2 that exist in all completely sequenced metazoan genomes (Brett et al., 2005). The CHX clade consists of *E.coli* KefB and KefC which are the closest bacterial homologs of an uncharacterized cluster of plant genes (Brett et al., 2005). The CPA2 family is also represented by the the well-characterized bacterial NhaA antiporters, including *E.coli* NhaA, which are major contributors to NaCl tolerance in many bacterial species and perform electrogenic (n+1)H+/nNa+ exchange (Padan and Schuldiner, 1994).The proteins of the CPA2 family consist of between 333 and 900 amino acid residues. They exhibit 10-14 transmembrane α -helical segments (TMSs). The generalized transport reaction catalyzed by members of the CPA2 family is (www.tcdb.org):

$$M_{in}^+ + nH_{out}^+ \rightleftharpoons M_{out}^+ + nH_{in}^+$$
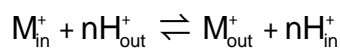
This is referred to as the carrier-mediated mode.

Some members may also catalyze: $M_{in}^+ \rightleftharpoons M_{out}^+$. This is refered to as the channel-mediated mode.
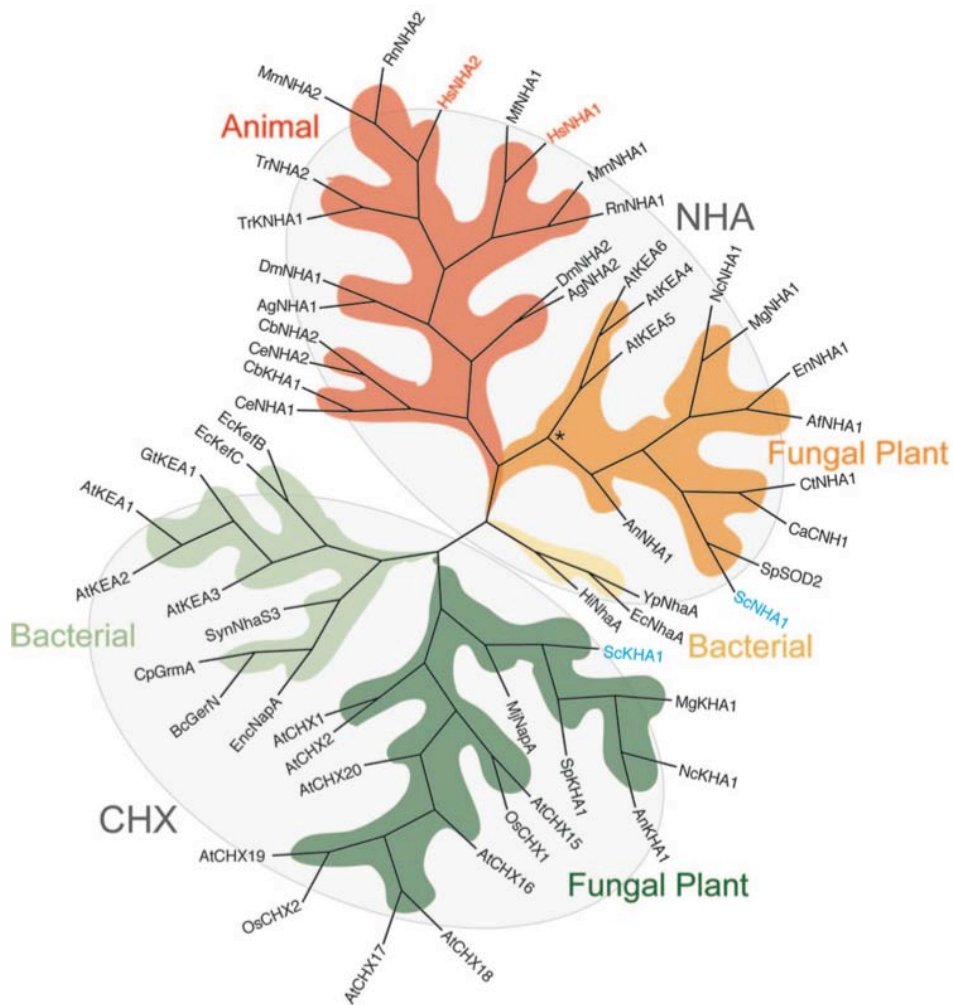
Figure 4 Phylogenetic tree of CPA2 transporters (Brett et al., 2005). The phylogenetic relationships between 58 representative CPA2 genes are shown in this unrooted phylogram. The CPA2 gene family is subdivided into 2 subfamilies: the NHA (top shaded circle) and CHX (bottom shaded circle) clades. The CHX clade has origins in the bacterial NapA and KefB K^+/H^+ transporter genes, which are highlighted in light green. The fungal and plant CHX gene clade is highlighted in dark green. The NHA subfamily has origins in bacterial NhaA genes (shown in light yellow). Fungal NHA genes including ScNHA1 (blue text) cluster with, but show low similarity to, plant AtKEA4–AtKEA6 genes; these are highlighted in dark yellow. The newly identified animal NHA clade is shown in light red and includes 2 genes from all animal species studied, including HsNHA1 and HsNHA2 (red text).

1.4.3   The model system of Na^+/H^+ antiporter, *E.coli* NhaA

E.coli NhaA is the best-characterized Na^+/H^+ antiporter so far. West and Mitchell first provided the evidence for the existence of a Na^+/H^+ antiporter in *E.coli* by describing the effect of Na^+ on the pH gradient in everted vesicles (West and Mitchell, 1974). In the *E.coli* genome two genes *nhaA* and *nhaB* were identified (E. Pinner, 1993; Padan

et al., 1989). NhaA is the main antiporter that is required to support growth at high Na$^+$ concentration (0.9M, pH7.0) and tolerate high pH in presence of Na$^+$ (0.7M, pH8.5) (Etana Padan, 1989). The expression level of NhaA in the cell is regulated by Na$^+$ and Li$^+$ concentration in the environment (Karpel et al., 1991; Rahav-Manor et al., 1992). NhaA has therefore a Na$^+$ (and Li$^+$) specific regulatory network where intracellular Na$^+$ rather than extracellular Na$^+$ is the inductive signal (Dover et al., 1996) . A positive regulator of NhaA is NhaR, encoded by a gene (*nhaR*) mapped downstream of NhaA (Rahav-Manor et al., 1992). *nhaR* is induced by Na$^+$ and the inductions is increased with pH ((Carmel et al., 1997; Padan et al., 1989; Rahav-Manor et al., 1992) . NhaA is also positively regulated by H-NS (Dover et al., 1996), a DNA binding protein and a global regulator involved in salt stress in bacteria (Dersch et al., 1993; Higgins et al., 1988; Ussery et al., 1994). The regulatory mechanism of NhaA is thus an interplay between Na$^+$, H-NS and NhaR (Rahav-Manor et al., 1992) .

The activity of NhaA is dramatically affected by pH (Gerchman et al., 1993; Gerchman et al., 1999; Taglicht, 1991). This is essential for cytoplasmic pH regulation, and is a property common to many other prokaryotic and eukaryotic antiporters. NhaA becomes inactive at acidic pH and changes its V$_{max}$ dramatically, by over three orders of magnitude, upon a shift to alkaline pH, reaching a maximal level at pH 8.5. Hence, NhaA is thought to have amino acids acting as "pH sensors" that transduce the pH signal into a change in activity. Several steps are expected to be involved in the pH response of the antiporter, raising the question as to whether the amino acid residues involved in the various steps are identical, overlapping or different from the ones that are involved in the translocation of the ions. Studies by monoclonal antibodies, fluorescent probe and trypsin accessibility tests have shown that the protein undergoes a conformational change in response to pH (Rothman et al., 1997; Venturi et al., 2000) .

Cryo-electron crystallography of 2D crystals of *E. coli* NhaA provided the first structural evidence that the protein exist as a dimer (Williams et al., 1999). A three-dimensional map of these 2D crystals discerned the presence of 12 transmembrane helices and gave insight about the helix packing (Williams, 2000). A X-ray structure of acidic pH-downregulated NhaA was determined at 3.5Å resolution which opened avenues of a detailed understanding of the working mechanism of this antiporter (Hunte et al., 2005a). The X-ray structure revealed an unique fold (Hunte et al., 2005b): the TMSs IV and XI exist as pairs of half helices connected by short

stretches of non-helical peptides. These disrupted helices cross each other in the middle of the membrane in opposite directions.
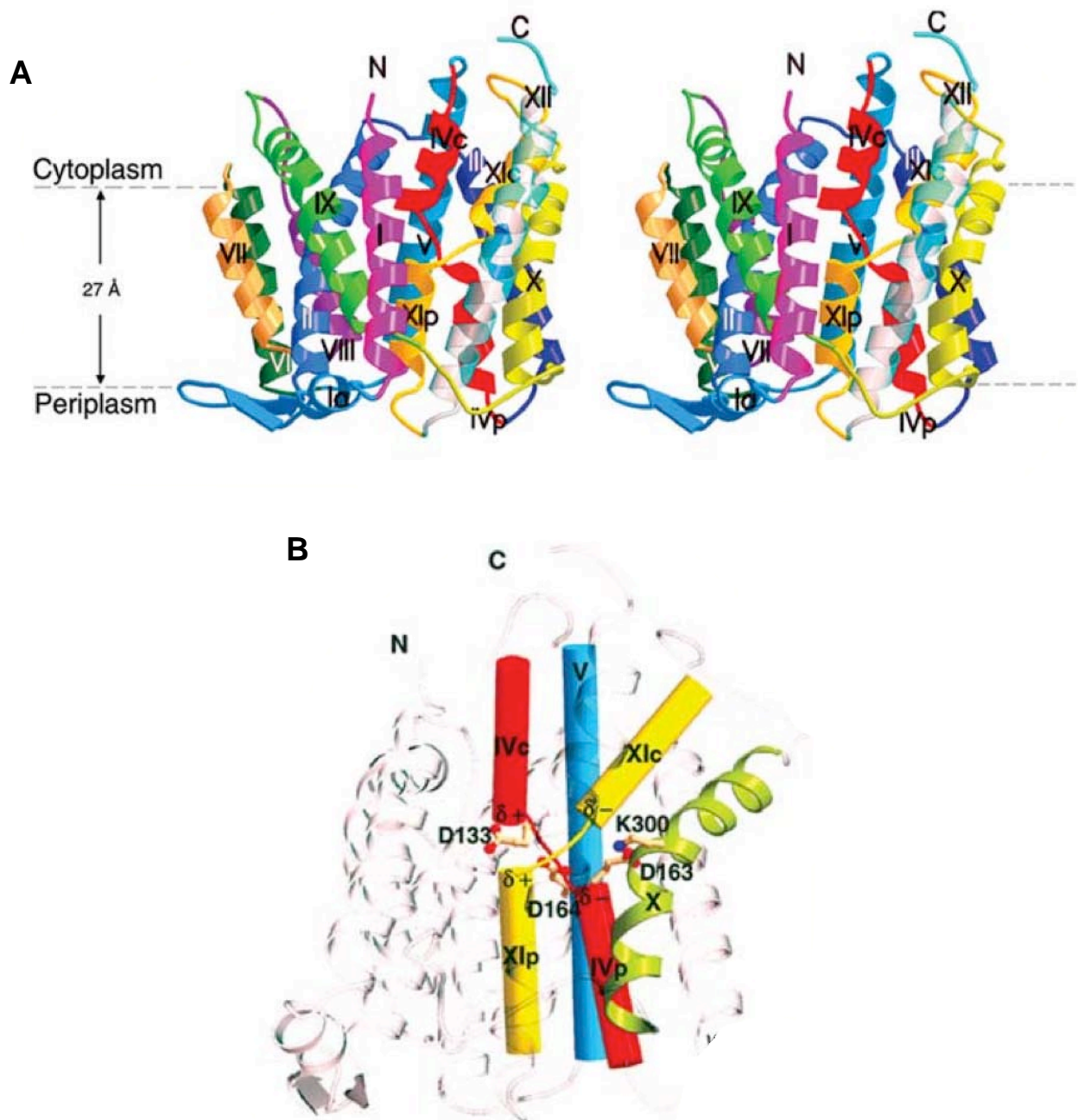
Figure 5, A. Stereo view of a ribbon representation viewed parallel to the membrane (grey broken lines). The 12 TMSs are labelled with roman numerals. B, TMSs IV/XI assembly. Helices of the assembly and helix V are shown as cylinders, helix X in ribbon representation. The partial charges of the N and C termini of the short helices are indicated. The orientation of the molecule is indicated with respect to A (Hunte et al., 2005a).

Biochemical mutagenesis and molecular dynamic simulation studies have put forward an intriguing mechanism of ion transport (Arkin et al., 2007). D163 and D164 in helix V were predicted to be the key residues in Na$^+$ binding as they are the only

carboxylic residues which are indispensable for transport activity. Strong clues from simulation studies suggested that Na^+ remains bound when placed near deprotonated D164 irrespective of the protonation state of D163. By contrast protonated D164 releases Na^+, its direction being determined by the protonation state of D163: if D163 is protonated, Na^+ is released in the periplasm and if it is deprotonated, Na^+ is released to the cytoplasm. This protonation and deprotonation of D163 brings about conformational changes in the protein, exposing the Na^+ binding site to periplasm and cytoplasm respectively. Simulations also suggested that D133 in TMS IV is the key residue acting as the pH sensor. D133 resides in the N termini of IV and XI neutralizing their opposing helical dipoles. Protonation of this residue brings about a conformational change resulting in a structure exactly like the down-regulated X-ray structure. In this conformation both in case of the X–ray structure and the simulated model, D164 faces the lumen away from the Na^+ entry or exit site further throwing light on the fact that both the structures are downregulated. In addition, mutation of this residue leads to complete inhibition of antiporter activity (Arkin et al., 2007).
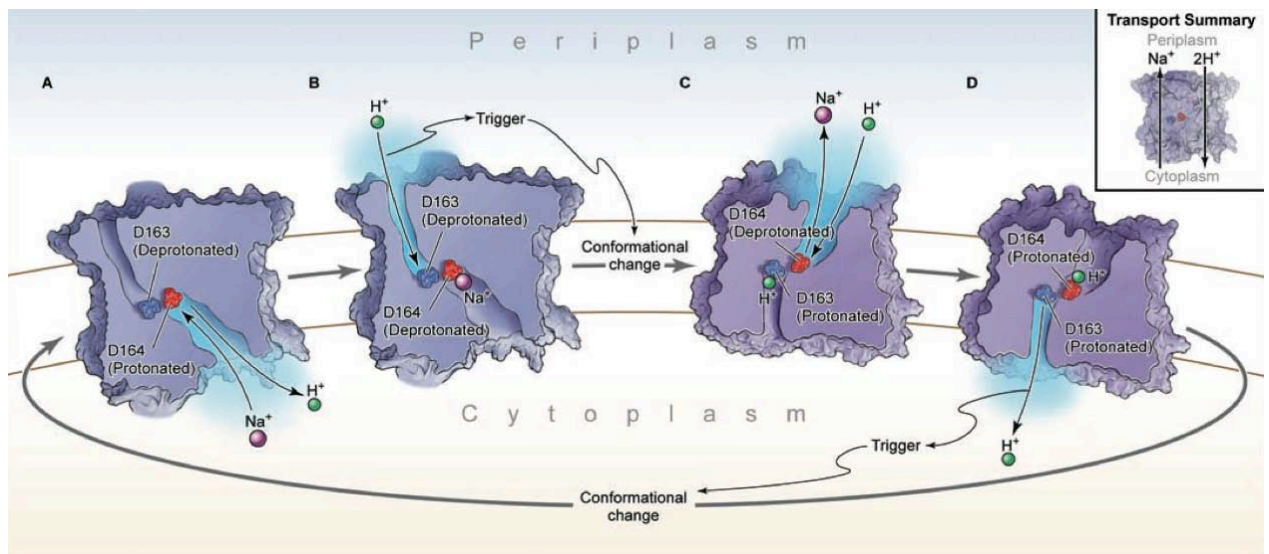
Figure 6 Schematic representation of the transport model of NhaA. The carboxylic group of D163 in the accessibility-control site is coloured in blue, and D164 in the Na^+-binding site is red (Arkin et al , Science, 2007).

1.5   Na⁺/H⁺ antiporter from *Methanococcus jannaschii*

1.5.1   Bioenergetics in Methanogens

Methanogens, belonging to the archaeal phylum Euryarchaeota produce methane as a metabolic by-product under anaerobic conditions. The pathway where a small number of compounds are converted to methane is linked to the generation of ion gradients across the membrane that is used to drive the synthesis of ATP. Two most common ion gradients simultaneously generated during methane formation are of H^+ and Na^+. In fact methanogens are the only microorganisms known to produce primary ion gradients of $\Delta\mu_{Na+}$ and $\Delta\mu H^+$ at the same time. Therefore, they are confronted with the problem of coupling both ion gradients to the synthesis of ATP (Deppenmeier, 1996).
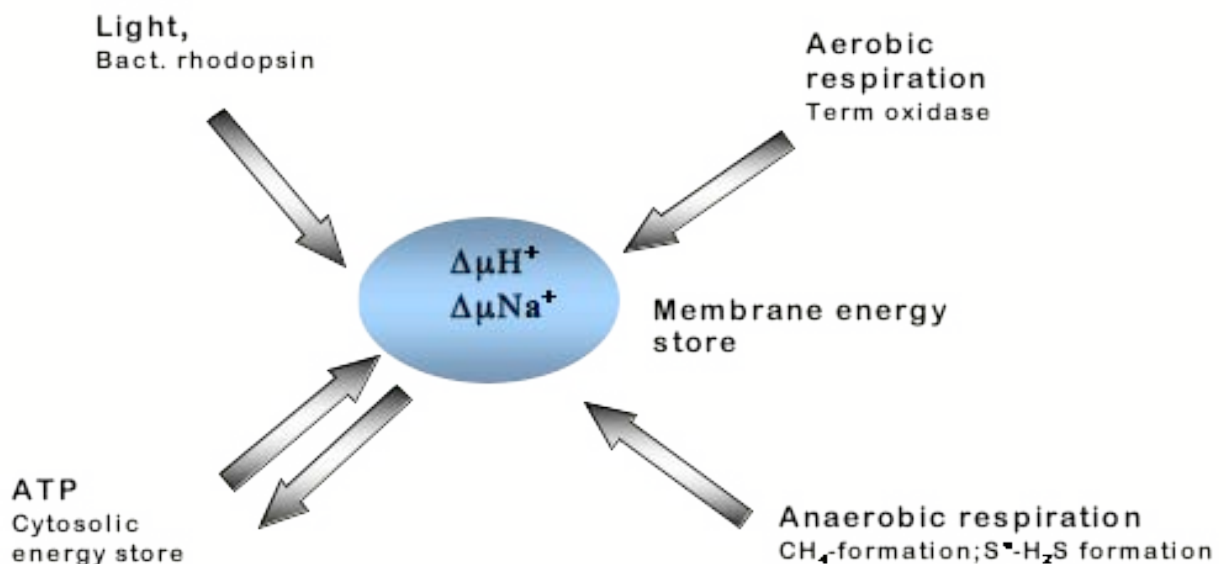
Figure 7   Primary energy-transducing processes and coupling principles in membrane bioenergetics. The scheme illustrates the processes found in archaea that contribute to the formation of either proton or sodium ion potentials across the plasma membrane [Figure adapted from (Schafer et al., 1999)]

The primary sodium ion pump in methanogens is the methyl-H4MPT:CoM methyltransferase (Becher et al., 1992; Fischer et al., 1992). This enzyme is part of the central pathway and therefore Na^+ transport is obligatory for methane formation. Because the central pathway is reversible, this enzyme functions as a generator of a

sodium ion potential during methanogenesis from CO_2 or acetate but as an enedergonic reaction. A theory suggests that the $\Delta\mu_{Na+}$ established by the methytransferase reaction is converted to a secondary proton gradient that then drives the synthesis of ATP via a H^+-translocating A_1A_0 ATPase (Kaesler and Schonheit, 1989).

1.5.2 MjNhaP1

The genome of the hyperthermophile *Methanococcus jannaschii (M. jannaschii)* has three Na^+/H^+ antiporter related genes, Mj1275, Mj1521 and Mj0057 (Hellmer et al., 2002). The corresponding proteins of Mj0057 and Mj1521 belong to the NhaP family and hence they were named as MjNhaP1 and MjNhaP2 respectively, while that of Mj1275 is called MjNapA as it is related to the NapA family.

1.5.2.1 Sequence conservation

MjNhaP1 and MjNhap2 share 45% identity and therefore can be said to have arisen from gene duplication. The sequence identity of these two proteins to putative antiporters of the NhaP type coming from archaeons like *Methanopyrus kandleri* (42%-46%) and *Pyrococcus abyssi* (27%-31%) is high. In addition, MjNhaP1 and MjNhaP2 are closer to eukaryotic antiporters like SOS1 from *Arabidopsis thaliana* (18%-21%) and Human NHE1 (18%-21%) than to the *E.coli* NhaA and NhaB (10%-12%) in terms of sequence similarity (Hellmer et al., 2002). There are three motifs in the sequence of the NhaP family of antiporters. The TDP and the FNDP motif are widespread amongst eukaryotic and prokaryotic antiporters, but the conserved motif GPRGVVP is unique to the NhaP family (Hellmer et al., 2002).

1.5.2.2 Physiological role of MjNhaP1

Measurement of H^+ transport by fluorescence in everted vesicles shows that MjNhaP1 is the most active amongst the three (Hellmer et al., 2002). In contrast to *E.coli* NhaA, which has a functional pH range between pH 7.0 and 8.5 (Padan, 2004; Taglicht, 1991), MjNhaP1 is active at pH 7.0 and below, and switches off above pH 7.0. Interestingly, the human homologue, NHE1, also has the highest activity between pH 6-6.5 (Padan et al., 2001). Like the *E.coli* NhaA, MjNhaP1 has a low K_m for lithium ions (2.5mM) compared to Na^+ ions (10mM) (Hellmer et al, 2002). MjNhaP1 did not functionally complement NhaA in mutant *E.coli* strains. This could

be because the antiporter becomes inactive in the cytoplasmic pH of *E.coli* (Hellmer, 2002). The natural marine habitat of *M. jannaschii* has a salt concentration of 10-15mg/ml and a pH of 4.0-6.0. Based on the activity profiles of MjNhaP1 which is responsible for pH homeostasis in the cell, the internal pH of *M. jannaschii* is likely to be around 6.5 (Vinothkumar et al., 2005).

```
NhaP_Thermoplasma/1-432        1 -----------MTAIFPFGYYLDVSLILVLGAIALPISRKMSVVEIPILVFLGIIIGPMLHLIS 53
NhaP_Pyrococcus/1-443          1 ------------MIELSLAEALFLILFTGVISMLISRRTGISYVPIFILTGLVIGPLLKLIP 50
NhaP-M.Kandleri/1-434          1 MWRTVKMGGSTTKFGFFTLVGYTALLLSLGAIVARLSEDRGLPDIPFLLLLGFLLGPIAGIVR 63
Q60362_M.jannaschii_NhaP1/1-42 1 -------------MELMMAIGYLGLALVLGSLVAKIAEKLKIPDIPLLLLLGLIIGPFLQIIP 50
NP_414560_E.coliNhaA/1-388     1 MKHLHRFFSS-----------------------------DASGGIILIIAAILAMIMANSGA 33

NhaP_Thermoplasma/1-432         54 PNFSVYLFSSFAGVGIGMMGLVIILYSESHNMNLKVLRSEFYRIASLDTLGVIITAVVAGLVF 116
NhaP_Pyrococcus/1-443           51 RDLAHEIFDFVR-----VFGLVIILFTEGHNLSWRLLKKNMPTIVTLDTIGLILTALIAGFIF 108
NhaP-M.Kandleri/1-434           64 PEYAQKA-FPFVG----TLGLIIILLDGGFEIGIDVLRRVASLVAKLDSITLLITAGISSLIF 121
Q60362_M.jannaschii_NhaP1/1-42  51 SDSAMEI-FEYAG----PIGLIFILLGGAFTMRISLLKRVIKTVVRLDTITFLITLLISGFIF 108
NP_414560_E.coliNhaA/1-388      34 TSGWYDFLVGIMLLWINDALMAVFFLLVGLEVKRELMQGSLASLRQAAFPVIAAIGGMIVPAL 96

NhaP_Thermoplasma/1-432        117 TVLTGAP--IIVGFLFGAIVSPTDPVTLIPLFRRVKVSEDISEILVGES--LFNDPVGIILVS 175
NhaP_Pyrococcus/1-443          109 KVVFNSS--FLLGFLFGAIIGATDPATLIPLFRQYRVKQDIETVIVTES--IFNDPLGIVLTL 167
NhaP-M.Kandleri/1-434          122 NLVFGLKPFSPIGFLYGSITCATDPATLIPVFSKVELPINISTALIAES--VFNDPLGVVLTK 182
Q60362_M.jannaschii_NhaP1/1-42 109 NMVLNLPYTSPVGYLFGAITAATDPATLIPVFSRVRTNPEVAITLEAES--VFNDPLGVVLTK 169
NP_414560_E.coliNhaA/1-388      97 LYLAFNYAD-PITREGWAIPAATDIAFALGVLALLGSRVPLALKIFLMALAIIDDLGAIIIIA 158

NhaP_Thermoplasma/1-432        176 VGIALLAPQSSYVSLFSAMNRVITFYPSIVAYFLIQVAVPSIVGIAIGFSVIYLDKKIKFENY 238
NhaP_Pyrococcus/1-443          168 IAISMLVPG-YGGGIFSTLSEKLGIYAGGVIYFLYNVSVSISLGIFLGILGYKFIKRTGIFDF 229
NhaP-M.Kandleri/1-434          183 MSLSVMGLSSHQ--NPILLFISLAAGGAALGLATGVVLERLLAREPFGEY--VVPITLGAALA 241
Q60362_M.jannaschii_NhaP1/1-42 170 MSLSVMGLGLFSSSNPLIDLITLAGGAIVVGLLLAKIYEKIIIHCDFHEY--VAPLVLGGAML 230
NP_414560_E.coliNhaA/1-388     159 LFYTNDLSM--ASLGVAAVAIAVLAVLNLCGARR-------------TGVYILVGVVLWTAVLK 207

NhaP_Thermoplasma/1-432        239 LTAMLLGLVIFEFT--VFESLSITPFPAIIATGAIVGNFSDKNIFWSREQNFQESLSFLSAAI 299
NhaP_Pyrococcus/1-443          230 PEIEAFSLSLAFLGFFIGERLDASGYLVATVTGIVLGNYKLLKPRENIRILKRLQRAIEKEVH 292
NhaP-M.Kandleri/1-434          242 LWYICEELLPGLLGYELSGFMAVAVLGMYLGNNLIKHDY--------LKDDRTFLKDFFEELS 296
Q60362_M.jannaschii_NhaP1/1-42 231 LLYVGDDLLPSICGYGFSGYMAVAIMGLYLGDALFRADD----------IDYKYIVSFCDDLS 283
NP_414560_E.coliNhaA/1-388     208 SGVHATLA-GVIVGFFIPLKEKHGRS--------------------------------- 232

NhaP_Thermoplasma/1-432        300 IFILIGSSFTLSEIVSYILLGIALT-------------------ILIVFLVRPLAVFPSLM 341
NhaP_Pyrococcus/1-443          293 FNDTLAALATIFIFVLLGAEMNLEVIWSNLGKG---------LLVALGVMILARPLATLPLLK 346
NhaP-M.Kandleri/1-434          297 TVVRIMVFTLLGACVSISLLKTFWLKG-------------LVCALSNVFIARPAGVIIGTY 344
Q60362_M.jannaschii_NhaP1/1-42 284 LLARVFIFVFLGACIKLSMLENYFIPG--------------LLVALGSIFLARPLGVFLGLI 331
NP_414560_E.coliNhaA/1-388     233 PAKRLEHVLHPWVAYLILPLFAFANAGVSLQGVTLDGLTSILPLGIIAGLLIGKPLGISLFCW 295

NhaP_Thermoplasma/1-432        342 IADARKPKMKSYY--KIAAFISLVGPRGVVPVVLSTLPYVVGEEYNIPVL-VTWG-------- 393
NhaP_Pyrococcus/1-443          347 WWNFR-EY----------LFIALEGPRGVVPSALASLPLSLALKYKSPLLTVHWGE------- 391
NhaP-M.Kandleri/1-434          345 IPPKEDL------NLKERIYLALEGPRGVVPAALVGTIYSKIVSNPHAVPVAIASEMPPKTLA 401
Q60362_M.jannaschii_NhaP1/1-42 332 GSKHSFKE-------K--LYFALEGPRGVVPAALAVTVGIEILKNADKIPAS------TKYIT 379
NP_414560_E.coliNhaA/1-388     296 LALRLKLAHLPEGTTYQQIMVV------------GILCGIGFTMSIFIASLAF------GSVD 340

NhaP_Thermoplasma/1-432        394 PLISVSALFVVLFSIVLQTLYTPIIRNIFLP---------DSGNGSEK-------- 432
NhaP_Pyrococcus/1-443          392 -IIMATVVITVLTSVIVETLWIPILKDKLDVGETIKERIEEKEEEKERRKVRG--- 443
NhaP-M.Kandleri/1-434          402 SAILVTTFLTIFISVVLEATWAQPLAKRLL----------------KEE------- 434
Q60362_M.jannaschii_NhaP1/1-42 380 PTDIAGTIIIGTFMTILLSVILEASWAGMLALKLLG--------EYKPKYKEESHH 427
NP_414560_E.coliNhaA/1-388     341 PE-LINWAKLGILVGSISSAVIGYSWLRVRLRPSV-------------------- 374
```

Figure 8 Alignment of four Na⁺/H⁺ antiporters of the NhaP type with *E.coli* NhaA. Alignment was carried out with ClustaWl and viewed with the software Jalview. Identical conserved amino acids are highlighted in light and dark blue. The antiporters in the alignment from top to bottom are 1. NhaP from *Thermoplasma acidophilum* 2. NhaP *from Pyrococcus abyssi* 3. NhaP from *Methanococcus kandleri* 4. MjNhaP1 from from *Methanococcus jannaschii* . 5. NhaA from *E. coli*

During a drop or rise in the internal pH the antiporter pumps protons out or allows protons in, respectively. In the former case, the Na⁺ gradient is used and in the latter case the increasing pH gradient is used to extrude Na⁺. Under extreme pH differences, the antiporter must be switched off to prevent an uncontrolled influx of Na⁺ or complete loss of Na⁺ from the cell, which is undesirable as several of the unique enzymes of *M. jannaschii* are Na⁺-dependent. These considerations might

partly explain why MjNhaP1 shuts down at a pH below 6, and above pH 7 (Vinothkumar et al., 2005).

1.5.2.3 Functionally important amino acids

Four acidic residues in MjNhap1, D93, D132, D162, and E156, are highly conserved. Amongst these, D132 and D162 have the highest conservation from bacteria to human while homologs of D93 are found only in the NhaP family. E156 has a homolog in NHE1, which is absent in NhaA reflecting the similarity of MjNhaP1 to eukaryotic antiporters. Besides these acidic residues, two basic residues R320 and R347 in MjNhaP1 have homologs in isoforms of the human Na^+/H^+ exchanger. K300 of *E.coli*, which is necessary for function, is homologous to the R320 residue. Unlike in the *E.coli* NhaA, the His residues in MjNhaP1 shows no conservation.

Site directed mutagenesis and functional analysis of the MjNhaP1 mutants have identified essential residues for antiporter activity. None of the His mutants of MjNhaP1 affected the antiporter activity. Mutants D131, D161 did not show antiporter activity at any pH whereas mutations of the less conserved D93 only lowered the activity. R320A (but not R320H) lead to a complete loss of antiporter activity (Hellmer et al., 2003).

1.5.2.4 Structural features of MjNhaP1

Hydropathy analysis of MjNhaP1 predicts 13 transmembrane helices. This is unusual for a secondary transporter but not unique (Jung, 1998). A 8Å projection map of MjNhaP1 at pH 4.0 (Vinothkumar et al., 2005) shows that MjNhaP1 is arranged in a dimer consisting of two regions: a dimer interface consisting of density peaks which suggests highly tilted membrane spanning helices and a outer bundle where the density peaks indicate a perpendicularly oriented group of helices (Figure 9A). This projection map revealed that MjNhaP1 is remarkably different from its *E.coli* counterpart NhaA. The overall dimensions in the two projection maps differed with 38 Å X 96 Å for a NhaA dimer and 51 Å X 94 Å for a MjNhaP1 dimer. The dimer core in both proteins appears different, indicating a different orientation of the helices. Although the outer bundle in both proteins looked similar, the helices in MjNhaP1 suggest a more perpendicular orientation to the membrane plane.

1.5.2.5 pH induced conformation change:

Generally, secondary transporters undergo a change in conformation during the transport process. In case of Na^+/H^+ antiporters such conformational changes are thought to be pH-induced. Using cryo-electron microscopy, a pH-induced conformational change has been mapped for MjNhaP1 (Vinothkumar et al., 2005). Significant differences in the projection structures at pH 4 and 8 appeared as a change in the distribution of densities within the helix bundle. At high pH, the disappearance of a peak between two of the helix densities (asterisk in Figure 8) resulted in a change in the bundle shape, hinting to a tilt or rotation of individual helices. There were no visible changes apparent in the dimer interface. A difference map of projection data at pH 4.0 and pH 8.0 confirmed that the pH-induced structural changes are localized at the membrane-spanning helix bundles at either side of the dimer core.
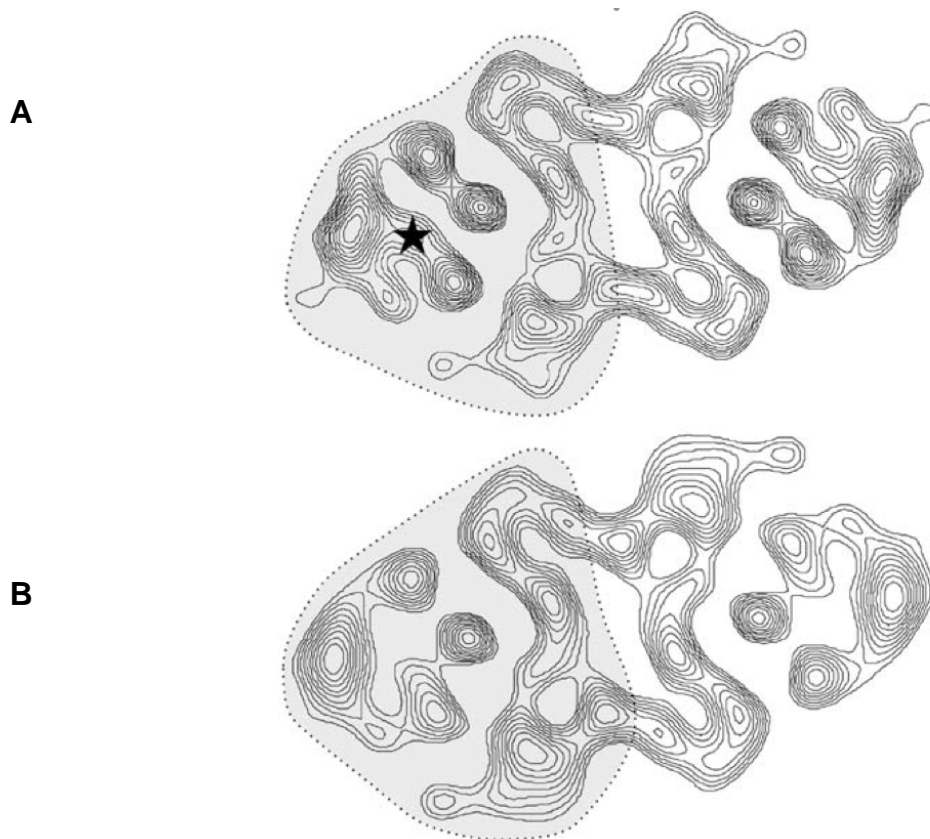
Figure 9 (A) Dimer of MjNhaP1 at pH 4. (B) Dimer of MjNhaP1 at pH 8. The map resolution is 8 Å, with only positive contours shown. The putative monomer is outlined. The asterisk marks a density in MjNhaP1 that is not present at pH 8. (Vinothkumar et al, 2005)

Aside from its physiological role, the human NHE1 has been implicated in several diseases, primarily heart diseases and cancer. During ischaemia, increased anaerobic glycolysis leads to a large increase in the production of protons. NHE1 becomes activated and exchanges intracellular protons for extracellular sodium, leading to a rapid accumulation of sodium in the cell. Na^+/K^+ ATPase, which pumps out accumulated Na^+ under normal conditions is inhibited by the decrease in high-energy phosphate stores that occurs during ischaemia. A reversal of the Na^+/Ca^{2+} exchanger occurs, causing accumulation of a high amount of Ca^{2+} within the cell. The build-up of calcium triggers various pathways, leading to cell death (Slepkov et al., 2007). Using drugs to inhibit NHE1 during open-heart surgery is required to prevent such consequences. A study (Mentzer et al., 2003) showed that the inhibitor cariporide administration caused a modest, but significant, reduction in myocardial infarction after coronary artery bypass graft surgery.

'Malignant acidosis' is considered to represent a key step in oncogenic transformation. This is caused by NHE1, which reverses the pH gradient in many types of transformed and/or malignant cells so that the intracellular environment is alkaline and the extracellular environment is acidic. A study (Bourguignon et al., 2004) has shown that NHE1 is activated in the breast tumour microenvironment through CD44, a multifunctional transmembrane glycoprotein expressed in many cells and tissues including breast tumor cells and carcinoma tissues (Dall et al., 1995). This increases the acidification of the extracellular environment, promoting breast cancer progression. NHE1 inhibitors have been shown to induce apoptosis in various cancer cell lines and have a high potential in treating various types of cancer (Rich et al., 2000). The efficacy of NHE1 inhibitors for treating cancer requires preclinical and clinical trials. In order to design drugs specific for NHE1, three-dimensional stuctural information is crucial. So far due to several technical difficulties, no concrete structural information is available for any of eukaryotic Na^+/H^+ exchanger. As stated earlier MjNhaP1 shares 18%-21% sequence homology to NHE1 and also performs antiporter activity in similar pH range. Three-dimensional structural information from this archaeal homolog of NHE1 will broaden our understanding of the structure and function of Na^+/H^+exchangers and help in designing better drugs and inhibitors.

1.7 Membrane Protein structure determination

Membrane proteins constitute between 20% and 30% of the proteomes in all organisms (Krogh et al., 2001). They are involved in many cellular functions and their deregulation results in several diseased states. Many pharmaceuticals target membrane proteins (40%) (Overington et al., 2006), which makes it imperative to know their structures. Regardless of their importance fewer than 1% of the membrane proteins are of known structures (Loll, 2003). Membrane proteins are difficult to study due to their relatively hydrophobic surface and they need to be extracted from the cell membrane with detergents. Due to their flexible and unstable nature, obstacles arise at all levels, including expression, solubilisation, purification, crystallisation, data collection and structure solution (Carpenter et al., 2008).

Three different techniques have gained ground in determining membrane protein structure: (a) NMR spectroscopy (b) X-ray Crystallography (c) Electron microscopy.

Nuclear magnetic resonance (NMR) spectroscopy is a suitable technique to study membrane proteins since it can study molecules in liquid crystalline bilayers and micelles formed by the lipids that associate with membrane proteins (Franzin et al., 2007). Structure determination is possible in a native-like environment by solution NMR methods that uses samples of proteins in lipid micelles, while solid-state NMR methods can be applied to samples of membrane proteins in lipid bilayers. The two approaches can be combined in a complementary manner for detailed description of structure and dynamics of membrane proteins. In addition, with NMR, it is possible to get intimate dynamic information and electronic details of bound ligands and details of the binding site can be resolved. Nevertheless, structural studies of membrane protein by NMR suffer from slow molecular motion of the protein-membrane particles (bilayers, bicelles, or micelles), which hampers the use of standard liquid-state NMR methods. Due to the need to resolve resonances within the available spectral regions and also because of the fact that fast molecular re-orientation is required to average out effects from anisotropic nuclear spin interactions, there is generally a restriction to proteins up to 30-50 KDa. Large proteins have slow molecular motion inducing line broadening, which degrades resolution (Nielsen et al., 2004). However, significant methodological advances (Clore and Gronenborn, 1997) and application of principles of TROSY (transverse relaxation-optimised spectroscopy) (Pervushin et al., 1997) has increased the upper limit of overall size of lipid-protein supramolecular structure.

Structures of a variety of helical membrane proteins [Gramicidin A (Ketchem et al., 1993), ChaB (Osborne et al., 2004) and Mistic (Roosild et al., 2005)] and *E.coli* β-barrel porins [OmpA (Arora et al., 2001) , PagP (Hwang et al., 2002) , OmpX (Fernandez et al., 2004) have been determined by NMR in micelles and in bilayers.

X-ray crystallography was the first technique to determine a membrane protein structure (Deisenhofer et al., 1984) and since then there has been a slow but steady growth in the number of structures determined by this method. It is the most preferred technique primarily because of the high resolution it offers. The pre-requisite for solving a membrane protein structure is highly ordered 3D crystals. Once a crystal condition is obtained after screening various parameters, optimization is necessary to achieve high resolution. The first hindrance comes from limited yield of membrane proteins. The success rate with crystal structures obtained from naturally abundant protein is significantly higher compared to of recombinant proteins. Over-expression of membrane protein is problematic as high-level expression can saturate the secretory pathway, leading either to the build-up of toxic intermediates or to inclusion body formation (Loll, 2003). High-resolution atomic structure for prokaryotic membrane protein are significantly ahead in comparison to eukaryotic membrane proteins. The challenges are in finding a suitable host system that provides a compatible lipid environment and post-translational modification apparatus.

The next critical consideration in obtaining well diffracting crystals is to choose the correct detergent amongst the dozens different detergents commonly used in biochemistry, dozens more that are less well characterized, and many novel detergents under development (McQuade et al., 2000). The detergent selected should maintain conformational homogeneity and avoid aggregation states. The presence of detergent complicates the optimization of well-ordered 3-D crystals. Due to the complex phase behaviour of detergents, the solution in crystal drop can separate into two liquid phases, one detergent-rich and the other detergent-poor with integral membrane proteins partitioning into the detergent-rich phase (Ward, 1987). This can lead to denaturation and prove deleterious to crystal growth. One method which minimizes the effect of detergents is by obtaining 3D crystals in lipid-cubic phase and there are a few examples where structure determination has been successful (Cherezov et al., 2007; Pebay-Peyroula, 1997). Antibody mediated crystallization is a valuable tool for membrane proteins with small hydrophilic loops

as the binding of Fv or Fab fragments enlarges the small hydrophilic part, thereby providing additional surface for crystal contacts and space for the detergent micelle (Hunte and Michel, 2002). Successful cases where the diffraction was enhanced by co-crystallization with antibodies are cytochrome c oxidase (Ostermeier et al., 1995), cytochrome bc1 complex (Hunte et al., 2000), Potassium channel (Zhou et al., 2001).

In the current work, the prime method used for structural studies is cryo-electron crystallography. In the following section, this technique is discussed in brief.

1.7.1 Cryo-electron electron crystallography

The term electron crystallography can be defined in structural molecular biology as a method where electron diffraction data and electron microscope images are used to determine the structure of biological macromolecules (Glaeser R M, 2007). In this work electron crystallography was used on 2D crystals of MjNhaP1 to determine its three-dimensional architecture. Because 2D crystals can be formed naturally and artificially in lipid bilayers, membrane proteins can be studied in an environment close to their native one, rather than in a detergent micelle in which denaturation and loss of activity might occur. This represents a huge incentive for membrane protein researchers to apply this technique for structure determination (Ford and Holzenburg, 2008). Although atomic resolution is a challenge, electron crystallography has given medium resolution information of transporters, ion-channels, membrane bound enzymes and receptors. Such medium resolution allows localization of secondary structural features, especially transmembrane helices. It is also a novel approach to study conformational changes that are associated with protein function (Subramaniam et al., 1993; Vinothkumar et al., 2005; Vonck, 2000). A feature of electron waves is that they can be focussed by magnetic or electric lenses. Hence, crystallographic phase information is fully retained in images and is a great advantage over X-ray crystallography.

Integral membrane proteins like bacteriorhodopsin represent natural 2D crystals. An atomic resolution structure had been determined for this protein by electron crystallography of highly ordered 2D crystals obtained by fusing purified fragments of purple membrane (Baldwin J, 1988). There are examples when integral membrane proteins have been induced to form 2D arrays during membrane isolation. Nicotinic acetyl choline receptor from electroplax of electric fish form 2D arrays upon storage of isolated membrane vesicles (Brisson A, 1985). One of the most widely used

techniques to obtain 2D crystals is reconstitution of purified protein in lipid bilayers. The membrane proteins in such cases are isolated by detergents and purified by column chromatography or other purification method. The detergent is removed by dialysis, dilution, or biobeads in the presence of small quantities of lipids. Some membrane proteins form 2D crystals in detergent-solubilized state. This apparently takes place by detergent micelle fusion. Thin, sheet-like crystals of the light harvesting complex have been amongst the most successful examples (Kühlbrandt, 1994).

Visualizing and image recording of the 2D crystals involve preparing the specimen suitably. Initial screening of the sample involves embedding the specimen within a matrix of a heavy-metal compound such as uranyl acetate or ammonium molybdate. The bulk water in which the specimen is embedded, is replaced by a solid matrix of amorphous salt. This method of negative staining provides an easy way to characterize morphology and specimen quality.

Sample can be preserved in the native hydrated by glucose embedding and imaging at low temperature using a cold stage (Y. Fujiyoshi, 1991). The glucose penetrates the crevices and channels of the structure of the specimen and prevents flattening and collapse which is a drying effect. In this way, the native crystalline order of the specimen is preserved in the vacuum of the electron microscope for longer duration (Glaeser R M, 2007) . One of the major challenges in working with 2D crystals lies in preparing extremely flat specimens. This becomes a major hurdle for specimen tilts, which is necessary for a 3D reconstruction. Wrinkling, buckling or imperfect flatness has a stronger effect at high resolution and high tilt angle. It causes broadening of diffraction spots for Bragg reflections in the direction perpendicular to the tilt axis and results in anisotropic data.

Selected images are digitized for further processing. The digitized image is Fourier transformed for extracting the phases and amplitudes. The signal to noise ratio in cryo-electron microscopy is very low. It can be dramatically improved by a filtering procedure called masking. The Fourier transform is masked so that all values except for those near diffraction spots are set to zero. The inverse transform thus removes all noise leaving a clearer image of the crystal. Procedures to compensate for real space distortion are common in 2D crystals image processing. This step called unbending involves re-interpolation of the image array such that the unit cell positions are shifted back onto their respective position on an ideal lattice. Finally, to obtain a

3D data set, the structure factors from different images must be combined. The merging of 3D data set involves the determination of phase origin of the untilted images and tilt geometry of the tilted images. Systematic image defects like the effect of contrast transfer function on image contrast and amplitudes at high resolution can be computationally corrected.

The biggest drawback of electron crystallography on rather electron microscopy as a whole is the missing cone problem. To arrive at a 3D structure, different projections of 2D crystals are generated by tilting the crystals relative to the incident electron beam. In practice, however, virtually no data can be obtained with the specimen tilted beyond 70° because the bars of the support grid occlude the specimen beyond this angle. There are therefore information deficits along one direction in space (the z-axis, normal to the crystal x,y plane), which leads to a loss of resolution in the vertical direction. Despite the challenges and limitations, electron crystallography has established itself as a viable alternative to X-ray crystallography structure determination, especially for membrane proteins.

1.8   Aim of the thesis

The *E.coli* NhaA is biochemically well-characterized and the structure of the acid down-regulated form has been resolved (Hunte et al., 2005a). NhaA is the only member of the ubiquitous Na^+/H^+ exchanger family, which has 3D structural information available. Three-dimensional structures of homologous proteins from other domains of the biological kingdom in different conformations would certainly enhance our understanding of the working mechanism of such membrane transporters. Therefore, the final aim of this thesis is the three-dimensional structure determination of the Na^+/H^+ antiporter, MjNhaP1, from the hyperthermophile *Methanococcus jannaschii* which shares high sequence homology to the human NHE1 and carry out Na^+/H^+ exchange at similar pH range. This aim was addressed by (a) Targeting high quantity of monodisperse protein (b) Screening of conditions for well-ordered 3D crystals which would diffract X-ray to a high order (c) Optimizing existing 2D crystals (Vinothkumar et al, 2005) and recording images of these 2D crystals in the electron microscope to reconstruct a 3D volume.

2   Materials and Methods

2.1   Basic molecular biology techniques

2.1.1   Preparation of competent *E.coli* cells

(Method adopted from Molecular cloning, Volume 1, Sambrook and Russell)

Bacterial strains:

Name of the strain	Supplier
E.coli BL21 pLysS	Stratagene, US-La Jolla
E.coli BL21 (DE3)	Invitrogen, D-Karlsruhe
E.coli BL21 (DE3) C43	Avidis, France
E.coli BL21 (DE3) C41	Avidis, France
E.coli DH5α	Invitrogen, D-Karlsruhe
E.coli TOP10	Invitrogen, D-Karlsruhe

Fresh Luria Bertini (LB) plates were streaked with glycerol stocks of the desired bacterial strain. Single colonies were inoculated into 5ml of liquid LB and were allowed to grow at 37°C for 16-17 hrs. 100µl of this preculture was subcultured to 50ml Super Optimal Broth or Tryptone/yeast extract bacterial (SOB/SOC) media and grown at 37°C till an OD_{600} = 0.4-0.5 of mid exponential phase was reached. Cells were harvested in an ice-cold tube at around 2700g for 10min at 4°C. Two rounds of washing were carried out: 1st with 20ml of ice cold 80mM $MgCl_2$, 20mM $CaCl_2$ and 2nd with 20ml of 0.1M $CaCl_2$. After the second wash, the pellet was resuspended in 4ml of 0.1M$CaCl_2$. 140ml of DMSO (dimethyl sulfoxide) was added to this resuspension. Aliquots of cells (200µl) were made and plunge frozen in liquid nitrogen before storing them at –80°C.

2.1.2   DNA transformation

1µl of 0.1ng/µl DNA was mixed with 100µl of competent cells and incubated on ice for 30min. The cells were then treated with a heat shock for 90 seconds in a water bath at 42°C. The transformed cells were incubated on the shaker at 37°C for 45

minutes after adding 0.8ml of Luria Broth. The regenerated cells were plated out on LB plates with antibiotic selection.

2.1.3 Electrocompetent E.coli cells for electroporation

Bacterial strain: _E. coli_ cells (Top10F') purchased from Invitrogen.

45µl of frozen cells were thawed on ice. The required amount of DNA was mixed with the cells followed by a short incubation on ice for 5min. The cells were then transferred to an electroporation cuvette (GenePulser® cuvette, BioRad Inc) and electroporated at 2000V, 300Ω and 25µF. After reaching a pulse of 4.9 msec SOC was added immediately to the cell suspensions. This suspension was allowed to revive at 37∞C for 1hr before plating on an antibiotic containing LB agar plate.

2.1.4 Preparation of glycerol stocks for culture maintainance

5ml LB media with selection marker was inoculated with a single colony from a fresh transformation plate. The cell culture was diluted to a final concentration of 20% with autoclaved glycerol. Aliquots of 200ml were made and stored at -80°C.

2.2 Cloning of NhaP1

2.2.1 Polymerase chain reaction

The NhaP1 encoding gene, Mj0057, has been previously cloned into the expression vector pET26b (Vinothkumar et al), which has a C-terminal hexa histidine tag. For designing new expression plasmids, NhaP1 was amplified using the above mentioned pET26b-NhaP (**NhaP1$_{His}$**) as a template with the following forward (For1) and two reverse (Rev1& Rev2) primers (MWG-Biotech-AG);

For 1: 5' TACG*CCGCGGACATATG*GAACTTATGATG3'

Rev 1: 5'TG*GAATTCTCGAG*TTAATGGTGGGATTCTTCTTT3'

Rev2: 5'TGGAATTCTCGAGTTAGTGATGGTGATGATGGTGGGATTCTTCTTT3'

42

The primers introduced a *Sac*II (green) or *Nde*1 (blue) restriction enzyme site at the N-terminus and *Xho*I (orange) and *Eco*RI (cyan) restriction enzyme site at the C-terminus of the amplified product. 4 histidines were introduced when amplified with Rev2. Primers were resuspended in double distilled H2O to form a 10µM stock solution. 1µM of each primer was added to 1U Pfu DNA polymerase (Stratagene, Heidelberg), 0.2mM dNTPs, 1mM $MgSO_4$, 1ng plasmid template, 5µl of 10X PCR buffer for Pfu DNA polymerase (Stratagene, Heidelberg). The total reaction volume was 50µl.

Template amplification was performed in a thermal cycler T3 thermocycler, Biometra, Göttingen) with the following programme:

5 min 95 C Hotstart Denaturation

30 cycle

45s   95°C Denaturation

30s   45°C Primer hybridization

 45s   72°C Polymerization

 10min 72°C End Polymerization

Till cool down to 4°C

Reaction mixtures were analysed for PCR products of correct length by loading 1µl onto a 1.2% agarose gel (80V, 30mins, B1A, Owi seperation system USA Portmoth-NH). DNA was stained with ethidium bromide (~0.01%v/v) and visualised under UV illumination. Proteins, dNTPs and unused primers, were removed from successful PCR reaction mixtures using the commercially available, QIAquick® PCR purification kit (Qiagen).

2.2.2   Expression plasmids

Following expression plasmids were generated for the NhaP1 gene:

1. *pSKB2LNB-NhaP1 (Novagen, modified).* The expression cassette is under the transcriptional control of the T7 promoter. This plasmid has a N-terminal hexa histidine tag, which can be cleaved off using the PreScisson protease (Amersham pharmacia Biotech). The NhaP1 gene from a previous clone (Vinothkumar et al.,

2005) was released by restriction digestion with *Nde*1 and *Xho*1(New England Biolabs) and subcloned into pSKB2LNB . The new expression plasmid with NhaP1 inserted into this vector will be further referred as _{His}NhaP1.

 2. *pASKIBA13plus-NhaP1* (IBA, Biotagnology, Göttingen) The expression cassette is under the transcriptional control of a tetracycline promoter. This plasmid has a N-terminal Strep-Tactin affinity tag (Strep tag II), which can be removed by cleavage with thrombin (Sigma-aldrich). The NhaP1 gene was amplified from a (Vinothkumar et al., 2005) previous construct with primer For 1 and Rev 1. The amplified PCR product was digested with *Sac*II and *Xho*1 and cloned into the vector pASKIBA13plus. The new expression plasmid with NhaP1 inserted into this vector will be further referred as _{Strep}NhaP1.

2.2.3   Plasmid extraction

Colonies of transformed cells (DH5α) with the above plasmids were inoculated into 5ml LB with 50µg/ml Kanamycin (1) or 100µg/ml Ampicillin (2). The inoculated media was incubated for 16 hours at 37°C in a shaker at 180 rpm. Plasmids were purified using the commercially available QIAprep® Miniprep kit.

2.2.4   Estimation of plasmid concentration

The plasmid concentration can be determined spectrophotometrically. The plasmid was diluted by 1:100 and the absorbance (optical density) measured at 260nm. One absorbance unit at 260nm is equivalent to 50µg/ml of double stranded DNA for a pathlength of 1cm; this is the molar extinction coefficient of DNA. An average of three readings was taken. The formula given below was used to calculate the final concentration:

Absorbance $OD\lambda_{260}$ x 50 x dilution factor = DNA sample concentration (µg/ml)

2.2.5   Agarose Gel Electrophoresis

0.8g of low-melt agarose (Sigma) was dissolved in 100ml of 1x TAE buffer (40mM tris-acetate pH8.0, 1mM EDTA) and heated in a microwave. The solution was allowed to cool down before pouring it out into a cast. Just before pouring, 1µl of

ethidium bromide solution was added. After the gel solidified, it was transferred into a Biorad sub-cell GT system and submerged with 1x TAE buffer. The sample was mixed with DNA loading buffer and electrophoresis was performed at 80V for 30 minutes. The stained bands were visualised with a UV illuminator (Biorad).

2.2.6 Restriction Enzyme Digestion

Before ligation, the PCR products and the plasmids require to be digested with the respective restriction enzymes to generate 'sticky ends' necessary for ligation.

Restriction digestion mix (Total volume 50µl with ddH$_2$0)

	Plasmid	PCR product
DNA	10µl	20µl
Restriction enzyme	2U	2U
Buffer(10X)(NEB)	5µl	5µl

Each digest mixture was incubated for 3 hours in a 37°C. Digested PCR product was purified using the QIAquick® PCR purification kit (Qiagen) and the cleaved vector was purified by gel extraction.

2.2.7 Gel Extraction

After complete restriction digestion, the mixture was loaded onto a 1.2% agarose gel and the cleaved vector was separated by electrophoresis. Bands were visualised using UV illumination and the cleaved vector was excised. DNA was extracted from the agarose gel using the commercially available QIAquick® gel extraction kit (Qiagen).

2.2.8 Ligation

Insertion of digested and purified PCR product into digested and purified vector was carried out by ligation at 16°C for 16 hours using the ligation enzyme T4 DNA ligase (New England Biolab). TOP10 competent cells were transformed with the resulting ligation mixture via electroporation (details above) plated onto LB agar plates containing required antibiotics, Kanamycin-50µg/ml and Ampicillin-100µg/ml.

2.2.9   Screening for positive clones

Positive clones were checked as follows:

1. Plasmids were extracted from liquid LB cultures grown overnight. The mobility shifts of the plamids were compared to the vector.

2. Plasmids, which show a mobility shift, were subjected to restriction digestion to check for insert release.

The positive clones are then preserved as glycerol stocks and their plasmids extracted and stored at -20°C.

2.2.10   Sequencing

The positive clones are further confirmed by sequencing. The resulting sequences were compared with the expected sequence using the web based server Multalin (CORPET, 1988).

2.3   Mutant NhaP1 clones

NhaP1 mutants (Hellmer et al., 2003) were received as a kind gift from Prof. Zeilinger from Universität Hannover. The mutants are H211R-H215R, H33R, H425Δ-H426Δ, D93A, D132A, D161A, E156A, R320A, R320D, R320H, R347A. All the mutants were in the vector pTrcHis2TOPO and expression is under control of a trc promoter. A C-terminal fusion peptide, containing a myc-epitope tag for immune detection and a histidine hexamer allowing affinity purification was provided by the plasmid. DH5α strains were transformed with these plasmids. Glycerol stocks were prepared and stored at -80°C.

2.4   Protein expression

2.4.1   Expression strains

For protein expression, *E. coli* expression strains BL21(DE3), BL21(DE3) pLysS, BL21C43 and BL21C41 were transformed with NhaP1$_{His}$, $_{His}$NhaP1 and the

$_{Strep}$NhaP1 . *E. coli* mutants EP432 (nhaA and nhaB deleted in frame) and KNabc (nhaA, nhaB and chaA destroyed by insertion of omega cassettes) were transformed with the above-mentioned mutants. The *E.coli* mutant strains, EP432 and KNabc, were kindly provided by Etana Padan, Hebrew University of Jerusalem, Israel.

2.4.2 Growth media for E.coli mutants EP432 and KNabc

LBK medium: 1% tryptone, 0.5% yeast extract, and 87 mM KCl

2.4.3 Expression by IPTG induction

Glycerol stocks of expression strains transformed with $_{His}$NhaP1, NhaP1$_{His}$, $_{Strep}$NhaP1 and the above-mentioned mutants were streaked onto LB agar plates. The antibiotic selection for $_{His}$NhaP1, NhaP1$_{His}$ is 50µg/ml kanamycin and for $_{Strep}$NhaP1 and the mutants is 100µg/ml ampicillin. The cells are incubated at 37°C for 12hours. A single plate colony was used to inoculate a 5ml LB preculture. The precultures were incubated at 37°C, 180rpm for 16 hours. 1ml of each starter culture were transferred to 5 litre Erlenmeyer flasks containing 2L LB with required antibiotics. The cultures were incubated at 37°C (180rpm), until the OD_{600}=~0.5 (approx. 4-5 hours). Expression was induced with 1mM IPTG and cells were further incubated until an OD_{600} of 3. This protocol is an adaptation from the published results (Vinothkumar et al, 2005).

2.4.4 Large scale Expression in Autoinduction media

Composition of Autoinduction media

* **2x ZY-** Tryptone (2 % (w/v), Yeast extract (1 % (w/v))

* **50x M-** ($Na_2HPO_4.2H_2O$ (1.25 M), KH_2PO_4 (1.25 M), NH_4Cl (2.5 M) Na_2SO_4 (0.25 M)

 * **50x 5052** Glycerol (25 %) glucose (2.5 %) alpha-lactose monohydrate (10 %)

Other reagents: Glycerol (25 %), Glucose (2.5 %), 1.0 M $MgSO_4$, 1.0 M $MgSO_4.7H_2O$

 * **1000x Trace elements (Combination of solution 1 & 2)**

1. 0.1 M $FeCl_3$ in 0.12 M HCl

2. Trace metal mix (25 ml) $CaCl_2.2H_2O$ (40 mM), $MnCl_4.2H_2O$ (20 mM), $ZnSO_4.7H_2O$ (20 mM), $CoCl_2.6H_2O$ (4 mM), $CuCl_2$ (4 mM), $NiCl_2.6H_2O$ (4 mM), $Na_2MoO_4.2H_2O$ (4 mM), $Na_2SeO_3.5H_2O$ (4 mM), H_3BO_3 (4 mM)

Glycerol stocks were plated out on a LB agar plate allowing overnight growth at 37°C. Single colonies were inoculated into 5ml LB media and allowed for growth at 37°C for 7-8 hrs. 2L of Autoinduction media in 5l Erlenmeyer flasks were inoculated with 800ml of this preculture. Cell growth was allowed for 16-18 hrs at 37°C with 150 RPM.

[Method adopted from (Studier, 2005)]

2.5   Protein purification

Important buffers

Lysis buffer: 25mM Tris, pH8.0, 5-10mM DNAse1, 2-4mM PMSF, 0.1mM PefaBLOC and 2mM β-mercaptoethanol

Basic buffer: 25mM Tris pH8.0, 2mM β-mercaptoethanol

Buffer A (25mM Tris-HCl pH 8.0, 10% glycerol, 300mM NaCl, 2mM b-ME, 0.3M 0.05% DDM)

2.5.1   Membrane preparation and solubilization

Cell Lysis: The cell cultures grown as described above, were harvested and resuspended in lysis buffer. The Microfluidizer system was used to break the cells.

Membrane extraction: Cell debris was removed by a low speed centrifugation (Sorvall RC-SB from Du Pont instruments) at 10,000 RPM at 4°C for 30 min. The supernatant was subjected to a round of high-speed centrifugation (Beckman L7 Ultracentrifuge) at 45,000 RPM at 4°C for 90min.

Urea Wash: (*Optional step*) The membrane pellet obtained was resuspended in basic buffer with 3-4 M-urea and ultra-centrifuged at 45,000 RPM at 4°C for 30min.

The pellet was resuspended in the original volume of urea free basic buffer and given another round of ultracentrifugation.

The final membrane pellet was resuspended in the original volume of urea-free buffer. The dilution volume was adjusted so that the final protein concentration in the membrane suspension was 25mg/ml.

Test solubilizations: 200µl of membrane suspensions was used to screen detergents for optimum solubilization. The detergents tested were 2 % n-Octyl β-D-glucopyranoside (OG), 2 % n-Nonyl β-D-glucopyranoside (NG), 1.5 %, Lauryldimethylamine-oxide (LDAO), 1.5 % Cyclohexyl-hexyl-β-D-maltoside (Cymal-6), 1.5 % Cymal-7, 1.5 % 3-[(3-Cholamidopropyl) dimethylammonio]-1-propanesulfonate (CHAPS), 1.5 % 3-[(3-Cholamidopropyl) dimethylammonio]-2-hydroxy-1-propanesulfonate(CHAPSO), 1.5 % FOS-CHOLINE-9, 1.5% n-Decyl-β-D-maltoside (DM), and 1.5% n-Dodecyl-β-D-maltoside (DDM). After solubilization for 30 minutes in room temperature, the fractions were ultracentrifuged at 45,000 RPM at room temperature using a table-top centrifuge. The pellet was resuspended in 200µl buffer. Resuspended pellets and the soluble fraction were analysed by western blot.

Another solubilization test was carried out with 0.2%, 0.4%, 0.6%, 0.8%, 1%, 1.2%, 1.4% and 1.6% DDM in the same way as above.

Solubilization with DDM: For large-scale solubilization, the extracted membrane was incubated with Basic buffer containing 1.5% DDM in presence of 10% glycerol for 45minutes at room temperature with stirring. The solubilized membrane fraction was centrifuged at 45,000 RPM at 4°C for 30min to removed insoluble material. 0.3M NaCl and 10mM imidazole were added to the soluble fraction.

2.5.2 Estimation of total protein concentration

Protein was estimated by the Bradford dye binding method (Bradford, 1976). 500µl of sample was mixed with 500µl of Bradford Reagent (Sigma), incubated at room temperature for 5minutes and absorbance was measured at 595nm. Bovine Serum Albumin (BSA) in the range of 1-10µg was used as a standard for comparison.

2.5.3 Affinity purification

The extracted membrane fraction solubilzed with 1.5%DDM was further purified as follows:

Column equilibration Chelating sepharose from Amersham was washed free of ethanol with water. 50mM $NiCl_2$, equivalent to the 3 column volume (CV) was used to load the column, followed by washing off the unbound $NiCl_2$. 5 CV of Buffer A with 10mM imidazole was used to equilibrate the column.

Lysate loading The soluble fraction was allowed to bind to the pre-equilibrated column material in batch: 5ml column material in 50 ml Falcon tubes was incubated at 4°C for overnight or 90 minutes at room temperature with gentle end to end rotation.

Washing of impurities and elution Buffer A and BufferB (BufferA + 500mM Imidazole) was used in step or linear gradient manner with the Aekta purification system. The protein started eluting after 300mM Imidazole. The pure fractions were collected for concentration.

Detergent exchange (optional) Testing of different detregents to optimize two-dimensional and three-dimensional crystals were carried out by a slow exchange of detergent on the Ni^{2+}-NTA column. This step was carried out after the column was loaded with the lysate. The new detergent was added to Buffer A without DDM. The exchange was initially tested at a miniscale level. The amount of eluted protein is checked on a SDS-page and by analytical gel filtration. For detergents that look promising, the procedure was scaled up to the typical column chromatography, as described above.

2.5.4   Gel filtration

Gel filtration in buffer A was carried out either on a Superdex 200(16/60) or a Superose 6 column (Amesham/Pharmacia). When required the pH of the buffer or the detergent was changed. Analytical gel filtration was carried out with the Superdex 200 PC 3.2/30 (2.4 ml) column.

2.6   Protein detection

Solutions

1. *Stacking and resolving gel*: Acrylamide/bis (30%T, 2.67%C) – prepared by mixing of 29.2 g acrylamide and 0.8g N'-N'bis-methylene-acrylamide, filtered and stored at 4°C in the dark, 1.5M Tris pH8.8, 0.5M Tris pH6.8, 10% SDS, 10% ammonium persulfate (prepared fresh),

2. *Sample buffer*: 0.5M Tris pH6.8 1ml, Glycerol 0.8ml, 10% SDS 1.6ml, 2-mercaptoethanol 0.4ml, 0.05% (w/v) BP blue 0.4ml, water to 8ml

3. *5X Electrode buffer (for a liter)* : Tris 15g, Glycine 72g, SDS 5g

4. *Fixing solution*: 40% of methanol and 35% of formalin

5. *Silver stain conditioning solution* 0.2% stock solution of sodium thiosulfate

6. *Silver stain solution*: 0.1% of silver nitrate solution (prepared fresh)

7. *Developing solution:* 0.3% sodium carbonate, 0.02% sodium

8. *Transfer buffer*: 25 mM Tris 192 mM glycine, 20% methanol (added just before the transfer)

9. *TBS (for washing):* 10 mM Tris pH7.5, 150 mM NaCl and TBS –Tween buffer (TBS +0.05% Tween 20)

10. *Blocking buffer* : 5% milk powder or 3% BSA in TBS

11. *Antibody stock solution* (1:1000) was made in blocking buffer

SDS-PAGE

12% gels were cast with a multiple casting unit from Biorad. After polymerization, gels were stored at 4°C and used up to a month. For sample preparation, the protein sample at desired concentration was mixed with sample buffer (to a final of 1X). Samples were not boiled to prevent hydrophobic subunits from aggregating.

SDS-PAGE staining

Coomassie brilliant blue R250/G250 was dissolved in 45.5% of methanol and 7% acetic acid and filtered before use. Gels were stained for 20 minutes and destained with 5% methanol and 7% acetic acid. This staining procedure is sensitive to the dye binding capacity of the protein (>1µg) (Wilson, 1983)

Silver staining of SDS-PAGE is a highly sensitive method of protein detection and permits detection of nanogram amount of proteins (Switzer, 1979). The gel was fixed for ten minutes and subsequently treated with 300ml of 0.02% STS (conditioning solution). After washing with water (3 x 5), the gel was incubated staining solution for 10 minutes followed by rinsing with water. The gel was developed with 300ml of the developer until the bands started appearing and the reaction was stopped with 5% acetic acid.

Transfer of the protein from the gel to PVDF membrane was carried out with a semi dry blotting system (BIORAD) for 30 minutes at 15V. The membrane was subsequently treated with blocking buffer for an hour and washed 2 times each with TBS-Tween buffer and TBS buffer for 10 minutes. The membrane was allowed to bind primary antibody (His-probe, Santa cruz) for an hour and washed as in the previous step. Subsequently the secondary antibody (goat anti-mouse IgG), a conjugate of horse raddish peroxidase was allowed to bind to the membrane for an hour and washed as before. The membrane was developed immunodetection (Amersham).

2.7 Thin layer chromatography

Solutions:

1. Acidic solvent systems: $CHCL_3$(Chlorofrom)-CH_3-OH(Methanol)-CH_3COOH(Acetic acid)-H_2O in 55:43:3:4

2. Basic solvent system: $CHCl_3$-CH_3OH-NH_4OH (Ammonium Hydroxide)-H_2O 40:70:10:20

The two different solvent systems (acidic and basic) were used to separate different phospholipids (Medh and Weigel, 1989). In the first dimension, the acidic solvent system was used followed by the basic solvent system in the second dimension. The lipids associated with the protein sample (~200-500mg) was extracted with chloroform/methanol (3:1) and dried in nitrogen. The dried sample was re-dissolved in chloroform to a final concentration of 10µg/µl (based on protein concentration as lipid concentration is unknown). A faint line was drawn at ~1cm from the bottom of TLC plates. 1-2µl of the sample and a standard (75µg phosphotidylcholine) were spotted on this base line and allowed to air-dry thoroughly. The first development by ascending chromatography was carried out with acidic solvent, which was stopped before 0.5cm from the top of the TLC plate. The plates were allowed to dry before the second development in basic solvent, which was stopped after the solvent front reached 25% of the earlier solvent front. The plates were allowed to dry and lipids were visualized by exposing the plates to iodine vapour.

2.8   Preparation of lipid stocks

Lipids were obtained from Avanti Lipids as stocks in chloroform. Lipid was dried under argon and traces of chloroform were further removed in vacuum for 2 hours. Lipid was resuspended in 1% of detergent solution to a final concentration of 4-5mg/ml, sonicated until a clear solution was obtained. This stock of solubilized lipid was aliquoted and stored at –20°C.

2.9   Preparation of lipids from *Methanococcus jannaschii*

All glassware was cleaned with chloroform/methanol in the ratio 2:1. 1 volume of cell pellet was mixed with 20 volumes of chloroform/methanol in the ratio 2:1. The mix was incubated for 4 hours at room temperature and filtered using a glass funnel and filter paper. The extract was mixed with I volume of water, 20 volumes of organic phase and five volumes of 0.88% KCl in a separatory funnel at 4°C overnight. The funnel was covered with aluminium foil. The next day, the lower phase was collected and dried in a rotatory evaporator. Approximately 0.2 g of Dextran G-25 was added to remove residual hydrophiles. The lipid extract was then mixed with chloroform and remaining organic solvents were removed by rotatory evaporation. The step was repeated twice before finally removing dextran by passing through sinter filter. The remaining chloroform was removed by rotatory evaporation. The lipid film was resuspended in a defined volume of chloroform and stored in glass bottled with Teflon lids.

2.10   2D Crystallization

1. Dilution buffer: 25mM Na-Acetate pH4.0. This buffer was used with different protein concentration and variety of detergent for optimization.

2. Dilaysis buffer: 25mM Na-Acetate pH 4.0, pH 5.6 and pH 6.0, 5%MPD, 5%Glycerol, 300mM 200mM, 150mM, 100mM, 50mM NaCl, 2mM-4mM β-mercaptoethanol or 2mM –4mM DTT.

Crystallization set-ups with an LPR (lipid to protein ratio) ranging from 0.2-0.7 were screened. The total volume of the set-ups was generally made up to ~ 100µl-150µl

with dilution buffer. The final concentration of purified protein was varied from 0.5mg/ml to 1mg/ml.

The mix was incubated at room temperature for 45 minutes before transferring it to 10mm wide dialysis bags with molecular weight cut-off (MWCO) of 12,000-14,000 kDa. These bags were previously cut into lengths of 6-8cm, and a clip was positioned at 5-10mm at one end. A volume of 50µl-100µl of the crystallization mix was pipetted into the tube followed by closing the other end also at a distance of 5-10mm (Schmidt-Krey, 2007). Flattening of the dialysis bag or removal of any trapped air is avoided. The length of the dialysis bags and the position of the clips in the extreme end proved critical in reproducible recovery of the sample volume. Different temperatures at which dialysis were carried out are 25°C, 30°C or 37°C. The dialysis time varied between 7 and 15 days, during which detergent removal was monitored by electron microscopy.

2.11 Electron microscopy

2.11.1 Negative stain and screening

2µl of the dialyzed sample was allowed to adsorb on a carbon coated copper grid of 400 mesh for 30 seconds. 3 drops of 100µl 1% uranyl acetate were pipetted on Parafilm. The grid with the sample was washed in two drops and floated for a few seconds on the third and blotted on a filter paper. The grid was then allowed to dry on the tweezers for one minute. Any debris from the buffer was washed away in the first two drops. The grids were screened in a Philips CM120 or FEI G[2] Tecnai Spirit electron microscope equipped with a LaB_6 filament and operating at 120kV. Images were recorded by a CCD camera with 2k x 2k or 1k x 1k pixels or in Kodak SO-163 film, typically at a magnification of 35,000 with an exposure of 20 electrons per $Å^2$. The negatives were developed in Kodak D-12 developer for 12 min, washed for1 min and fixed for 8 min. A prolonged wash of 30 minutes was carried out before allowing the negatives to dry. The quality of data recorded by a CCD camera was evaluated by Fourier transfrom calculation. Negatives were analysed by optical diffraction for assessing the quality of the 2D crystals.

2.11.2 Cryo-specimen preparation

Specimens for cryo-electron microscopy were prepared by the back injection method (Wang and Kuhlbrandt, 1991). A fresh piece of carbon was floated from mica on an embedding medium of choice (typically 4% glucose or 4.5% trehalose). A copper or molybdenum grid was used to pick up the carbon film. The sample was applied to the side opposite to where the supporting film is present. The sample and the embedding medium were mixed several times. An incubation time of 1 minute was allowed before removing out a volume of 2µl off the grid. The grid was blotted on a double Whatman 4 filter paper for 20 seconds and air dried for 5 seconds before plunging into liquid nitrogen.

For data collection at 0° tilt, 20Å-30Å thick carbon film was used. In case of specimen prepared for recording images at high tilt (30° and 45°), thicker carbon of 80Å-100Å was used. Data collection at 45° was also carried out with 50Å-100Å titanium-silicon (TiSi) film (Rhinow and Kuhlbrandt, 2008) instead of carbon film. A prior step of moistening the TiSi film on a wet filter paper is required for floating it off conveniently.

2.11.3 Cryo-electron microscopy

Data collection was carried out in the JEOL 3000 SFF electron microscope equipped with a field emission gun and a liquid helium cooled top entry stage (Y. Fujiyoshi, 1991). Images were recorded at an accelerating voltage of 300 kV at a specimen temperature of 4K and a magnification of 70000x. The spot scan procedure (Downing, 1991) with an exposure time of 35 ms per spot and spot size 5 was used for collecting data of 0° and 20° tilted specimen. The exposure time and spot size was changed to 32ms per spot and 4, respectively, for 30° and 45° tilted specimen. Images recorded on Kodak SO-163 electron emulsion film were developed for 12 min in full strength Kodak D19 developer.

2.11.4 Screening and digitizing of negatives

After evaluating individual images by optical diffraction good crystalline areas showing diffraction spots to 10Å or better were marked for scanning. Optical diffraction was also used as a tool to analyse the effect of imaging parameters like defocus, astigmatism and to identify defects such as specimen drift. Areas of 6000 × 6000 pixels were selected and digitized by a Zeiss SCAI scanner with a scanning

pixel size of 7 µm, corresponding to a pixel of 1Å on the specimen. The program TIF2MRC was used to convert the images to MRC format for data processing by the MRC image processing software package (Crowther, 1996) .

2.11.5 Single image processing

Data processing for the digitized images were carried out with the MRC (Medical Research Council, UK) suite of programs (Crowther, 1996). To avoid spikes in the Fourier transform, a smooth gradient of optical densities across the edge of the MRC formatted images was created by the programme TAPEREDGE. The program LABEL was used to average adjacent pixels and create a reduced copy of the image. FFTRANS was then used to calculate a Fourier transform of the image for determining lattice parameters. The Fourier transform was visualized by the graphics program XIMDISP (Smith, 1999).

The unit cell parameters were determined by manually selecting reflections in the Fourier transform. The root mean square error for the lattice fit after each new spot selected was restricted to ≤ 0.5. Three important points in indexing are:

1. Avoiding fuzzy spots and selecting only sharp reflection.

2. Including reflections to as high a resolution as possible.

3. The Friedel mates of the chosen reflections were indexed to avoid

    offset of the fitted lattice from the true transform origin.

Noise was removed in Fourier space by masking the diffraction spots by the program MASKTRANA. As a result only selected part within the mask have non-zero values. Subsequently, lattice distortions in the original image are identified by cross-correlation with a tightly masked reference using the program TWOFILE in reciprocal space. A real space cross-correlation map is generated that enabled the program QUADSERCHK to identify the exact position of cross-correlation peaks. 2-3 rounds of correction of crystal deformation by CCUNBEND improved the quality of data by manifold. MMBOXA was utilized to retrieve and list the phase and amplitude for each reflection. Finally, the defocus and astigmatism were determined using CTFFIND3 and these values were applied using CTFAPPLY for correction of the phase data for the effect of the contrast transfer function.

2.11.6 Merging of 0° tilt data

To calculate a projection map, data from several untilted images were merged. The crystal plane group symmetry was determined using the program ALLSPACE (Valpuesta et al., 1994). To start the merging process the best image based on resolution and overall phase residual was selected as the reference. The phase origin for every 0° tilt image was refined against this reference using ORIGTILTD (NPROG=1). The merging is finally carried out with ORIGTILTD, NPROG=0). The CCP4 program suite was used to create projection maps.

2.11.7 Difference map

Difference maps were calculated using phases and scaled amplitudes of structure factors obtained for wild type MjNhaP1 and mutant R347A. Differences from 1 to 4 σ are plotted with each contour representing 0.5σ. Positive densities are blue, negatives are red.

2.11.8 Tilt geometry and Handedness determination

Generally, the crystal tilts are different from the nominal tilt indicated by the sample holder and deviations of ±5-8° are commonly observed (MRC documentation, Unger and Cheng). Therefore, to build up 3D data set, a crucial step is determination of accurate tilt geometries. The program EMTILT was used to determine the tilt angle and the direction of the tilt axis for each tilted image from the reciprocal lattice vector lengths. The sign of the tilt angle was determined as follows:

1. The direction of the tilt axis was determined for each of the tilted image by moving the micrograph and noting the direction where the Thon ring pattern is constant.

2. The position of less and more defocus was determined by moving the micrograph in the direction perpendicular to the tilt axis. Larger thon ring means less defocus and vice versa.

A

B
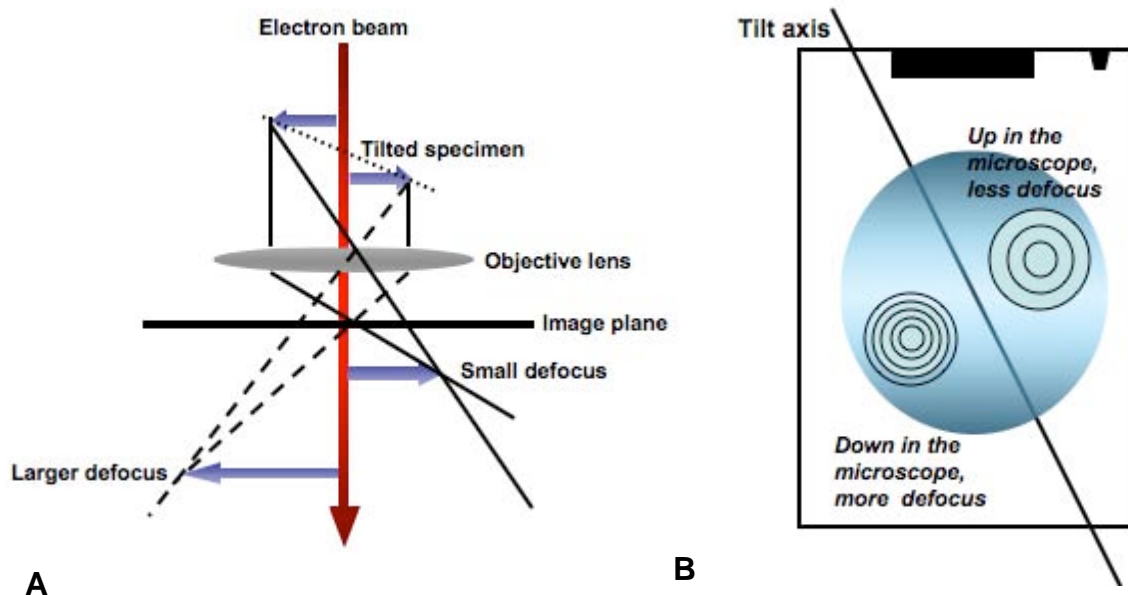
Figure 10 Schematic representation of the relation between specimen height in the column and the defocus gradient observed in the micrograph. A.The simplified ray diagram illustrates that parts of the specimen that are higher up in the column, will be imaged at a lower underfoucs if the objective lens current is held constant. B. By optical diffraction this relation can be directly observed by comparing the Thon ring pattern on either side of the tilt axis. The part of the micrograph that displays fewer and more separated Thon rings is at lower underfocus. Accordingly, this part of the specimen was higher up in the column. (Figure adapted with changes from a handout on "2D- structure determination" by Vinzenz M. Unger, Yale University).

3. The relationship between the two lattice vectors a* and b* and the direction of tilt axis are taken into account for assigning the sign of reciprocal height vector z*. In a right handed coordinate system if b* is counter clockwise from a*, +z* points towards the observer and if b* is clockwise from a*, +z* points away from observer. The assignment was verified taking the bacteriorhodopsin structure as a model. Accordingly, the assignment of the sign of tilt angle depending on the handedness of the vectors is depicted below.
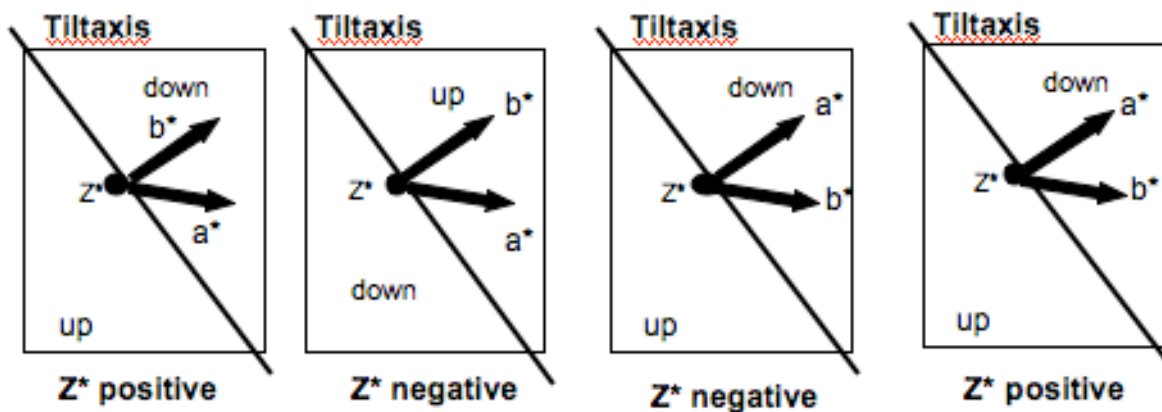
Figure 11 Assignment of the sign for the tilt angle (TANGL). The sign of the z* value for the (1,0) or (0,1) reflection, i.e. the sign of z* along a* and b* is established. The "up" or "down" position of the part of the micrograph in the microscope column determined by optical diffraction (Fig.10) and these attributes are linked with parts of the molecular transform "rising above" or "falling below" the plane of the micrograph ("central section"). Lastly, depending on whether the z* axis is pointing towards or away and at the same time if a* is "rising above" or "falling below" the "central section". This information is used directly to check if the central section intersects the (1,0) lattice line at positive or negative z* values. Once the z* sign for the (1,0) is known the sign of TANGL is determined and compared to the output of ORIGTILT. (based on a handout on "2D- structure determination" by Vinzenz M. Unger, Yale University)

2.11.9 Generation of 3D density

The image data were brought to a common phase origin and merged in reciprocal space assuming p22$_1$2$_1$ symmetry (ORIGTILT). The 0° reference was obtained by merging 14 individual images of 0° tilt. Tilted data were added sequentially to the reference in order of increasing tilt angles. The tilt geometries and phase origins of the merged data were refined until convergence. The phased data were weighted according to the intensity of the reflections (IQ) (LATLINEPRESCAL) and continuous amplitude and phase functions were fitted via a least-squares procedure to each set of X/Y reflections (LATLINE). A list of structure factors were produced by sampling the resulting continuous molecular transform at intervals of 1/150Å(0.007Å^{-1}) for each X/Y reflection. These were converted to mtz format (F2MTZ) and Fourier transformed (FFT) to create an electron density map of NhaP1. F2MTZ and FFT are part of the ccp4 software package (CCP4 94) and ORIGTILT, LATLINEPRESCAL and LATLINE are part of the MRC suite of programmes (Crowther et al., 1996).

2.11.10 Docking of NhaA X-ray Structure

The PDB file 1ZCD of the NhaA X-ray structure was fitted manually into the 3D map pf NhaP1. The fitting was carried out in the graphics program Coot.

2.11.11 MjNhaP1 model building

The NhaA X-ray PDB file (1ZCD) monomer was used as a template to build the NhaP1 model. The model building was carried out in the graphics program Coot.

2.12 3D Crystallization of NhaP1$_{His}$

Sitting drop vapour diffusion was used to screen conditions for 3D crystal formation of NhaP1$_{His}$. In this technique, equilibration occurs by diffusion of liquid vapour from the protein drop to the liquid in the reservoir (mother liquor) and vice versa. The concentration of NhaP1$_{His}$ used for the screening process varied for 5mg/ml to 15mg/ml. 0.3µl of purified protein was mixed with 0.3µl of mother liquor and the pipetting procedure was carried out in 96 well plates using the crystallization robot. The protein/reservoir liquid is placed in a small well above the bigger well with the mother liquid. The two wells are sealed within the same chamber with a cover slip or transparent tape allowing equilibration. The commercially available crystal screen of Hampton I & II, and Jena biosciences were used for initial screening. Secondary screen for optimization was done by manual hanging drop method in 24 well Limbro plate. Conditions were optimized from promising hits in the screening plate. Generally, 0.5µl to 1µl protein conditions were mixed with 0.5µl, 1µl or 2µl of mother liquor during the optimization process.

2.12.1 Crystal Freezing and Data collection

Crystals of NhaP1 were mounted in a cryo-loop (Hampton Research) and transferred to 1µl of cryoprotectant (mother liquor containing a mix of paraffin and paratone) for few seconds before being flash-frozen in liquid nitrogen. Diffraction data was collected at the ESRF, European Synchrotron Radiation Facility Grenoble, France (https://www.esrf.fr).

2.13 Sequence alignment

Sequences of Na$^+$/H$^+$ exchangers (or antiporters) belonging to different families were downloaded from protein database (http://www.ncbi.nlm.nih.gov/PubMed/). Initial alignments were made using CLUSTALW and the preliminary predictions for hydrophobic segments were carried out with TMHMM, Tmpred. The transmembrane segments of the X-ray structure of E.coli NhaA (Hunte et al., 2005a) was used as a template for the initial alignment. The final alignment was manually modified taking into account sequence conservation present in corresponding transmembrane helices. The web based software **_Jalview_** (Clamp et al., 2004) was used for editing the alignment. Details about the different Na$^+$/H$^+$ exchangers (antiporters) used in the sequence alignment are given in the table below.

Table 1

Name	Accession mumber	Source Organism	Family	Length
NHE6a	NP_001036002	_Homo Sapiens_	CPA1	701
Nhx1	EDN60776	_Saccharomyces cerevesiae_ YJM789	CPA1	633
Nhx1	NP_198067	_Arabidopsis thaliana_	CPA1	538
NHE3	NP_004165	_Homo sapiens_	CPA1	834
NHE1	SL9A1	_Homo sapiens_	CPA1	815
Mj0057 (NhaP1)	Q60362	_Methanococcus jannaschii_	CPA1	426
PAB1518 (NhaP)	CAB50204	_Pyrococcus abyssi_	CPA1	443
MK0552 (NhaP)	NP_613837	_Methanopyrus kandleri_	CPA1	434
NhaA	NP_414560.1	_Escherichia coli_	CPA2	388
NhaA	AAX63940	_Salmonella enterica_	CPA2	388
NhaA	ZP_01261277	_Vibrio alginolyticus 12G01_	CPA2	383

3 Results

3.1 Cloning of NhaP1

The gene Mj0057 encodes the Na^+/H^+ antiporter in *Methanococcus jannaschii*. Vinothkumar et al. have previously cloned this gene into the *E.coli* expression vector pET26b (Novagen) using the restriction enzyme *Nde*1 and *Xho*I, thus introducing a hexa-His-tag to the C-terminus end of the gene. The resulting clone was called MjNhaP1 (Hellmer et al., 2002; Vinothkumar et al., 2005). In this work, we refer to it as $NhaP1_{His}$. Expression of $NhaP1_{His}$ in the *E. coli* strain BL21 pLyS, yielded 0.5-0.7 mg of pure protein per litre culture (Vinothkumar et al., 2005). This amount was sufficient to obtain 2D crystals but limiting for extensive screening and optimization of 3D crystals. Therefore, to increase expression level and get monodisperse preparations of MjNhaP1, the gene encoding MjNhaP1 was cloned into different expression plasmids. The gene for MjNhaP1 was successfully amplified by PCR using $NhaP1_{His}$ as a template. Typically, 10µg of amplified DNA was recovered from each PCR reaction. Ligation of the amplified gene product into linearized plasmid (2.2.2) gave positive clones as confirmed by sequencing. The two positive clones are:

1. $_{His}NhaP1$ - MjNhaP1 was cloned into the vector pSKB2LNB (2.2.2). Here gene expression is controlled by the T7 promoter and the resulting MjNhaP1 protein has an N-terminal hexa-His tag. The aim of designing this clone was to test the effect of the position of Hexa-His tag (from C-termial to N-terminal end of the gene) on the expression level and on the purification quality of recombinant MjNhaP1.

2. $_{strep}NhaP1$- MjNhaP1 was cloned into the vector pASKIBA13plus (2.2.2). Here gene expression is controlled by a Tet promoter and the MjNhaP1 protein has a N-terminal Strep tag II. The aim of designing this clone was to test the effect of Tet promoter on the expression level and to check if replacement of Hexa-His tag by Strep tag II improves the preparation of monodisperse MjNhaP1.
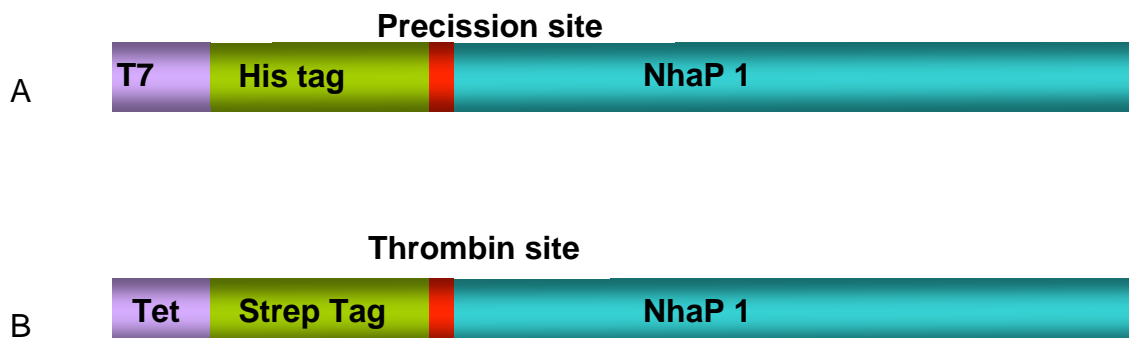
Figure 12 Expression constructs with two different tags for purification by affinity chromatography. (A) MjNhaP1 is cloned into pSKB2LNB vector under a T7 promoter and an N-terminal his tag with a preScission cleavage site (B). MjNhaP1 is cloned into pASKIBA-13 vector under a tet promoter and a N-terminal strep tag with a thrombin cleavage site.

3.2   Optimization of expression

3.2.1   Expression optimization of NhaP1

As mentioned earlier (3.1) expression of NhaP1$_{His}$ in the *E. coli* strain BL21 pLyS, yielded 0.5-0.7 mg of pure protein per litre culture (Vinothkumar et al., 2005). This clone has been used in the current work for 3D crystallization. 3D crystals have been obtained using purified NhaP1$_{His}$ (2.5) under various conditions (2.12). However, diffraction spots of these 3D crystals using X-ray were observed only up to a resolution of 7-8Å. To improve diffraction quality it was necessary to carry out extensive screening and optimization of various crystallization parameters. The yield of pure protein as optimized by Vinothkumar et al was limiting for 3D crystallization experiments. Therefore, to improve expression levels of NhaP1$_{His}$, various conditions like different temperatures, *E. coli* strains, induction time for expression, amount of the inducer IPTG and different growth media were explored. Both the strains BL21 (DE3) C41 & C43 showed a two fold increase in expression levels compared to BL21 pLysS. However, the most significant improvement was found when cells were grown for expression in autoinducing medium (AI) (2.4.4). NhaP1$_{His}$ expressed in AI medium 37°C yielded 2-2.5mg of pure protein per litre of culture. No expression was

observed at lower temperature. The optical density, (OD_{600nm}) of cells grown in autoinduction medium reaches 7-8 compared to an OD_{600nm} of 3 for cells grown in LB, 2YT or TB media under same growth conditions.
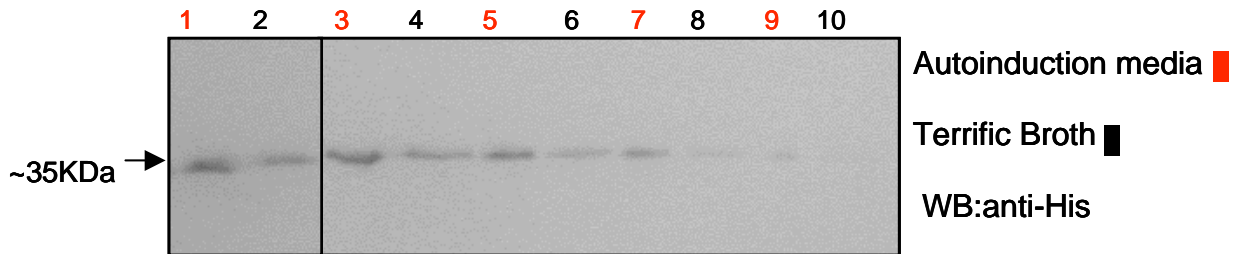

Figure 13 Analysis of NhaP1$_{His}$ expression by western blot. Comparison of expression levels of NhaP1$_{His}$ in Terrific broth medium and Autoinduction medium. 12%SDS page analysed by anti-His antibody. Lane 1: NhaP1$_{His}$ in Autoinduction medium, Lane 2: NhaP1$_{His}$ in Terrific broth. In lane 1 & 2 equal OD of cells were loaded. Lane 3,5, 7, 9- NhaP1$_{His}$ in Autoinduction medium. Lane 4,6, 8,10: NhaP1$_{His}$ in terrific broth. In lane 3-10 equal volumes of cells were serially diluted for comparing expression levels.

The clone $_{His}$NhaP1 showed a two-fold higher expression level than NhaP1$_{His}$. Expression level of $_{His}$NhaP1 was highest at 37°C in the autoinduction medium. The highest expression level for both $_{His}$NhaP1 and NhaP1$_{His}$ were obtained at 37°C using the *E.coli* host strain BL21 (DE3) C43. The construct $_{Strep}$NhaP1 showed very low expression under all conditions tested.

Figure 14 Comparison of expression level of different constructs. Cells expressing MjNhaP1 were subjected SDS-PAGE followed by a western blot using a nitrocellulose membrane. The recombinant fusion protein was tagged with an Anti-His primary antibody(2.6) followed by detection with an anti-mouse secondary antibody coupled to horse raddish peroxidae. Lane1. NhaP1$_{His}$ Lane 2. $_{His}$NhaP1. Lane 3. Purified NhaP1$_{His}$ as positive control. Lane 4. Lower molecular weight marker (Sigma).
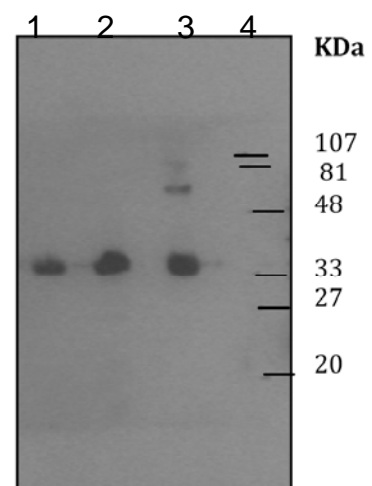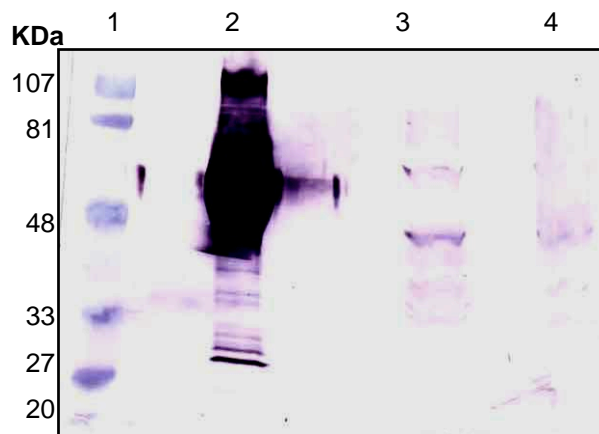
Figure 14 Western blot of $_{Strep}$NhaP1 for checking expression level. Cells were subjected to 12% SDS-PAGE and western blot analysis. Anti-strep tag antibody has been used as the primary antibody and a secondary antibody conjugated to alkaline phosphatase was used for detection of the recombinant fusion protein. Lane 1: Molecular weight standard, Lane2: BetP purified protein was used as positive control Lane 3: $_{Strep}$NhaP1 in whole *E. coli* cells lane4: pASKIBA13 vector as negative control

3.2.2 Expression optimization of NhaP1 mutants

MjNhaP1 mutants (Hellmer et al., 2003) were obtained as a gift (2.3). Secondary structure prediction of MjNhaP1 highlighting the amino acids selected for mutagenesis is shown below (Figure 15). Functional characterizations of these mutants have shown that asparate and arginine residues are required for antiporter activity 1.5.2.3 (Hellmer et al., 2003). Three primary reasons for working towards optimizing the expression levels of MjNhaP1 mutants are: (a) To check if the expression level is higher than the wild type NhaP1$_{His}$ (b) To check their monodispersity after purification (c) to improve the diffraction quality of both 2-dimensional and 3-dimensional crystals. Point mutation has been a valuable tool in protein engineering for improving crystal packing.

Initially, BL21(DE3) pLysS cells were transformed with the mutant MjNhaP1 clones i.e vector pTrcHis2TOPO containing various point mutations for the gene encoding MjNhaP1 2.3 under a trc promoter. The transformants with D132A, R320A, D93A failed to grow in LB media although the *E.coli* strain BL21 DE3 (pLysS) contained an endogeneous gene for Na$^+$/H$^+$ antiporters. The remaining transformants with H211R-H215R, H33R, H425Δ-H426, D161A, E156A, R320D, R320H, R347A grew in LB media and protein expression was detected for the mutants D156A and H211R-H215R.
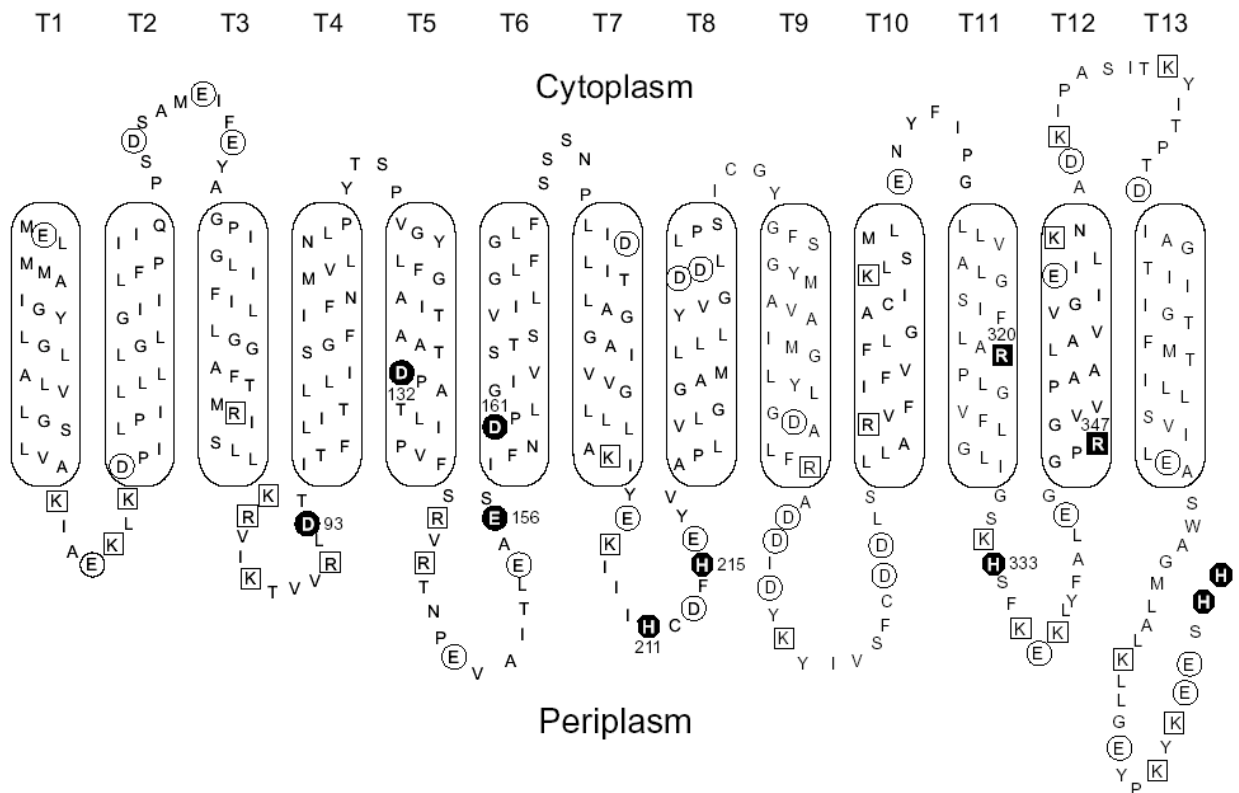
Figure 15 The topological model was based on the secondary structure prediction using the Kyte and Doolittle algorithm of Protean (DNA-Star). In circles: acidic residues (D, E). In squares: strongly basic residues (R, K). In octagons: histidine residues. Closed symbols indicate the residues selected for mutagenesis. Transmembrane domains (T) are numbered above the model (Hellmer et al., 2003).

To find better expression conditions, the *E.coli* strains EPR432 and KNabc were transformed with mutated MjNhaP1 clones. These two *E.coli* strains lack the genes for NhaA and NhaB and fail to grow in a NaCl environment. A higher number of transformants, R347A, R320A, R132A, D156A, H211R-H215R, H333R and E161A, could be grown in a LBK media. EPR432 and KNabc transformed with R347A, R320A, R132A, D156A were selected for further expression optimization as arginine and aspartate residues have been shown to be functionally essential for antiporter activity (Hellmer et al., 2003). In addition to these, EP432 and KNabc transformants with H211R-H215R and EPR432-H333R and KNabc-E161A were randomly selected for the expression test. Amongst all the mutants, R347A in KNabc grown in LBK media appeared promising for purification and crystallization trials.
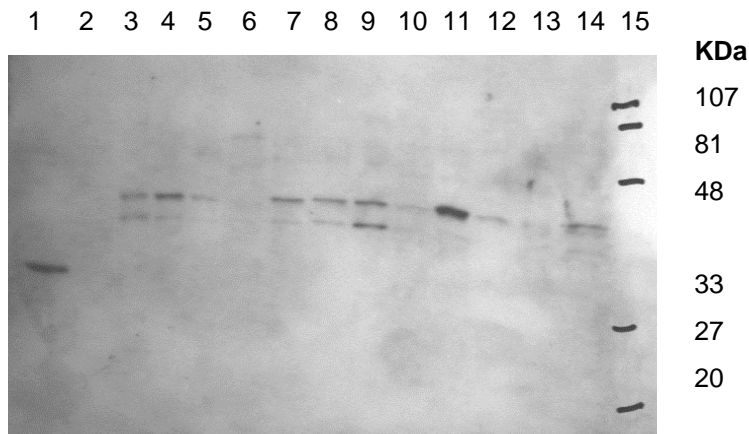
Figure 16 Western Blot analysis to check expression level of the MjNhaP1 mutants. Anti-His antibody is used as the primary antibody and a secondary antibody coupled to a horse raddish peroxidase is used for detection. Lane 1-Lane 15: (1) EPR432-NhaP1$_{His}$ (2) EPR432-R347A (3) EPR432-R320A (4)KNabc-D156A (5) EPR432-D156A (6) KNabc-NhaP (7) EPR R132A (8) EPR-H333R (9) EPR H211R-H215R (10) KNabc R132A (11) KNabc R347A (12) KNabc R320A (13) KNabc H211R-H215R (14) KNabc E161A (15) Molecular weight standard

3.3   Purification

3.3.1   Purification of NhaP1$_{His}$

NhaP1$_{His}$ was purified according to Vinothkumar et al. with a few modifications (2.5). Protein purified by Vinothkumar's method contained a few contaminations with a molecular weight similar to NhaP1$_{His}$. To remove these proteins, washing of the membranes in 3-4M Urea was carried out. This washing step appeared to remove the impurities but unfortunately, the stability of NhaP1$_{His}$ was also affected as a proportion of of the protein was found in the Urea soluble fraction. Urea soluble and insoluble fractions could be separated by ultracentrifugation 2.5.

Including 10% glycerol during the solubilization process with 1.5% DDM improved the stability of the protein and decreased non-specific binding to the Ni^{2+}-NTA column. The purity of the eluted protein was improved futher by including 1M NaCl in the wash buffer. Also, a longer wash using approximately 40-column volume wash buffer helped in improving the purity. The most effective method, which removed most of the impurities with a molecular weight similar to NhaP1$_{His}$ was by using a gradient of imidazole in the wash and elution buffer during the purification process using the Äkta system (2.5.3).
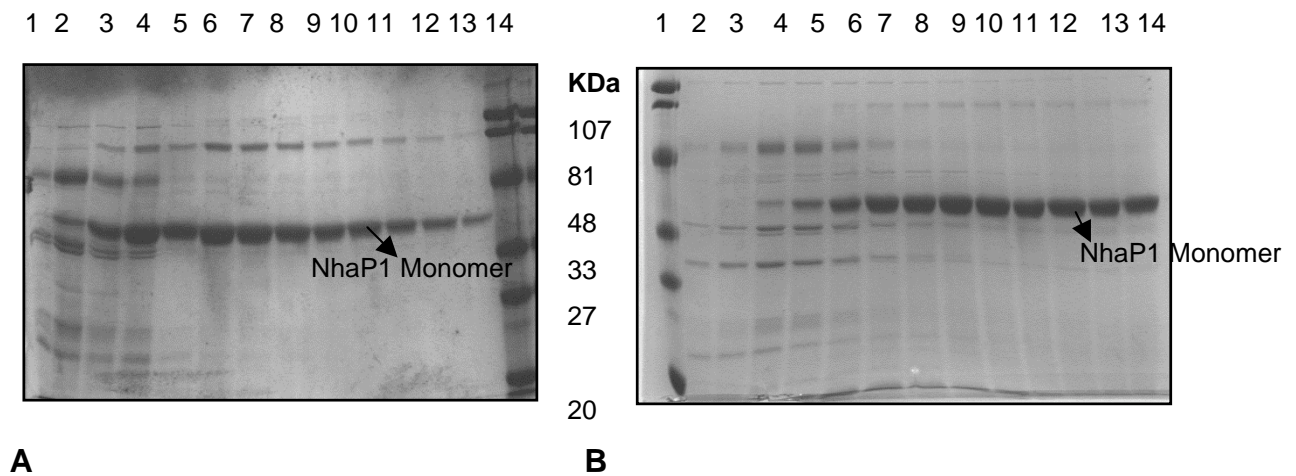
Figure 17 **SDS-PAGE analysis NhaP1$_{His}$ at different purfication stages. Lane 1-Lane 13 in (A) and Lane 2-Lane 14 in (B) shows fractions of NhaP1$_{His}$ eluted from Ni^{2+}-NTA column with a step and gradient increase of imidazole concentration. (A) Elution fraction of NhaP1$_{His}$ over-expressed in TB media induced by IPTG (B) Elutioin fraction of NhaP1$_{His}$ over-expressed in autoinduction media. Comparison of (A) and (B) shows the increase in protein yield by the method of autoinduction. Lane 14 in (A) and Lane 1 in (B) are molecular weight standards**

3.3.2   Detergent exchange on the Ni^{2+}-NTA affinity column

To optimize both 2D and 3D crystals of NhaP1$_{His}$ different detergents need to be tested for purification. Since NhaP1$_{His}$ solubilises best in buffer containing 1.5% DDM, It was decided to exchange the detergent prior to elution from the Ni^{2+}-NTA column. A number of detergents were investigated and NhaP1$_{His}$ eluted in a buffer containing 1.5% OG showed highest purification quality as analysed by Coomassie and silver stained SDS-PAGE. Analysis by size exclusion chromatography showed a symmetric peak corresponding to the expected molecular weight of NhaP1$_{His}$ and only a small aggregate peak. However, the protein was stable only for 12 hours after elution as determined by analytical gel filtration. Therefore, the purified protein had to be used immediately for 2D crystallization trials. Detergent exchange was also carried out by buffer exchange in a gel filtration column. Such studies by size exclusion chromatography show that the protein is also stable in several other detergents like 0.1% DM, 0.1% UDM, 0.06% Cymal-6, 0.06% Cymal-7. The purification of NhaP1$_{his}$ in these detergents however requires further optimization.
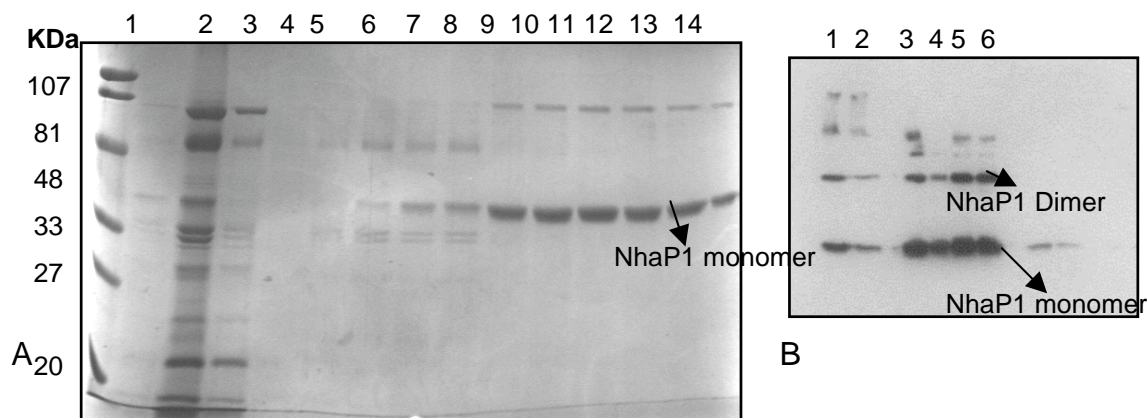
Figure 18 SDS-PAGE analysis of NhaP1$_{His}$ purified in buffer containing 1.5% OG. A. Membranes solubilized with 1.5% DDM were loaded onto Ni^{2+}-NTA column and eluted by exchanging to a buffer containing 1.5% OG. The different fractions of the purification process analysed on Coomassie stained SDS-PAGE. L1-L8: Fractions from preliminary washes with a gradient increase of imidazole in the buffer. L9-L14. NhaP1$_{His}$ elution fractions. B. Fractions from analytical gel filtration analysed on a silver stained SDS-PAGE. 50µl of elution pool from Ni^{2+}-NTA was loaded onto the Superdex200. Fractions in L1 &L2 correspond to the void volume and fractions in L3-L6 correspond to elution volume of 1.5.

3.3.3 Elution of NhaP1$_{His}$ by pH shift

2D crystals had been obtained with purifed NhaP1$_{His}$ at pH 4.0 (Vinothkumar et al., 2005). A preference towards lower pH was also observed in 3D crystallisation trials. The protein in both cases was dialysed into a buffer at pH 4.0. Moreover purified NhaA$_{His}$ showed a tendency to aggregate when kept at alkaline pH for longer duration. For these reasons, NhaA$_{His}$ was eluted from the Ni^{2+}-NTA column at pH 4.0. NhaP1$_{His}$ purified by this process was stable for a longer duration and showed a homogenous peak when analyzed by size exclusion chromatography. However, the purity of the eluted fractions required optimization.
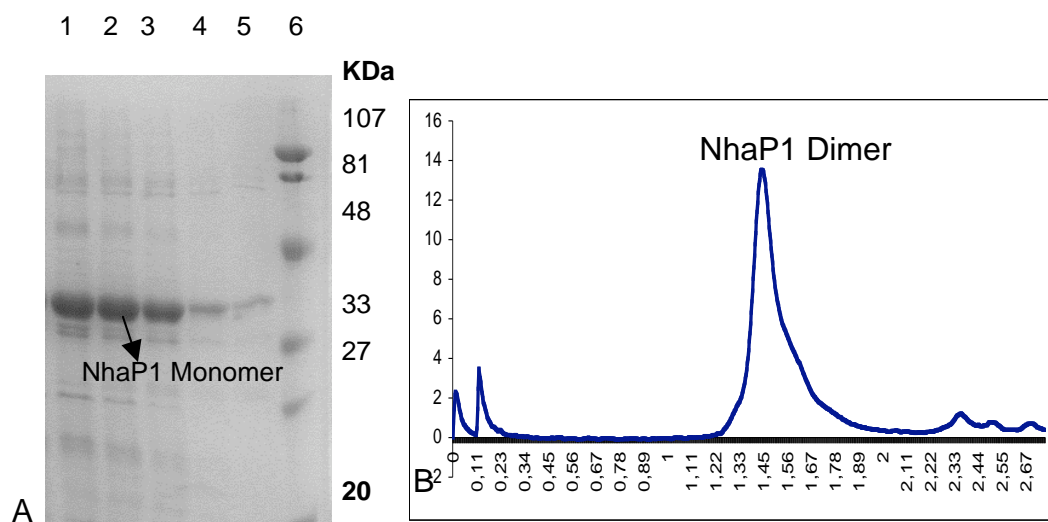
Figure 19   Purification of NhaP$_{His}$ by a shift to acidic buffer (A) L1-L5, Ni^{2+}-NTA elution fractions at pH4.0. NhaP1$_{His}$ was loaded to the Ni^{2}+-NTA column in BufferA at pH 8.0. The protein was eluted by shifting to the acidic buffer Na-Acetate at pH 4.0. 6, Molecular weight standards. (B) Analytical gel filtration on Superdex 200 using the SMART system. 50µl of the elution pool from Ni^{2+}-NTA were loaded onto the Superdex 200. The total amount of NhaP1$_{His}$ represented by the peak is ~50µg.

3.3.4   Purification of $_{His}$NhaP1

During this work MjNhaP1 was cloned into modified pET vector fused to a N-terminal Hexa-Histidine His tag. This clone has been termed in this work as $_{His}$NhaP1. Purification trials were carried out for the purpose of 2D and 3D crystallization. Since NhaP1$_{His}$ could be purified successfully from Ni^{2+-}NTA column, the same methodology was used to purify $_{His}$NhaP1.

$_{His}$NhaP1 bound efficiently to Ni^{2+}-NTA column and was eluted in Buffer A containing 300mM Imidazole. The Hexa-His tag was cleaved with PreScisson enzyme 2.2.2 after affinity purification. The time required for complete cleavage was determined by Western blot analysis. Complete cleavage was observed after 1-2 hours at room temperature using 1 Unit PreScission enzyme per 50ug protein. $_{His}$NhaP1 could not be eluted from the Ni^{2+}-NTA column by cutting the tag with PreScission enzyme on the Ni^{2+}-NTA column.
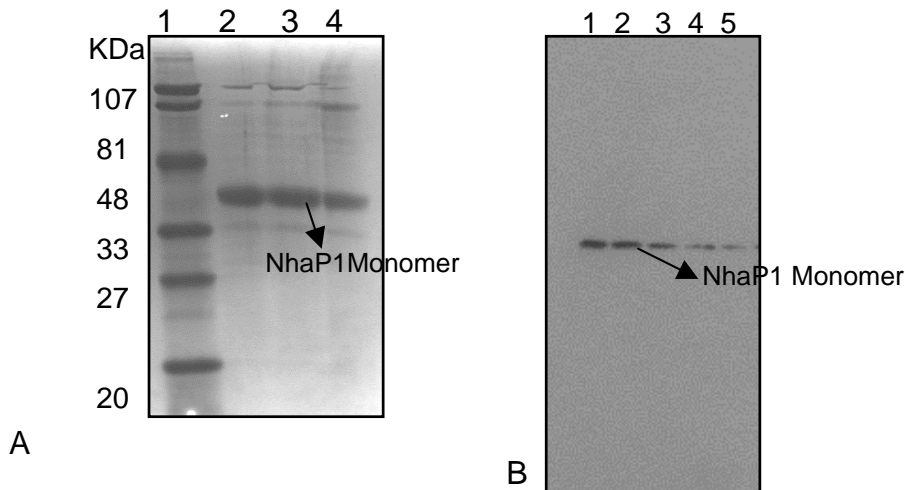
Figure 20 SDS-PAGE analysis of HisNhaP1 purified by affinity chromatography . (A) Analysis of HisNhaP1 fractions after 2-step purification. The elution fractions from the Ni^{2+}-NTA column were loaded to Superdex 200 16/60 column. The fractions, L2-L4, are analysed on a Coomassie stained SDS-PAGE, 1, Molecular weight standard. (B) Western Blot detection by anti-His antibody. Elution pool of HisNhaP1 from the Ni^{2+}-NTA column was incubated with PreScisson enzyme. L1-L5, 10µl of sample from different time point of incubation were loaded onto a SDS-PAGE. L1: 0 minutes L2: 15 minutes L3: 30 minutes L4: 45 minutes L5: 1hour

3.3.5 Purification of the MjNhaP1 mutant R347A

Optimization for higher yield revealed that R347A expressed in the bacterial strain BL21(DE3) pLysS in autoinduction media gave the highest quanitiy of purified protein. Membranes obtained from 6 litres of cells were resuspended with buffer A containing 1.5% DDM. R347A contains a hexa-histidine tag in the C-terminus, which enabled purification by Ni^{2+}-NTA chromatography according to the protocol optimized for NhaP1$_{His}$. Most impurities were washed away with 60mM imidazole and the protein could be eluted homogeneously with 300mM Imidazole.
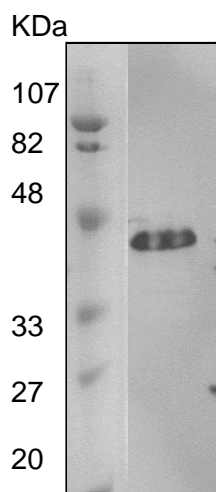
Figure 21 Purification of R347A by Ni^{2+}-NTA. Western Blot analysis of R347A purified on the Ni^{2+}-NTA column. Anti-His antibody is used as the primary antibody and a secondary antibody coupled to a horse raddish peroxidase is used for detection. Western blot was carried out to check for degradation products.

3.4 Three-dimensional crystallization of NhaP1$_{His}$

3.4.1 Effect of Purification conditions on 3D crystal formation

3D crystallization experiments were carried out with purified NhaP1$_{His}$. Production and purification comprised of a two-step purification process, immobilized metal affinity chromatography (IMAC) followed by gel filtration. The protein is virtually pure, stable and of homogenous oligomerization state as shown by analytical gel filtration (Figure 19 and appendix II). The purification procedure was shortened to improve crystal quality, since extensive delipidation has been shown to affect stability, activity and crystallization performance of membrane proteins (Palsdottir and Hunte, 2004). Further, there can be loss of protein yield with the second purification step. Therefore, the gel filtration step was omitted leaving a one-step IMAC purification. The new procedure was faster and did not affect NhaP1$_{His}$ yield, quality and purity as analyzed by gel filtration and SDS-PAGE. NhaP1$_{His}$ purified by this process formed 3D crystals under several conditions (3.12.2). However, no improvement was observed in the X-ray diffraction pattern.

Some batches of protein from the Ni^{2+}-NTA column appeared brown in colour and this kind of coloured protein solution never crystallized. A TLC analyses was carried out to detect the presence of any characteristic lipids. By TLC analysis no lipid, which could explain the colour, could be detected in the protein solution (Figure 22). The second purification process by gel filtration chromatography reduced the colour considerably and this protein yielded 3D crystals reproducibly. Washing the protein on the nickel column with a buffer containing 0.1%DDM and subsequent elution of

the protein in this high detergent concentration was another procedure used to remove the brown colour. However, this excess detergent had to be removed to avoid detergent crystals as often seen in the crystallization drops. The use of Vivaspin concentrator of 100 KDa cut off followed by dialysis against a buffer with 0.05% detergent helped to reduce the excess detergent.

The crystals of NhaP1$_{His}$ purified in DDM almost always showed plate-like in shape and had poor growth in the 3rd dimension. In order to perform 3D crystallization experiments with NhaP1$_{His}$ in the presence of other detergents, an exchange of DDM to OG and Cymal-6 was carried out on the Ni^{2+}-NTA column during the washing step. NhaP1$_{His}$ in OG tended to aggregate and hence never crystallized. Nevertheless, a set of screens of NhaP1$_{His}$ purified in DDM and incubated with 1% OG showed the formation of 3D crystals. NhaP1$_{His}$ in a buffer containing 0.06% Cymal-6 yielded 3D crystals comparable to DDM crystals.

Another important consideration for 3D crystallisation was the buffer containing the purified NhaP1$_{His}$. The presence of glycerol and salt in the final purification buffer hindered crystal growth. All 3D crystals of NhaP1$_{His}$ were obtained using 25mM Na-Acetate, pH4.0 and 2mM DDT (and the selected detergent). So far, the concentration of these reducing agents did not have any effect on the crystal quality.

MjNhaP1 is predicted to be a thermostable protein. Taking advantage of this property the purification quality of NhaP1 was enhanced. The protein after gel filtration was heated to a temperature of 90° and ultracentrifuged at 45,000 rpm for 30 minutes. The supernatant when used for crystallization screens yielded 3D crystals under various conditions, which could be further optimized. However, western blot analysis showed aggregation after such treatment, therefore, this step was avoided.
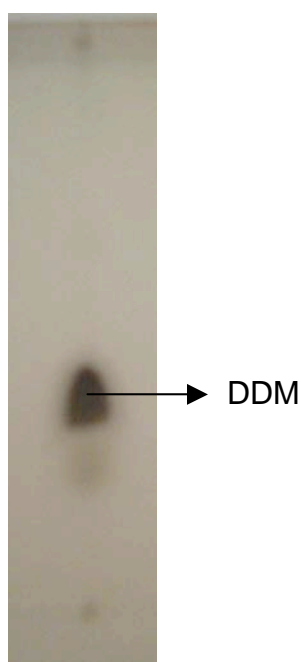
Figure 22 Analysis of lipids associated with purified NhaP1$_{His}$ by Thin layer chromatography (TLC). NhaP1$_{His}$ elution from Ni^{2+}-NTA had a characteristic brown colour. A 2-dimensional TLC with two different solvent systems did not reveal any characteristic lipids. The prominent band detected with Iodine vapour was of DDM.
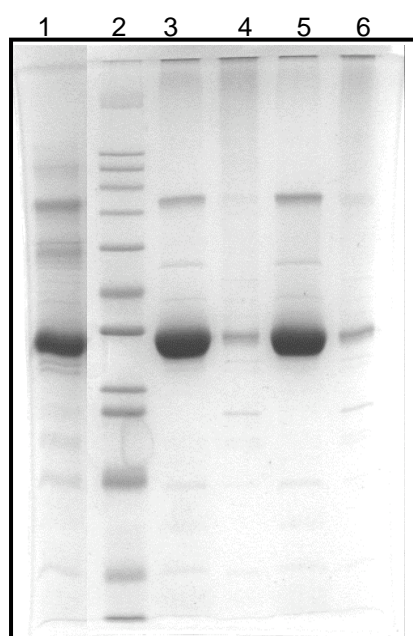
Figure 23 Purification of NhaP1$_{His}$ by heat treatment. NhaP1$_{His}$ purified by 2 steps: Ni^{2+}-NTA and Gel filtration is subjected to heat treatment to remove impurities. Lane1-NhaP1$_{His}$ after Gel Filtration column Lane 2: Molecular weight Marker Lane3: Supernatant after ultracentrifugation of NhaP1$_{His}$ heated to 90°C for 5 minutes. Lane 4: Pellet after ultracentrifugation of NhaP1$_{His}$ heated to 90°C for 5 minutes. Lane 5. Supernatant after ultracentrifugation of NhaP1$_{His}$ heated to 90°C for 10 minutes. Lane 6: Pellet after ultracentrifugation of NhaP1$_{His}$ heated to 90°C

3.4.2 Screening for 3D crystallization conditions

In all crystallization screenings, the vapour diffusion sitting drop technique was followed. Showers of 3D crystal formation were observed at a temperature of 18°C within 2 days with a 1:1 ratio of the protein sample and the reservoir drop.

Formation of 3D crystals was sensitive to the pH of the final sample (protein) buffer. A batch of purified NhaP1$_{His}$ in 25mM Tris-HCl at pH 8.0 (imidazole elution) was dialyzed to (A) 25mM Na-Actetate pH 4.0 and (B) 25mM Tris-HCl pH 8.0. Each buffer contained 0.05%DDM and 2mM β-Mercaptoethanol. Crystallization screens with

Hampton I and II and Jena Bioscience 1-4 came up with several crystal conditions for (A) but no crystals were observed in any of the conditions for (B).

The conditions at which NhaP1$_{His}$ formed 3D crystals using Hampton I and II and Jena Bioscience 1-4 are as follows:

1. 0.1M Imidazole-HCl pH 8.0, 30% w/v MPD &10%w/v PEG-4000

2. 0.1M Tris-HCl pH8.5, 0.2M CaCl$_2$

3. 5% glycerol, 15% w/v PEG-6000

4. 0.1M HEPES Na-Salt pH7.5, 70% w/v 2-propanol 10%w/v PEG 4000

5. 0.1 M MES Na-Salt pH6.5, 0.01M ZnSO$_4$, 25% w/v PEG-550 MME

6. 0.1 M MES-Na-salt pH 6.5, 0.1M Na-Acetate, 30% w/v PEG-400

7. 0.1M Acetate, pH 4.6, 0.1 M CaCl$_2$, 30% w/v PEG-400

8. 0.1 MES Na-Salt pH 6.5, 0.1MgCl$_{2,}$, 30% w/v PEG-400

9. 15% w/v PEG-1500

Due to limited protein quantity only few of the above conditions could be further optimized. The results from the conditions used for further optimization are discussed.

3.4.3   Optimization by hanging drop method

In all crystallization optimization the vapour diffusion hanging drop technique was followed. 0.5 ml reservoir solution was mixed in each well of 24 well VDXm Plate Greased^{TM} (Hampton Research) with the same volume of purified protein. Like the screening process, optimization was also carried out at 18°C. A change from sitting drop technique (screening) to hanging drop technique (optimization) was not critical for reproducing crystallization conditions. The effects of various components in the crystallization set-ups are summarized below.

Effect of MPD and PEG concentration

The condition where the mother liquor contained 0.1M Imidazole-HCl pH 8.0, 30% w/v MPD and10%w/v PEG-4000 (condition 1 from 3.11.2) was optimized using matrices, primarily, of PEG and MPD concentration. The concentration range of the

two precipitants was defined by increasing the PEG-4000 concentration in the reservoir in steps of 5% (5%, 10%, 15% and 20%) and by increasing MPD by 5% (20%, 25%, 30%, 35%, 40%, 45%). After another round of optimization the final concentration of PEG-4000 and MPD selected for the additive screen was fixed at 6% and 26% respectively. It was revealed that an increasing concentration of MPD in steps of 2% (26%, 28%, 30% &32%) lead to a decrease in crystal size.

Optimization using matrices of PEG-1500 (condition 9 from 3.11.2) in steps of 3% (9%, 12%, 15%, 18%, 21% and 24%) showed that the optimum crystal size was obtained for 21% PEG. Therefore, additive screening for 21% PEG-1500 was carried out.

Effect of additives

Further optimization with an additive screen from Hampton helped in the increasing the size of the crystals. Amongst the tested additives Trimethylamine-HCl, Iso propanol, Taurine, Urea, Cystine showed a noticeable improvement in crystal size. Trimethylamine- HCl was found to be the best additive for 3D crystals of NhaP1$_{His}$. This had a positive effect in the optimization of 3D crystals obtained from different batches of purified protein crystallized under several conditions.

Effect of CaCl$_2$ and MgCl$_2$

The effect of divalent metal ions like Mg^2+ and Ca^{2+} (condition 7&8, 3.11.2) were studied on the growth of 3D crystals of NhaP1$_{His}$. An increasing concentration of CaCl$_2$ and MgCl$_2$ in steps of 25mM (25mM, 50mM, 75mM, 100mM,125mM) showed an optimum condition of 50mM-60mM in presence of 37% PEG 400.
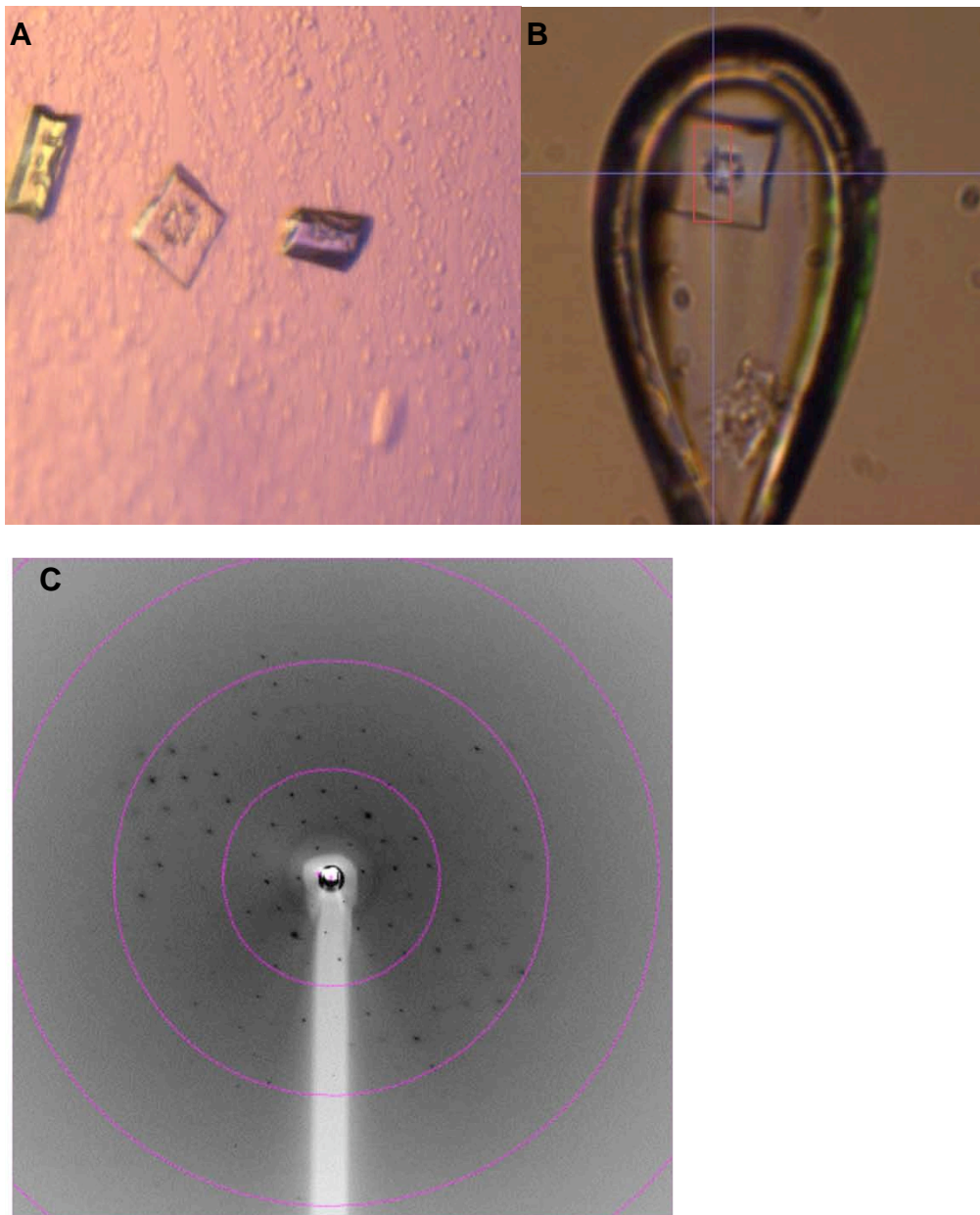
Figure 24 3D crystals of NhaP1$_{His}$ obtained by Trimethyl-HCl as an additive for optimization. (A) Single square or rectangular plate-like crystals (B) Such a crystal mounted on a cryo-loop (C) Diffraction pattern of one such crystal with circles denoting 17, 9 & 6Å resolution, respectively.
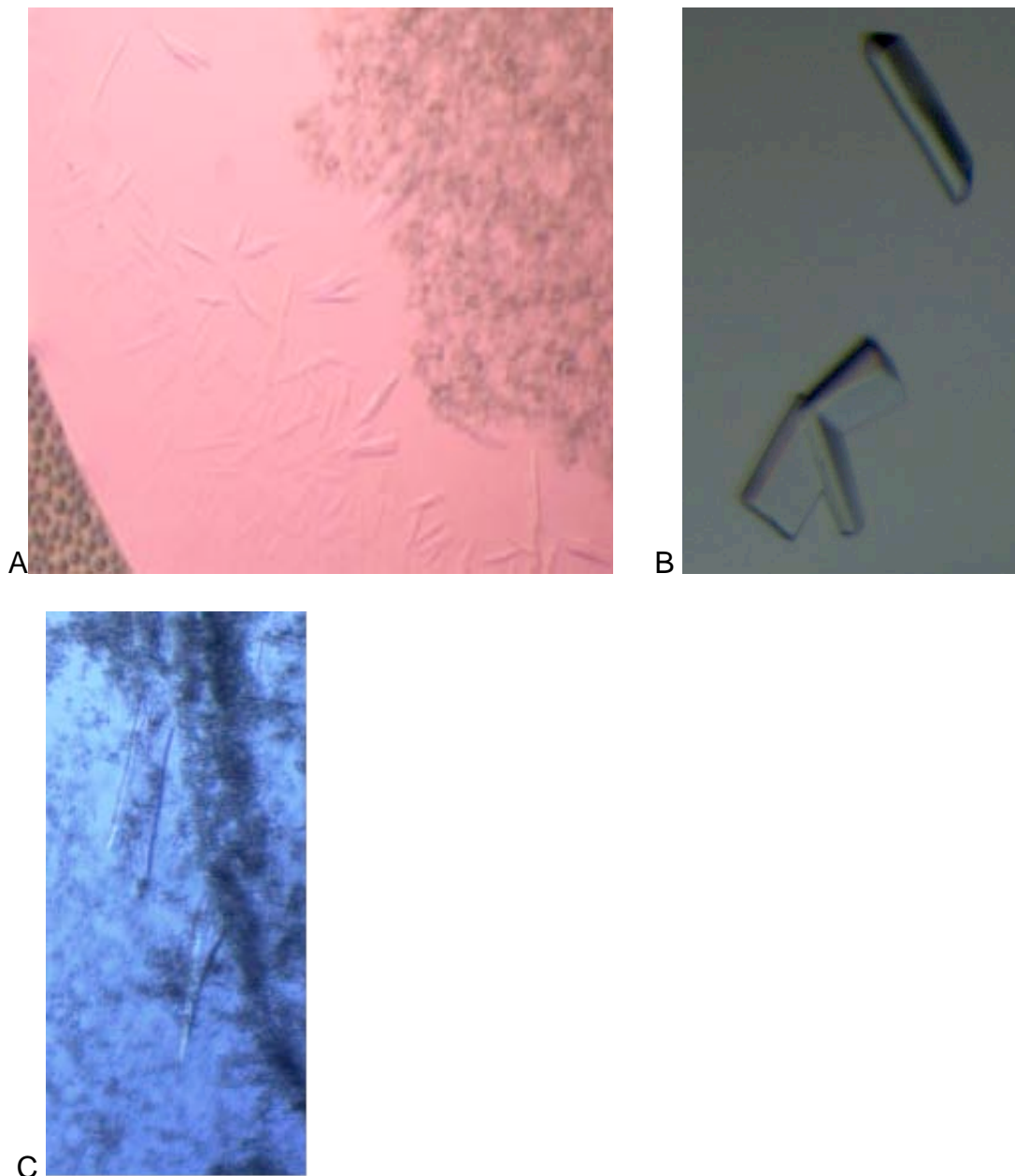
Figure 25 3D crystals of NhaP1$_{His}$ optimized by additives. (A) Iso-propanol. This additive resulted in larger number but smaller crystals. The drop showed precipitation, which did not take place at the site of crystal formation. (B)Amincaproic acid. In the optimized drops single crystals were observed with little precipitation. (C) Taurine. Heavy precipitation covered the thin, plate-like crystals.

__Effect of NaCl and LiCl__

NhaP1 functions as an exchanger of Na$^+$ or Li$^+$ against H$^+$ (Hellmer et al., 2002). The effect of NaCl and LiCl on 3D crystal formation of NhaP1$_{His}$ would surely be an interesting study. A previously optimized condition of 26% MPD and 6% PEG-4000 with a 0.1M Imidazole, pH 8.0 was selected for this study. It was observed that crystallization drops under same conditions failed to yield 3D crystals in the presence

of 2mM, 4mM, 6mM and 8mM NaCl. Several crystallization screens were also performed with commercial screens in presence of NaCl and LiCl, which never showed crystal formation.
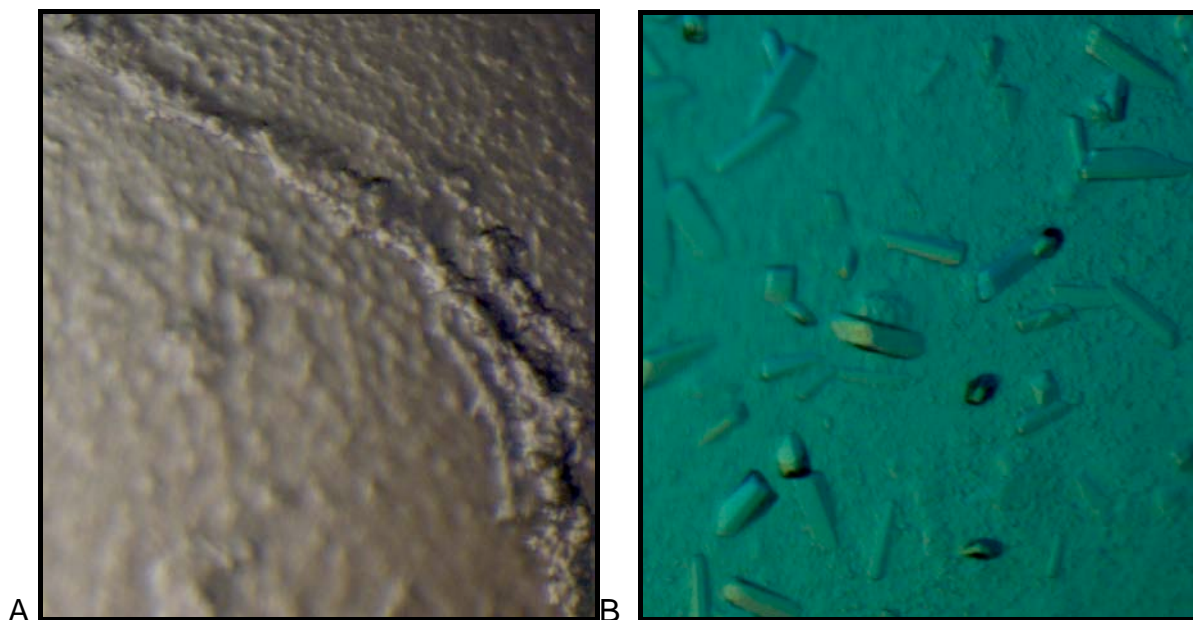
Figure 26 3D crystal formation of NhaP1His in presence or absence of NaCl. Two crystallization drops set up under same conditions (A) In presence of NaCl (B) In absence of NaCl

3.4.4 Freezing conditions of NhaP1$_{His}$ for data collection

NhaP1$_{His}$ 3D crystals were usually plate like and thus thin in the third dimension. A skin of protein precipitate from the crystallization drop adhered to the crystal. The thin size and the attached skin made it difficult to fish out the crystal from the drop. Surprisingly the crystals were robust and did not break easily. The crystals could be fished directly from the drop. Crystals were frozen by soaking them in a drop of mother liquor. The diffraction pattern of the crystals did not show any prominent ice ring.

The crystals diffracted to a resolution around 8Å. The spots were sharp but could not be indexed for getting information about the cell parameters.

3.5   2D crystallization

3.5.1   NhaP1$_{His}$

To produce high quality 2D crystals, the protein of interest must be purified to homogeneity. Initially 2D crystals of NhaP1$_{His}$ were produced using protein purified by Ni^{2+}-NTA affinity chromatography followed by size exclusion (gel filtration) chromatography. During later stage of the project the size exclusion chromatography step was omitted and the protein that eluted from the Ni^{2+}-NTA affinity chromatography was used for 2D crystallization directly. The prime reason for omitting the second purification step is to avoid loss of protein yield. It was observed that the quality of diffraction from the 2D crystals of NhaP1$_{His}$ was the same in both cases. However, the stability of the 2D crystals of NhaP1$_{His}$ was affected by the change in purification methods. Crystals formed by protein purified by Ni^{2+}-NTA affinity chromatography alone were stable for only 2-3 weeks whereas crystals formed by protein purified by both Ni^{2+}-NTA affinity and size exclusion chromatography were stable for 1.5-2 months. However, the quality of diffraction pattern of 2D crystals in both cases showed no differences. The concentration of NhaP1$_{his}$ in the elution fractions from either the Ni^{2+}-NTA affinity column or the gel filtration column were in the range from 0.3-0.5mg/ml. 2D crystallization trials were performed using protein concentrated between 2mg/ml to 10mg/ml. It was observed that the protein concentration had no effect on the size or quality of the 2D crystals.

The 2D crystals of NhaP1$_{His}$ obtained prior to this work were narrow and had a width of 0.3µm-0.4µm (Vinothkumar et al., 2005). These crystals were less suitable for data collection at higher tilt angle as the specimen surface exposed to the electron beam is very narrow. To generate wider, well-ordered 2D crystals various parameters were investigated. These are discussed below.

Detergent: The nature of detergent during purification trials as well as in the crystallization set up, can influence the quality of 2D crystals (Hasler, 1998). NhaP1$_{His}$ in 25mM Na-acetate, pH 4.0 (2D dilution buffer), containing different detergents like 0.05%DM, 1.5%OG, 0.6% Cymal-6 was used in the 2D crystallization trails. The 2D crystals of NhaP1$_{His}$ in 2D dilution buffer containing 0.05% DM buffer were of the same size and quality as earlier. 2D crystallization set-ups with NhaP1$_{His}$ in 0.6% Cymal-6 buffer showed aggregations as observed by electron microscopy.

The protein in 2D dilution buffer containing 1.5 % OG gave wide, 0.8µm-1µm, 2D crystals. These crystals were optimum for data collection. Most crystals were tubular but some crystals formed sheet-like structures. Data collection was carried out mainly on the tubular crystals.

The type of detergent used to solubilise the lipids used for reconstitution and the combination of detergent was a critical parameter in the generation of 2D crystals. A combination of 1% DDM used for lipid solubilzation, and 1.5% OG in the buffer of the purified protein produced the best 2D crystals.

Lipids: The host organism of MjNhaP1, *M. jannaschii*, has ether lipids in its cell membrane. Extraction of lipids from cells of *M. jannaschii* was carried out to reconstitute NhaP1$_{His}$ into a native lipid environment. These lipids were solubilized in 1.5%OG and 1%DDM. The crystal set ups with *M. jannaschii* lipids solubilized in 1.5% OG showed mostly aggregates in a negatively stained grid while the crystal set up with 1% DDM solubilized *M. jannaschii* lipids showed small tubes of 0.2µm-0.3µm in width and ~0.5µm in length. Crystallization trials were also made with different ratios of *E. coli* polar lipids and phosphotidylethanolamine. These trials produced very few crystalline tubes and had many small crystalline vesicles, which diffracted weakly and were not suitable for data collection.

Temperature: 2D crystallisation trials were carried out at various temperatures between 4°C and 37°C degrees. 2D crystal formation occurred between 30°C and 37°C. No crystals were observed below 30°C.

Salt in dialysis buffer: The method for 2D crystallisation of NhaP1$_{His}$ published by Vinothkumar et al. uses 200mM NaCl in the dialysis buffer. To determine the importance of salt on crystallisation, crystal trials containing 50mM, 200mM, or 300mM NaCl in the crystallisation buffer were investigated. Crystallization trials carried out in NaCl concentration lower than 50mM or in complete absence of NaCl were not successful. The well ordered, 0.8µm-1µm wide tubes obtained from crystal set ups with OG purified protein and DM solubilized *E.coli* polar extract was used for testing the affect of salt variation. The lower salt concentration of 50mM increased the width of the tubes to 1µm-1.5µm, which were also well ordered. This condition also contained a higher proportion of tubes than conditions containing high salt. The concentration of crystals on cryo-grids was similar to that observed on negatively stained grids.
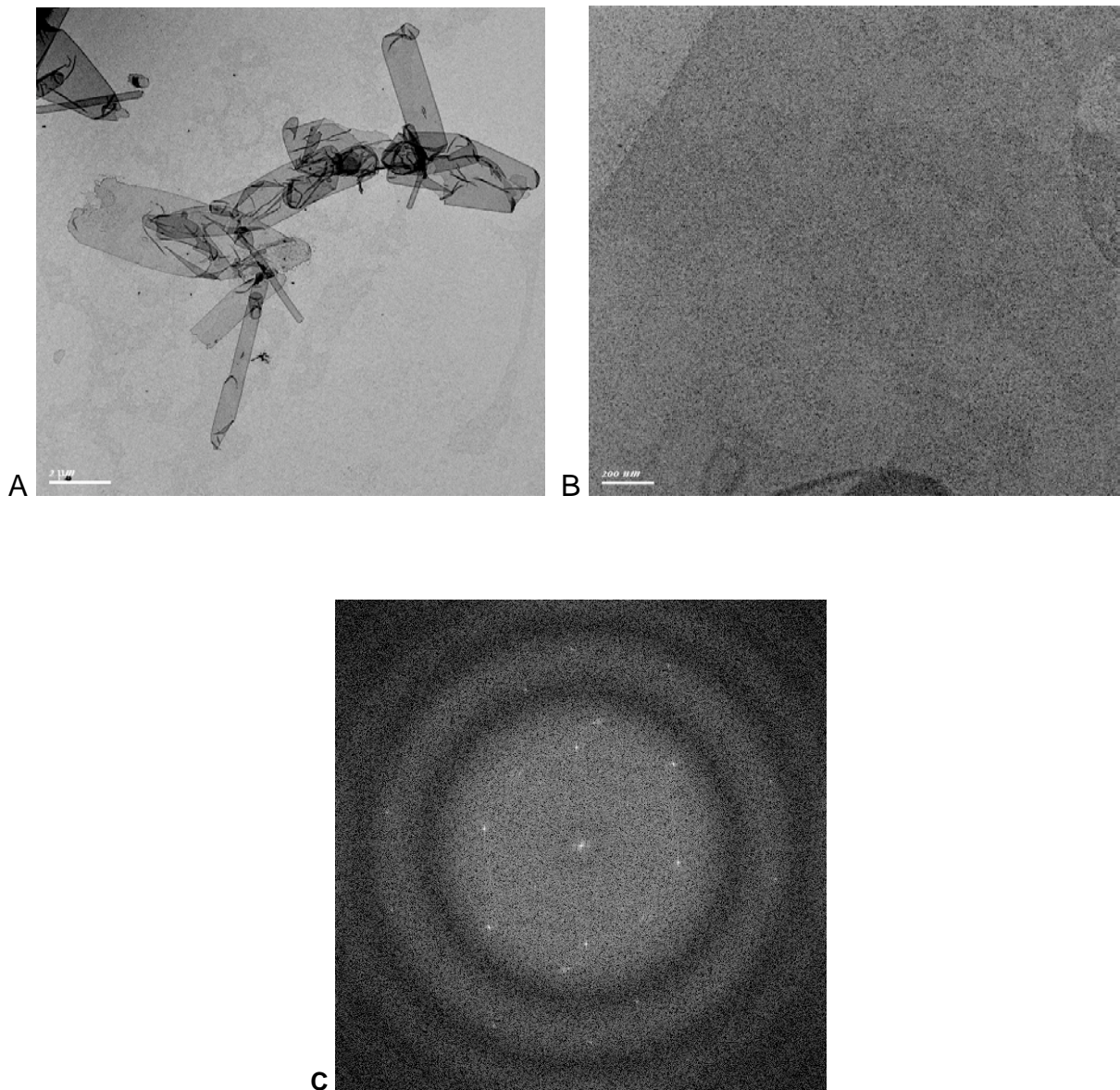
Figure 27 2D crystals of NhaP1$_{His}$ purified in OG. Images of 2D crystals stained with 1% Uranyl acetate. The images were recorded with a CCD camera at a nominal magnification of 2700. Scale bar 2 µm (B) Well-ordered negatively stained crystalline area of a tube of width 1.5 µm taken on Tecnai Spirit at a magnification of 45,000. Scale bar 200nm(C) A Fourier-transformed image of (B) recorded on a CCD camera.

Dialysis device: 2D crystallization trials were carried out in dialysis tubes with a molecular cut-off of 12-14 KDa. A flat diameter of 10mm was found to be suitable for a minimum volume of 100µl. The maximum volume used for crystal set ups of MjNhaP1 is 200µl. Often the problem of leakage was encountered which hampered the reproducibility and interpretation of screening parameters. Keeping the size of tubing to 6cm-8cm and placing the clips strategically at a distance of 5-10mm from the ends avoided leakage and helped to maximise volume recovery (Schmidt-Krey, 2007) and maintain reproducibility.

3.5.2 Mutant R347A

The NhaP1 mutant R347A could be purified homogeneously by Ni^{2+}-NTA chromatography. The amino acid residue R347 in MjNhaP1 is highly conserved and has been found to be functionally critical as the mutant R347A exhibits low antiporter activity at pH 6.0 (Hellmer et al., 2003). This mutant was selected for 2D crystallization for two reasons (a) A projection map can be calculated from the 2D crystals of R347A. This projection map can be compared with the projection map of the wild type, which might help in understanding of the helix packing of MjNhaP1 related to antiporter activity. (b) This antiporter is less active compared to the wild type. Due to this, it is expected that the helical domains are more stable which might improve overall crystal packing. Preparations of R347A from the Ni^{2+}-NTA column were concentrated to ~ 8mg/ml and used immediately for 2D crystallization without any buffer exchange or dialysis. Three different lipid protein ratios (LPR), 0.2, 0.4 and 0.6 were screened using *E.coli* polar lipids. Tubular crystal formation was observed at all three LPRs but the size and quality of the crystal differed in each. The set up with an LPR of 0.2 showed mostly aggregates with very few, small tubular crystals. In the set up with an LPR of 0.4, tubular crystals were observed which were ~8-12µm in length and 0.4µm in width. This condition produced the best diffracting crystals. The setup containing an LPR of 0.6 also produced long tubular crystals. These crystals had a similar length to those observed in the setup containing an LPR of 0.4 but were less frequent.
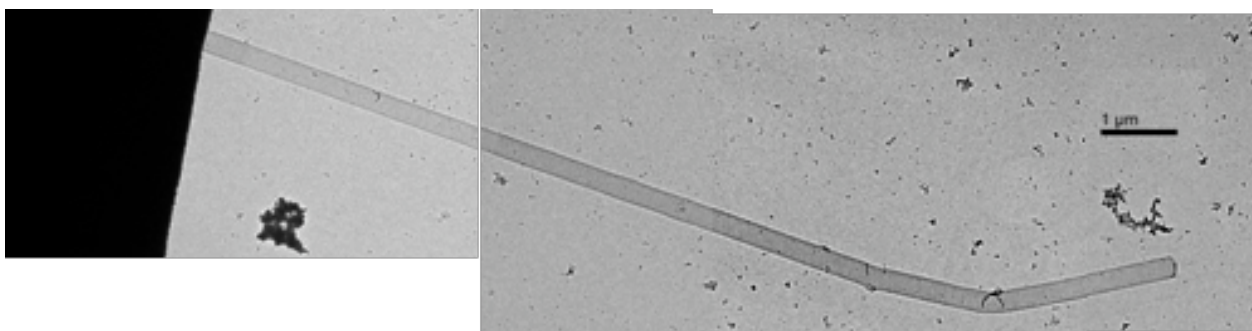

Figure 28 A 2D crystal of R347A. The crystals were negatively stained with 1 % uranyl acetate. The scale bar represents 1 µm. Tubes are formed in the presence *E. coli* lipid extract. The length of the tubes varied between 8-12µm.

3.5.3 Projection map of mutant R347A

The mutant R347A that shows low activity (Hellmer et al, 2003) could be crystallized in 2D. The crystals could be easily frozen in cryo-conditions similar to the wild type crystals.

Optical diffraction of images of 2D crystals of the mutant R347A showed very sharp spots to a resolution better than 8Å. 8 images from a single cryo-grid were selected for calculating a projection map.
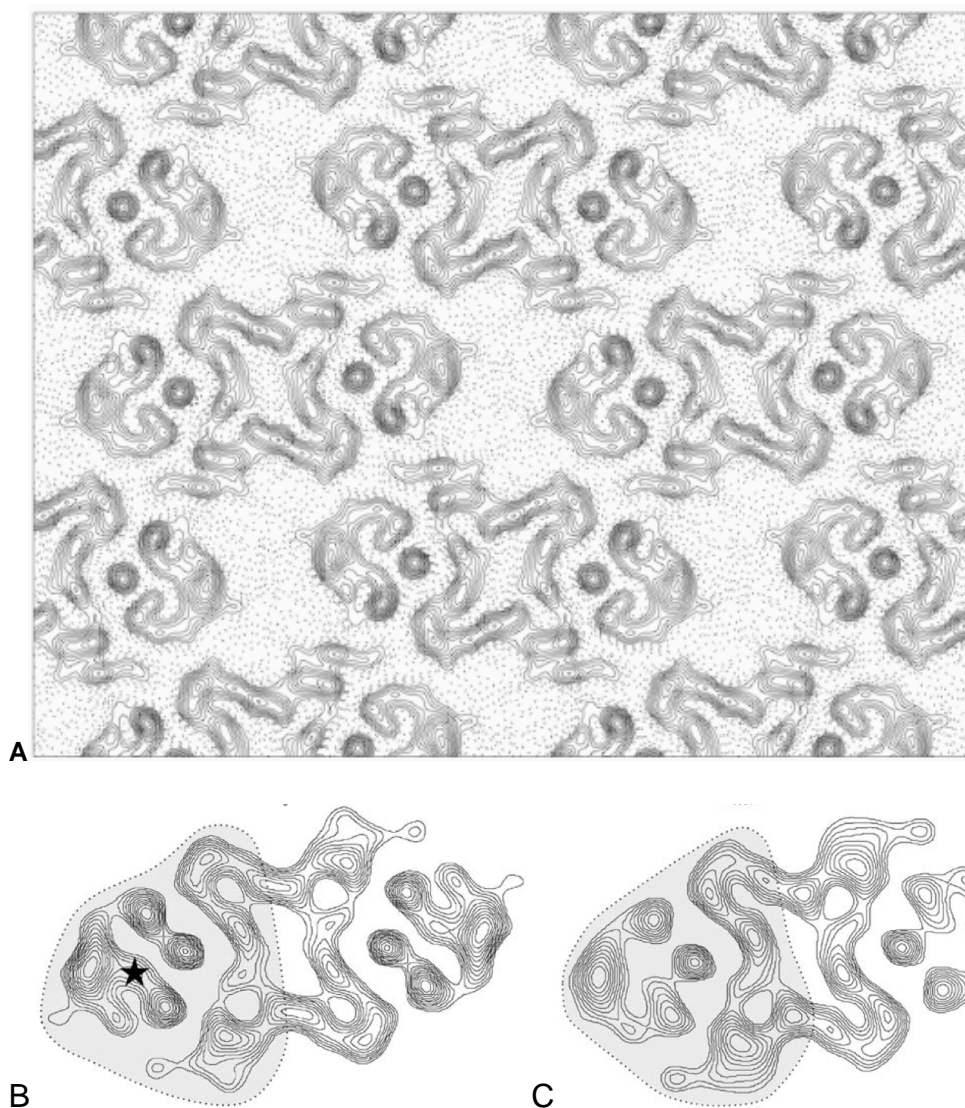

Figure 29 (A) Projection map of R347A at 6Å resolution. (B) Projection map of MjNhaP1 at pH 4.0 (Vinothkumar et al., 2005) (C) projection map MjNhaP1 at pH 8.0 (Vinothkumar et al., 2005).

The unit cell dimensions were found to be a = 81Å, b = 103Å, γ= 90° for the crystal lattices which is nearly same like the wild type 2D crystals. After 2 or 3 rounds of unbending using the program, CCUNBENDK the Fourier transformed images showed reflections to a resolution better than 6Å. The projection map showed that

84

the mutant like the wild type MjNhaP1 formed a dimer. The unit cell contains four molecules of MjNhaP1 arranged in 2 dimers with a 2-fold axis perpendicular to the membrane. The crystals like wild type MjNhaP1 showed $p22_12_1$ symmetry by phase comparison of symmetry related reflections.

In order to have a clear idea of the differences in helix packing between wild type MjNhaP1 and the mutant R347A, a difference map has been calculated.
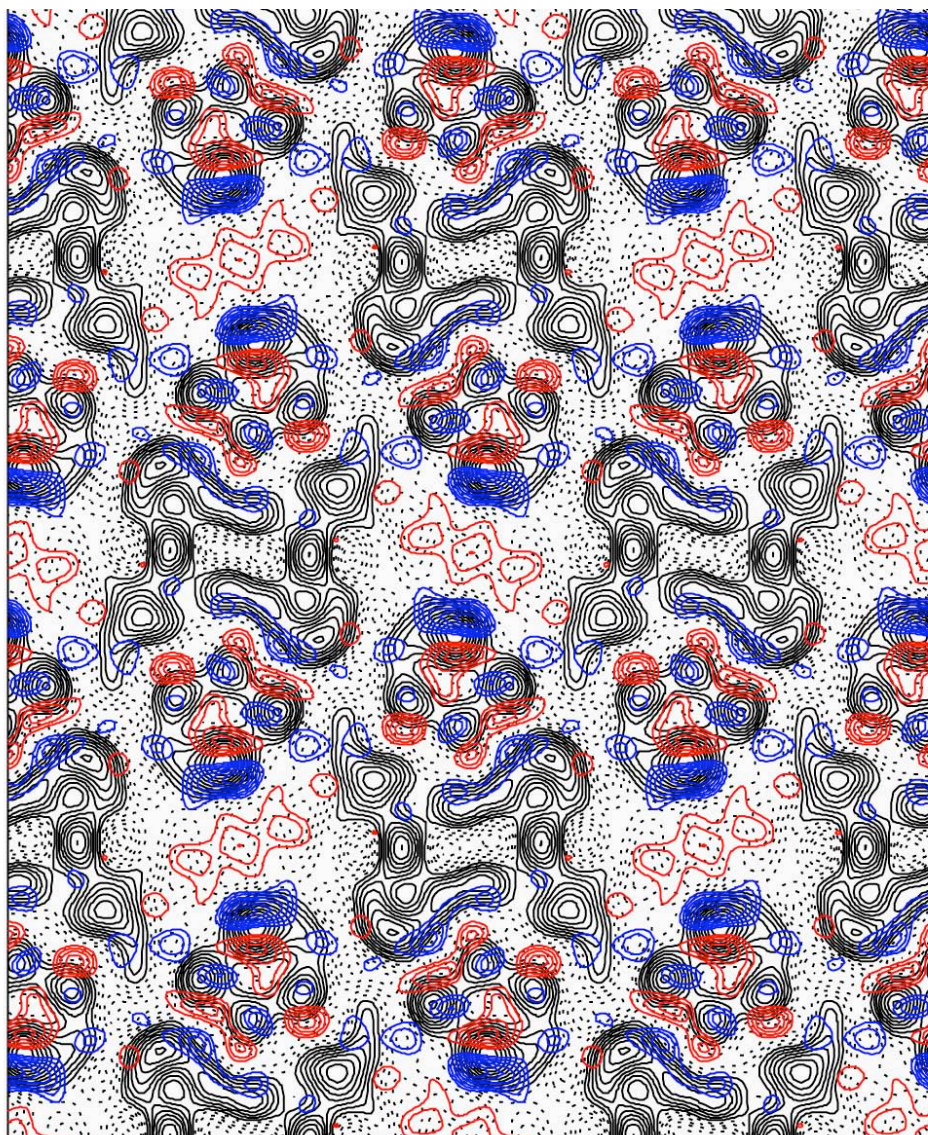
Figure 30 Difference map of wild type NhaP1 and mutant R347A projections. The differences between 1 to 4 σ are plotted with each contour representing 0.5σ. Positive densities are blue and negative are red. Overlay of the difference map with the wild type NhaP1 projection map (black).

The difference map shows clear differences in the outer helix bundle as indicated by blue lines. There are no visible differences in the position of helices in the dimer interface between both proteins. MjNhaP1 has been shown to have highest activity at pH 6.0-6.5 and inactive above 7.0. There is no information available so far about its

85

functional state or activity pattern at pH 4.0. Compared to the wild type the mutant has almost no activity at pH 6.0-6.5. Both the 2D crystals have been prepared and studied at pH 4.0. Our difference map suggests clearly that the helices in the outer bundle are in a different conformation at these two states of the antiporter. Since we know that the mutant R347A is inactive, the wild type crystal at pH 4.0 represents the transporter in an intermediate state (between inactive and active state).

3.6   3D reconstruction of NhaP1

3.6.1   Data Collection

Untilted specimen: Images of the frozen hydrated tubular crystals embedded in 4.5% trehalose were recorded in the electron microscope. A 0° fixed angle holder was used to record data in the XY plane of the specimen. On the cryo-grid the crystalline tubes were distinguishable from the surroundings. It was observed that the blotting procedure was crucial for the reproducibility of a good quality cryo-grid. The quality of data for untilted specimen was independent of the size or width of the crystal and did not vary significantly between batches. Also, both copper and molybdenum grids gave same quality images for untilted specimen. Images showing spots to 10Å in all directions, assessed by optical diffraction, were chosen for scanning and subsequent processing. The two planar lattices formed as the tubular crystals were flattened on the carbon film and could be processed separately yielding two data sets for some images. After three to four rounds of unbending these crystals showed spots to 6Å. The crystals had $p22_12_1$ symmetry as indicated by phase comparison of symmetry related reflections (Valpuesta et al., 1994). The crystals had a unit cell of a=81Å, b=108Å and γ=90°. Images with a phase residual below 20° were merged to calculate a projection map at 7Å resolution. Images with phase residual above 20° were discarded. This data set was used as the initial reference set to which tilted (20°, 30°, and 45°) data sets in increasing order were added.

Tilted specimen: In order to achieve the project goal of 3D reconstruction, data had to be collected by tilting the specimen to various tilt angles. All images of NhaP1 were collected on the JEOL 3000SSF microscope. This microscope lacks a tilting specimen stage and thus cryo holders of fixed tilt (20°, 30°, and 45°) were used to collect tilted data. Some important points, which contributed towards the collection of good quality data, are mentioned below:

1. *Morphology*: Crystalline vesicles were not ideal for tilted data collection but wide and longer tubes were optimum. Most images of tilted specimen were recorded with tubular crystals with a width greater than 0.8µm.

2. *The cryo- grid*: Selecting single, straight lying crystals with no contaminating particles sticking to the surface contributed to good quality images. Statistics revealed that tubes sticking out from the edge of the grid bar gave better quality data.

5. *Crystal Batches*: Images recorded with fresh batches of 2D crystals gave a higher number of good quality images. Crystals prepared with purified protein from a single step Ni^{2+}-NTA chromatography could be stored at 4°C for 2-3 weeks after which they deteriorated. However, crystals prepared with protein purified with an additional gel filtration chromatography could be stored for 1.5-2 months and yielded good quality images.

6. *Anisotropy:* Data collected from tilted specimens often shows a loss of information in the direction perpendicular to the tilt axis. This loss of resolution is often caused by imaging non-flat specimens (Henderson et al., 1990). One cause of lack of specimen flatness is due to bending or unevenness of carbon film, which is used to support the 2D crystals on a metal grid (Vonck, 2000). Isotropic data was obtained for tilted 2D crystals of $NhaP1_{His}$ using carbon film of 100Å thickness. The newly introduced TiSi films, a highly conductive alloy of titanium and silicon, (Rhinow and Kuhlbrandt, 2008) was also used as a support film for data collection of specimen tilted at 45°. However, the quality of data obtained with TiSi was equal to those obtained using carbon films. Also the frequency of good quality images were fewer compared to those obtained with carbon as the support film. Data collection of $NhaP1_{His}$ 2D crystals with TiSi films looks promising but needs optimization.

It is believed that carbon film on copper grids is prone to cryo-crinkling because of the difference in thermal expansion coefficient of carbon and copper. To avoid cryo-crinkling molybdenum grids are preferred as molybdenum has a expansion coefficient value closer to that of carbon (Booy and Pawley, 1993). This was not the case for NhaP1 crystals as best quality data for tilted specimens were obtained with copper grids.

 7. *Microscope parameters:* The spot scan method of imaging 2D crystals involves focussing the electron beam to a small spot, which is moved over the specimen to record images. Spotscan is believed to reduce specimen motion which is often induced by a flood beam as a result of specimen charging (Downing, 1991). The best

images of NhaP1 2D crystals, which showed good diffraction data, were collected by this method.

3.6.2   Image processing

Images of crystals were taken at magnification of 70,000x with the specimen grid tilted between 0 and +45° within the microscope. A single image was taken per crystal tube. Micrographs of crystals that diffracted to at least 3 orders and lacked excessive astigmatism and drift were chosen for digitization. Images of the flattened tubes showed two easily distinguishable crystalline lattices rotated by 12°-15° which originate from the two sides of the flattened tube, Images were processed using the MRC suite of programmes. These programmes reduced lateral lattice distortion in the crystal, and increased the signal to noise ratio by the process of lattice unbending and quasioptical filtering (Crowther, 1996). In most cases, both lattices observed from the images of flattened tubes could be processed separately and used for the 3D reconstruction. The lattices possessed $p22_12_1$ symmetry with unit cell dimensions a = 81°, b = 108°, γ=90°. Selected images of tilted specimen with their corresponding computed Fourier transforms generated after processing (2-3 rounds of unbending) are shown in Figure 31.
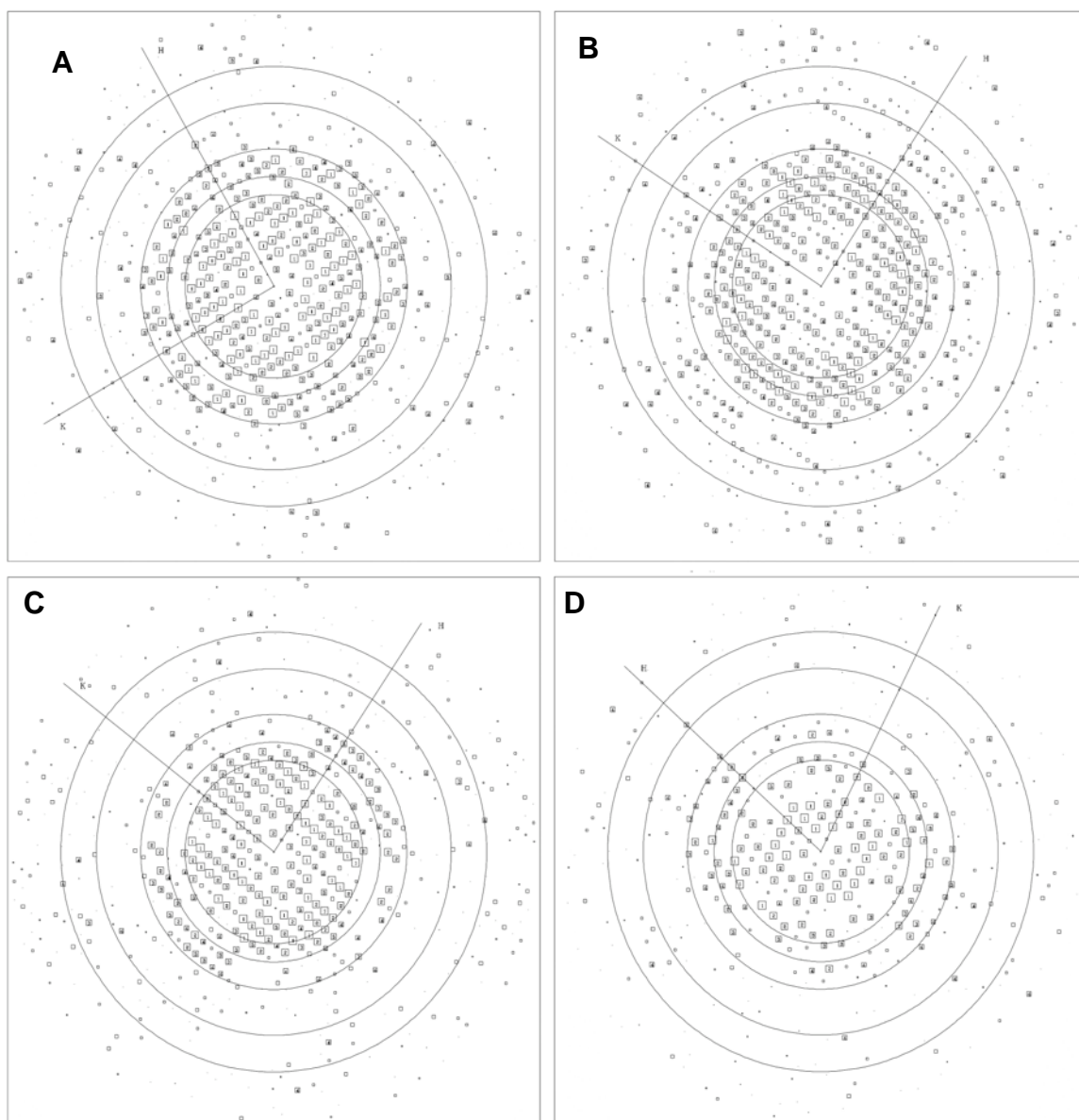
Figure 31 Fourier transforms of typical images recorded at tilt angles (A) 0°, (B) 20°, (C) 30° (D) 45⁰. Circles denote 12,10, 8, 6 and 4 Å resolutions, respectively

The merged data set was evaluated with the program LATLINEK (Agard, 1983), which generates lattice lines (Figure 26) by applying a weighted least-squares procedure to the phases and amplitudes. Due to the limited amount of points for comparison, some-out-of scale amplitudes were observed. These out-of-scale amplitudes were manually modified. Curves were fitted to the plotted data and sampled at ΔZ =(1/150) Å-1.
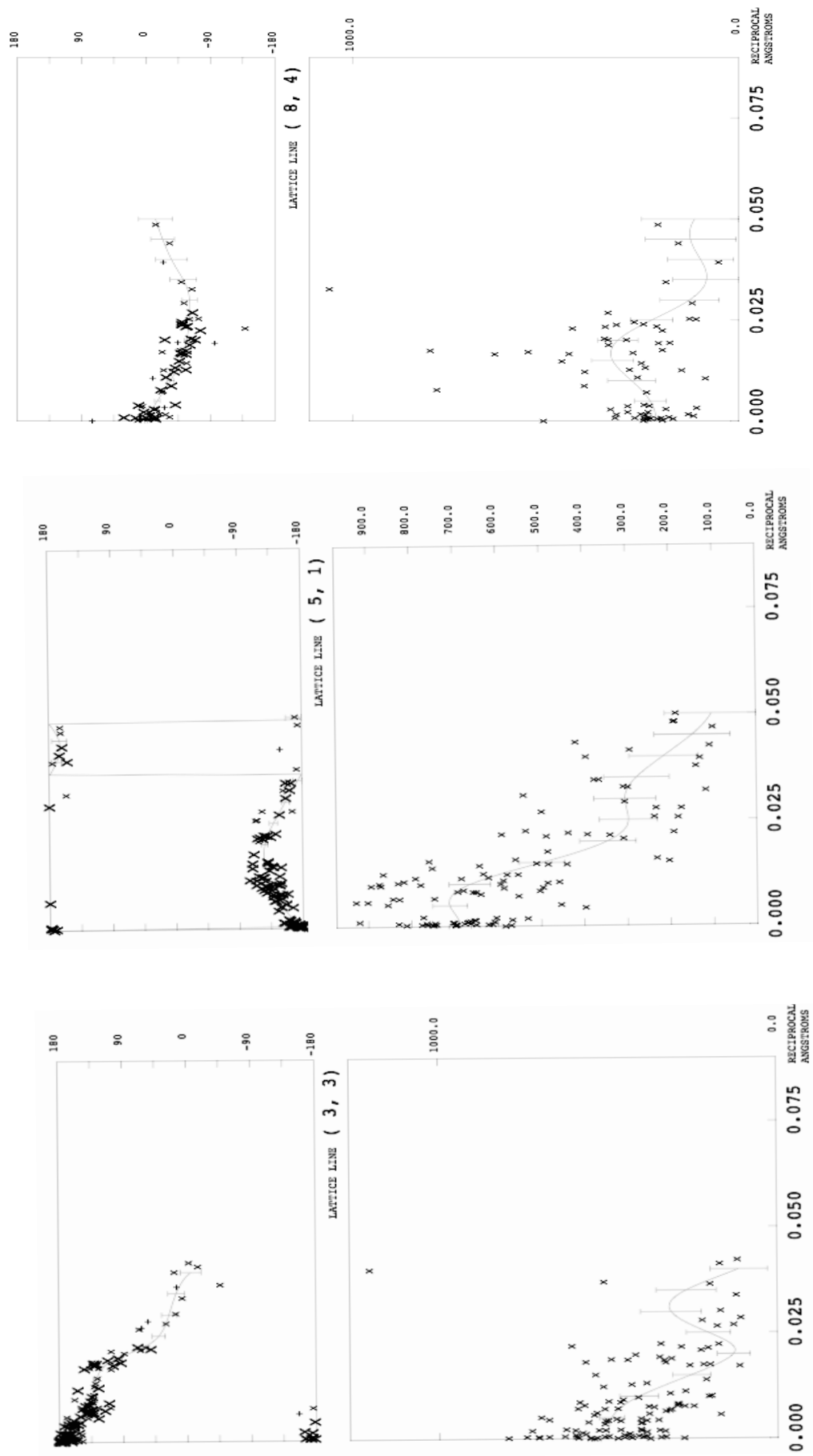
Figure 32 Plots of amplitudes (lower panels) and phases (upper panels) along the z* axis for three selected reflections. The fitted lattice lines were produced by weighted least squares fitting and the resulting errors are shown.

90

Table 2 <u>Crystallographic data summary</u>

Plane group	$p22_12_1$
Number of images*	74
Resolution in plane[a]	7Å
Resolution vertical[a]	14Å-15Å
Total no. of observations[b]	7475
No of unique observations	1494
Overall weighted R-factor (%)[b]	0.297
Overall weighted phase error[b]	17.8°

....

*Distribution of tilt angles (0°-15, 20°-14, 30°-17, 45°-28)

[a] As calculated from a point-spread function of the experimental data.

[b] From program LATLINEK.

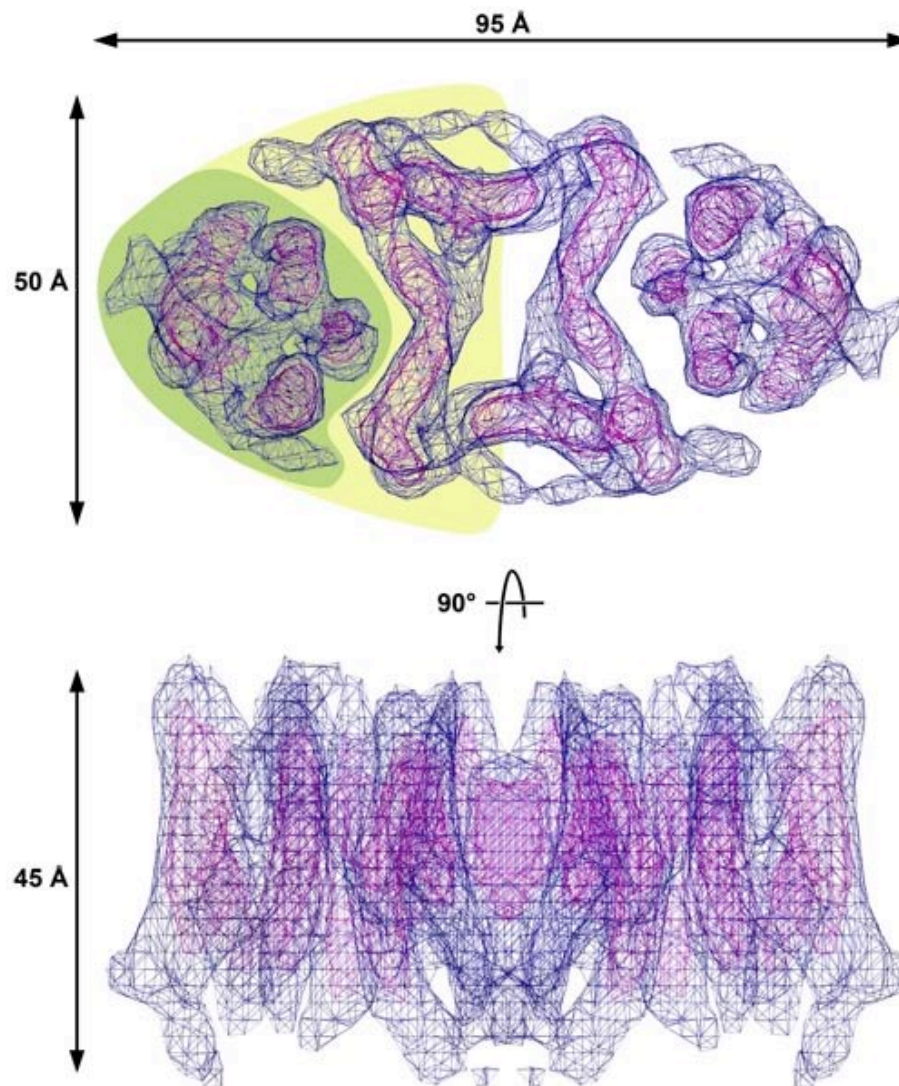## 3.7   3D map of MjNhaP1

The phases and amplitude obtained from the fit lattice lines were combined to generate a 3D map of MjNhaP1. Four different maps were calculated applying B-factors of -350 Å^2, -400 Å^{2,}, -450 Å^2 and -500 Å^2 respectively. The maps calculated with B-factors 400 Å^2 and 450 Å^2 showed fully resolved helical densities and these two maps were very similar. The map calculated with -500 Å^2 had the lowest apparent signal to noise ratio.

The projection map (Vinothkumar et al., 2005) had shown MjNhaP1 as a dimer with dimenions of ~51Å x 84Å. The 3D map of MjNhaP1 also shows a tightly packed dimer with an oval shape (Figure 33). In the 3D map, the dimensions of MjNhaP1 in the membrane plane are ~95 Å for the long and ~50 Å for the short axis. In the side-view, the MjNhaP1 has a thickness of ~45 Å. As mentioned in table 2 the in-plane resolution of the map is 7Å and the resolution in the vertical direction is 14Å. At this resolution, elongated helical densities could be clearly observed. These helical densities formed two distinct regions as shown by the delineated boundary of one monomer (Figure 33). The two distinct regions identified are:

 a) The region in the central part of the dimer composed of several tilted helices forming an interface between both monomers. Four helices in the centre could be clearly distinguished in the 3D map. Towards the periphery adjacent to the second

monomer two or three helical densities appear to be present. These two or three helices are in close contact with the second monomer.

Figure 33 3D electron density map of MjNhaP1. The map is contoured at 1σ (blue) and 2σ (purple). (A) Top view, one monomer is highlighted. The outer bundle and dimer interface are highlighted in green and yellow respectively. (B) The side view shows the NhaP1 map along the membrane plane.

b) In the other region, a group of six tightly packed helices form an outer bundle. This bundle contains three helices in the centre of the monomer and three helices on the outermost periphery. The three helices in the centre are almost perpendicular to the membrane plane, clearly separated from each other and extend from the top to bottom of the map. The densities for the other three peripheral helices are more connected to each other. They tilt at an angle of 5°-10° from the membrane normal.

There is a stretch of density in the centre connecting the three peripheral helices to three central one.

3.8   Sequence alignment

To investigate, whether the distinguishing structural features of MjNhaP1 could be a common feature of other archaeal, bacterial and eukaryotic Na$^+$/H$^+$ exchangers/antiporter (2.13), alignment of several amino acid sequences was carried out. The alignment indicated a different number of hydrophobic segments in different families. The NhaA family from *E.coli, S.enterica* and *V.aginolytiicus* contain 12 hydrophobic segments. The archaeal MjNhaP1 families show 13 hydrophobic segments. Finally, the NHE and Nhx families from eukaryotes show 14 hydrophobic segments with the exceptions of Nhx1 from *A. thaliana* and the human Nhe6a which have 13 and 15 hydrophobic segments, respectively. The alignment revealed that the amino acid sequence for the β-sheet of the X-ray structure of NhaA (Hunte et al., 2005) is present only in the two other bacterial species. This region is missing in the eukaryotic and archaeal counterparts.

The corresponding hydrophobic segments from the same family show high sequence conservation. Sequence conservation is also observed for the intermediate hydrophilic stretches of the same family especially for the prokaryotic proteins. Sequence motifs common to all families have been found in segments corresponding to transmembrane helices IV and V of the NhaA X-ray structure. Helix IV in NhaA is unwound in the sequence AIPAATDI located in the middle of the membrane (Hunte et al., 2005). A similar motif appears to exist in all other antiporters as shown in the alignment. The other unwound helix XI in NhaA disrupts a GIG motif. However, such a motif is not present in any other antiporter. Instead, a conserved GPRGVVP and GGLRG motif is present in the NhaP and NHE family respectively, with Nhx1 from *S.cerevesiae* and *A. thaliana* as exceptions. Helix V also shows high conservation in all the selected families in the alignment due to the presence of the common motif AIDDLG, FNDPLG and NDA in the NhaA, NhaP and NHE family, respectively.

Figure 34 Alignment of Na⁺/H⁺exchangers. Nomenclature as for putative helices in NhaP1. NhaA helices in Roman numerals in bracket.

The archaeal antiporters share conserved sequences with both their eukaryotic and prokaryotic counterparts. The amino acids in hydrophobic segments corresponding to helix IX of NhaA show conservation in the archaeal and eukaryotic antiporters. On the other hand, helix X of NhaA contains the motif KPLG which represented by the RPLG motif in the NhaP family.

3.8.1   Presence of an uncleaved signal peptide

The sequence alignment (Figure 34) and MjNhaP1 model (Figure 36, Figure 37) suggests that the additional helix (A) is in the N-terminal end. The amino acid sequence of the first helix aligns with N-terminal hydrophobic segments of several eukaryotic Na^+/H^+ exchangers that have been predicted to be signal peptides. Using a web based signal peptide prediction server, the sequence for this N-terminal hydrophobic segment of MjNhaP1 was analysed. Generally sequences for signal peptides typically show three distinct zones: an N-terminal region (n-region) which often contains positively charged residues, a hydrophobic region (h-region) of at least six residues and a C-terminal region (c-region) of polar uncharged residues with some conservation at the - 3 and - 1 positions relative to the cleavage site (Olof Emanuelsson1, 2007). A high score was obtained for all these three regions in the prediction, which suggests that the additional helix could be a signal peptide. The corresponding N-terminal hydrophobic segment of NHE1 from *Homo sapiens* was also analysed and here too the score indicated that this might also be a signal peptide.
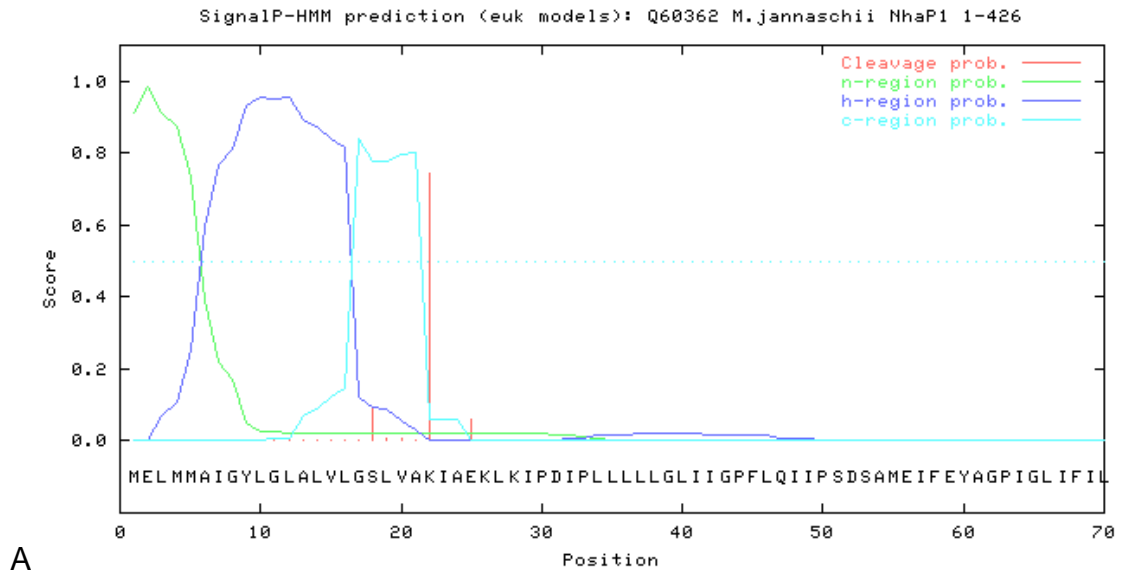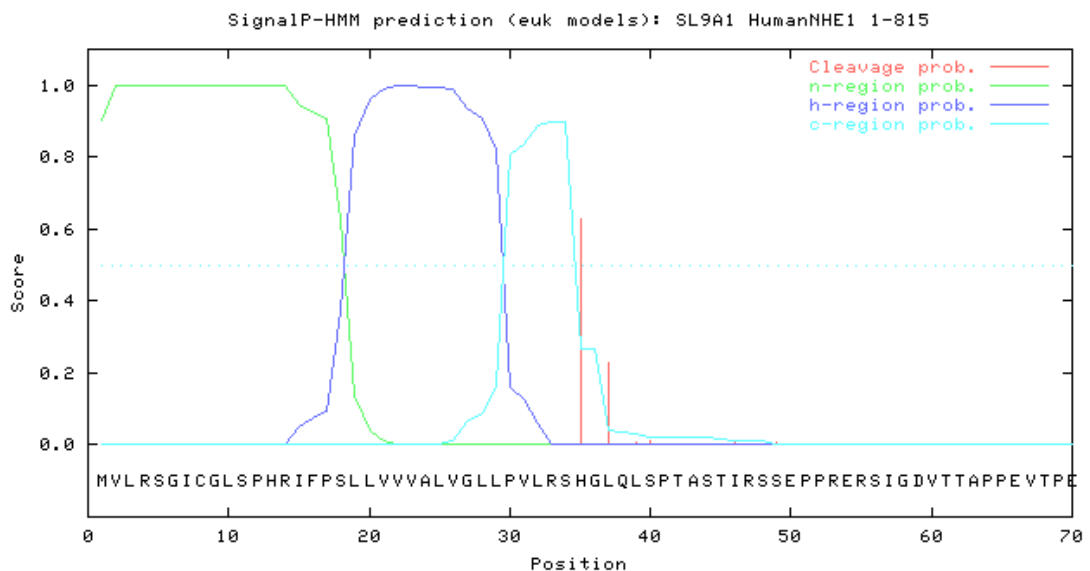
Figure 35 Prediction of signal peptide. A. Analysis of N-terminal hydrophobic segment of MjNhaP1 (B) Analysis of N-terminal hydrophobic segment of NHE1. The figure shows score for sequences present in signal peptides. Typically, such sequences show three distinct zones: an N-terminal region (n-region, in green) which often contains positively charged residues, a hydrophobic region (h-region, in blue) of at least six residues and a C-terminal region (c-region, in cyan) of polar uncharged residues with some conservation at the - 3 and - 1 positions relative to the cleavage site. The method incorporates a prediction of cleavage sites (red line) and a signal peptide/non-signal peptide prediction based on a combination of several artificial neural networks and hidden Markov models.

3.8.2　3D model of MjNhaP1

Based on the 3D map of MjNhaP1 and using the X-ray structure of NhaA as a template, a model of MjNhaP1 was constructed.

The outer bundle helices III, V and XI of NhaA fitted well into the MjNhaP1 map after a slight shift but helix X required an extension and reorientation of the N-terminus in order for it to fit appropriately. The assignment of helices in this outer bundle was the same as those of the helices in the outer bundle of the X-ray structure of NhaA. Although the density for the helices IV and XI appear to be continuous, these have been interpreted as disrupted/unwound helices (IVa/b and XIa/b) as observed in the X-ray structure of NhaA. These two helices had also appeared to be continuous in the NhaA 3D map (Williams, 2000). This was due to the low vertical (z) resolution of the 3D map of NhaA, which is similar to the vertical resolution of the 3D map of MjNhaP1. Therefore, it has been assumed that the half helices appear as continuous density and the disruption is not visible.

The assignment of helices to the density in the dimer interface was more difficult. Due to the absence of a corresponding density in the 3D map of MjNhaP1, the β-hairpin of NhaA between helix II and I was omitted in the model. This omisson is further supported by the sequence alignment study, which showed that the corresponding sequence for the β-hairpin of NhaA was absent in the MjNhaP1 sequence. While the N-terminal part of helix II of NhaA could be placed at the same position in MjNhaP1, its C-terminal had to be shifted by ~10 Å to fit the map. In addition, the N-terminal part of helix IX of NhaA could be located in the same region in the 3D map of NhaP1 whereas the C-terminus had to be shifted by ~8 Å. The most drastic differences observed were in the region corresponding to helices VI, VII, and VIII of NhaA. These helices were shifted up to 15 Å in order to fit them into the MjNhaP1 map. In addition, helix VI was extended by ~10 Å and embraced the entire MjNhaP1 molecule.

After modelling the 12 NhaA helices into the MjNhaP1 map, a clear density in the proximity of helix VI, VII and VII was left, which could be interpreted as the 13th helix of MjNhaP1. By alignment of MjNhaP1 sequence with different antiporter sequences, it was evident that the additional helix is located in the N terminus of MjNhaP1 (Figure 34). To maintain consistency in helix numbering with NhaA we have called this additional helix, helix A.
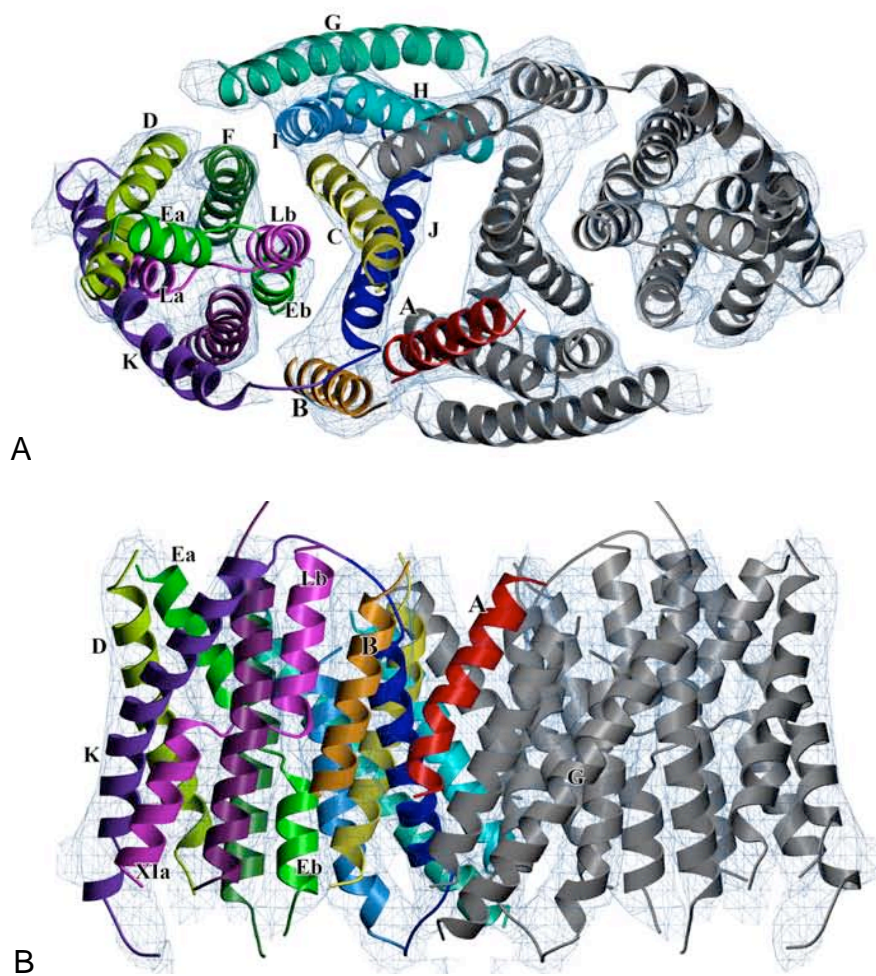
Figure 36   Model 1 of MjNhaP1 fitted in to the 3D map. The helices of one monomer are represented in colours and the other monomer is represented in grey. In this model helix 0 (red) is located in the interface region and mediated tight dimer interactions.

According to the secondary structure prediction, there is a loop of approximately 7 amino acid residues connecting helix A and B. This short distance makes it likely that the position of helix A needs to be adjacent to helix B. However, there is ambiguity in the assignment of helix A. Based on this two models for MjNhaP1 were predicted: (1) In model 1, helix A is assigned to the density in the vicinity of helix B and J (Figure 36). Here, helix A is located in the interface region and appear to mediate tight dimer interactions with H and I of the second monomer. In this model helix G was assigned to the density in the periphery of the molecule (2) In model 2, Helix A is assigned to the density in the outermost periphery of the second monomer (Figure 37). At this position, helix A extends obliquely from one monomer to the other.
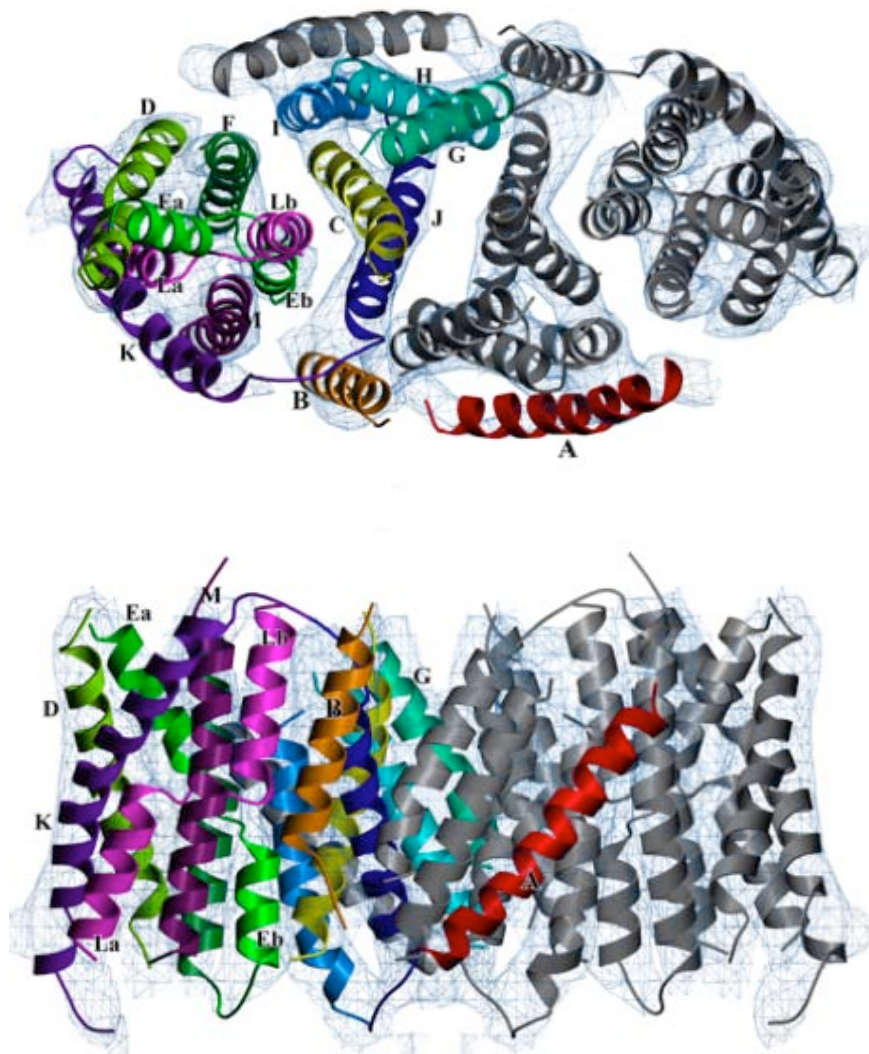
Figure 37   Model 2 of MjNhaP1 fitted in to the 3D map. The helices of one monomer is represented in colours and the other monomer is represented in grey. In this model helix 0 (red) is located in the periphery of the second monomer.

3.8.3   Helix Packing of MjNhaP1

Horizontal slabs (5Å) thick at different depths (7.5Å) of the outer bundle of helices of model 1 demonstrate that the helices move away from one another at the top and bottom surface of the map and form a more compact clustering towards the centre.

The lengths of individual helices vary between 20Å and 36Å. The 6 helices in the outer bundle were observed in all sections at different heights through the map, which indicate that they span the membrane from top to bottom.

The dimer interface shows 7 helical densities with lengths between 24Å and 35Å. The helices are tilted with average tilt angles in the range of 15°-30° from the

direction perpendicular to the membrane. The helices A, G and H appear to take part in the dimer packing.
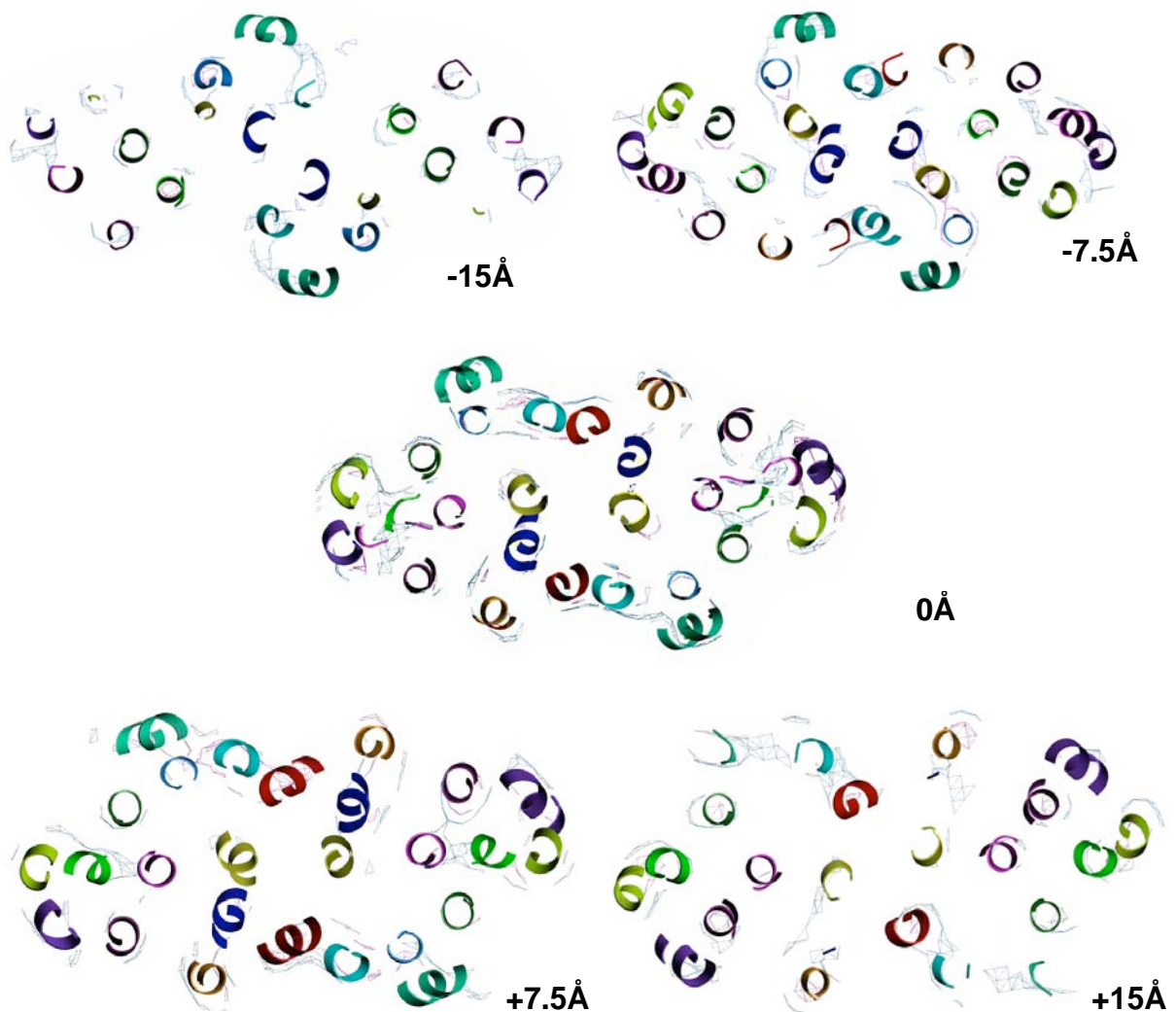

Figure 38 Horizontal slices (5A thick) from the density map at intervals of 7.5Å from the centre.

3.9 Comparison of MjNhaP1 with NhaA

The overall dimensions of the MjNhaP1 dimer is comparable to that of the NhaA dimer (Williams, 2000) but MjNhaP1 is 5 -10 Å longer in the membrane plane. The projection maps had earlier suggested that there are considerable differences in the orientation of the transmembrane helices (Vinothkumar et al; 2005). The 3D map of MjNhaP1 reveals that significant differences does exist between the 3D architecture of NhaA and MjNhaP1. In NhaA, the monomers are well separated by a gap in the

dimer interface within the membrane (Williams, 2000). Whereas, both monomers of MjNhaP1 interact more tightly, leaving only a small gap in the centre of the dimer (Figure 39).
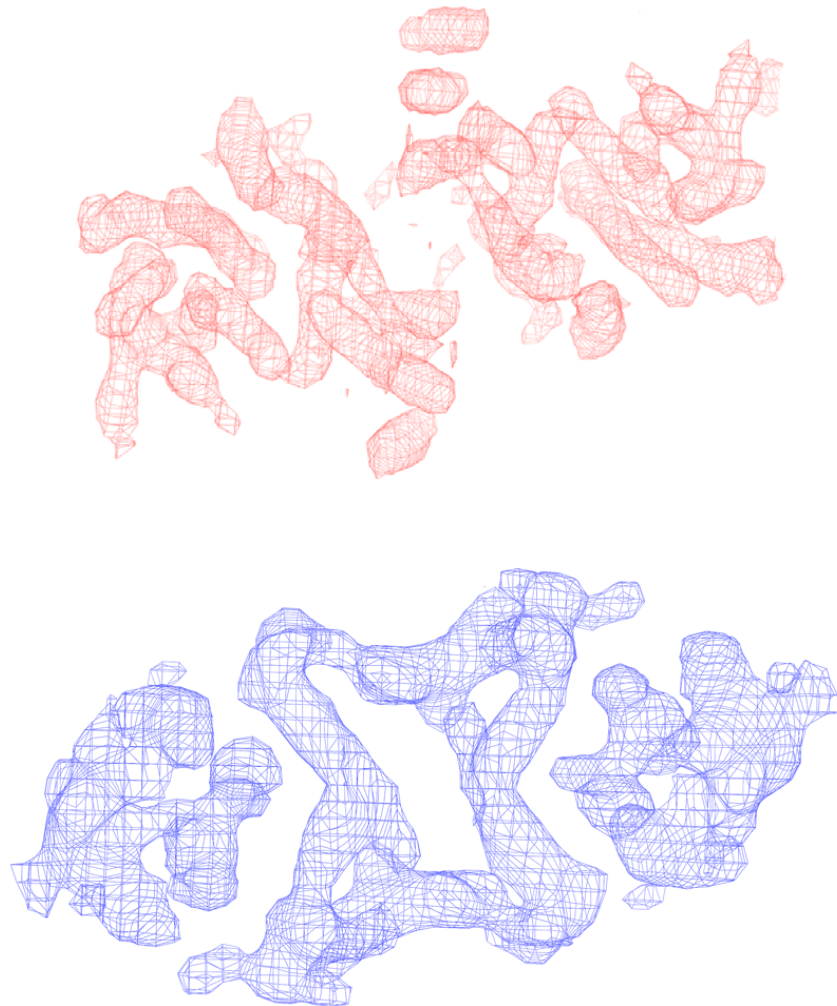
Figure 39 Comparison of 3D maps of NhaA and MjNhaP1. Perpendicular view of the 3D map of (A) NhaA dimer at pH 4.0 (5) and (B) MjNhaP1 dimer at pH 4.0. The maps show the overall arrangement of helices in the two proteins.

To have a more detailed and clear comparison between the proteins, the X ray structure of NhaA was superimposed onto the 3D model MjNhaP1 (Figure 40). While the central dimer interface shows substantial differences between both antiporters, the helix bundle region differs mainly in the length and slope of the helices. In this region of the outer helix bundle, the discontinuos helices IV and XI of NhaA fit two central helices at a similar position in the 3D map of MjNhaP1. Other helices of the outer bundle of NhaA that fit the outer bundle of MjNhaP1 are III, V, X and XII.

According to alignment of amino acid sequence between both proteins, the outer bundle helices IV and V are the regions of highest sequence conservation (Figure 35) NhaA helices I, II and IX fit similar helical densities in the dimer interface of the MjNhaP1 3D map. Significant differences are visible in the region of the dimer interface of the 3D map of MjNhaP1 occupied by helices VI, VII, and VIII in NhaA. This region shows the extra helical density in the 3D map of MjNhaP1.
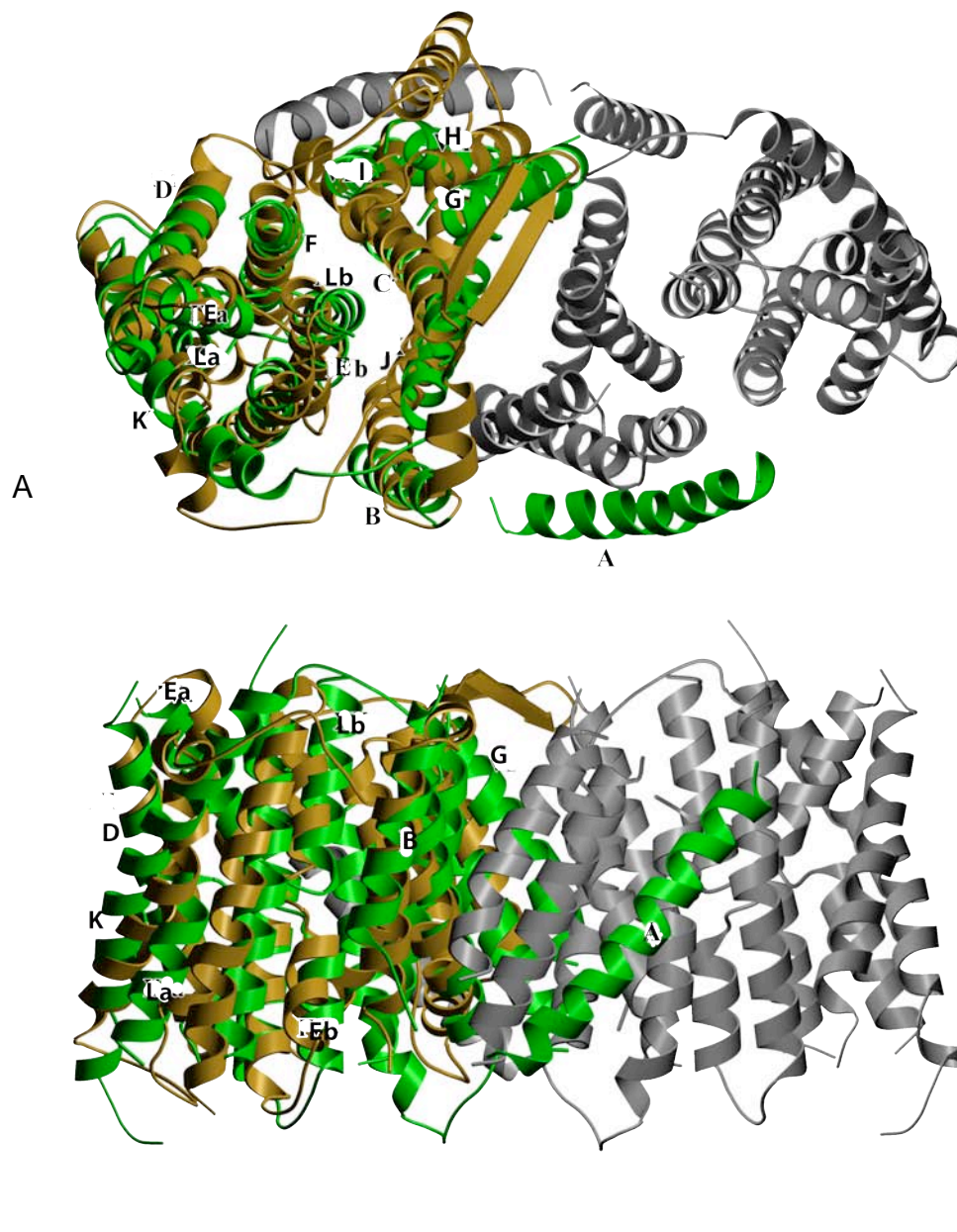
Figure 40 Superimposement of MjNhaP1 dimer model (green, grey) with NhaA monomer (gold) shown perpendicular (A) and (B) along the membrane plane. The two β-strand indicate the periplasmic side of NhaA.
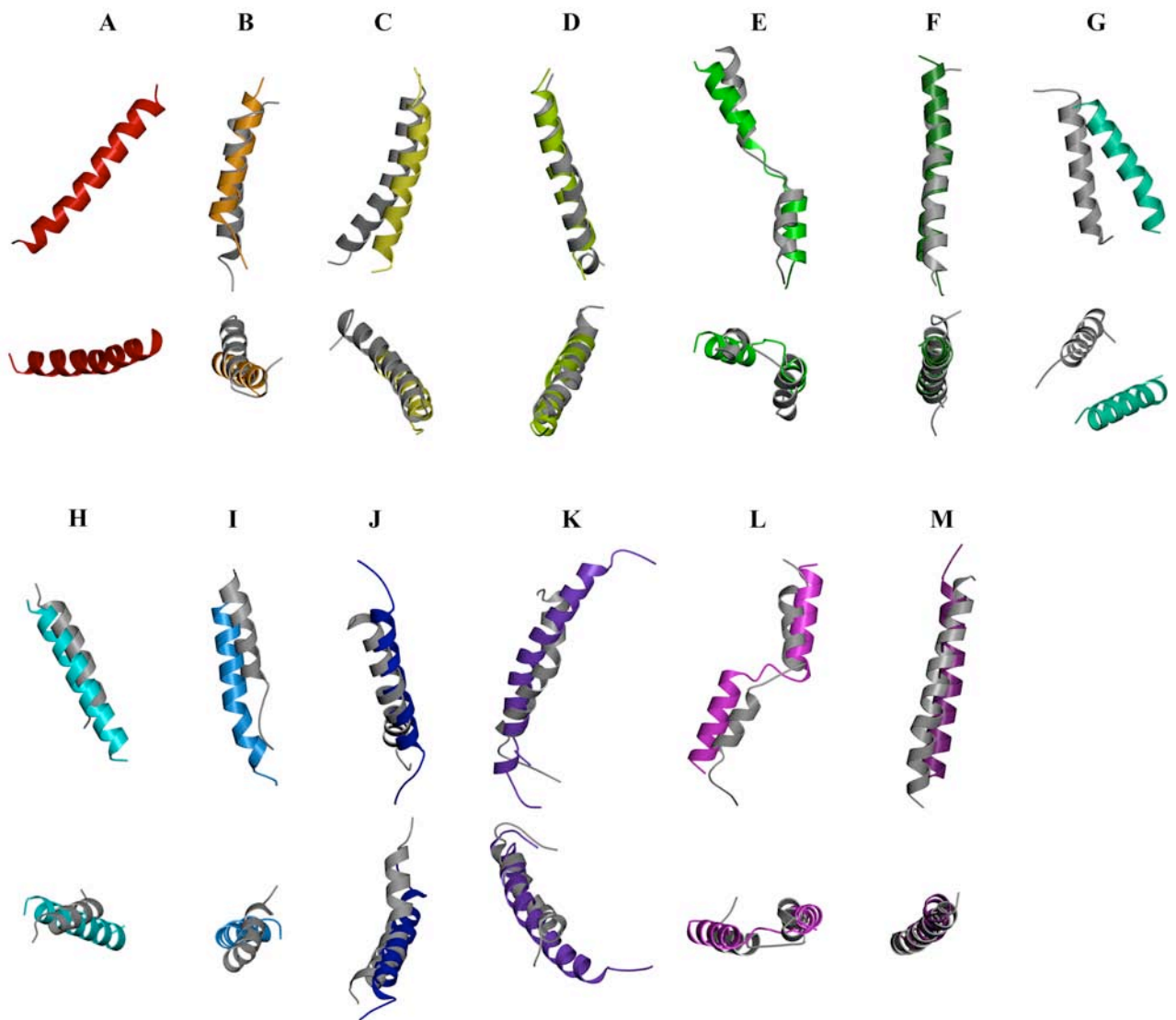
Figure 41 Helix by helix comparison of NhaA (grey) and MjNhaP1 (coloured). Each helix is shown along the membrane plane and the membrane axis.

3.10 Structural duplication in MjNhaP1 helices

Despite the weak sequence homology, helices of MjNhaP1 appear to be structurally related. A duplication event has been observed between pairs of helices in an opposite orientation with respect to the membrane. These pairs are A-I, B-J, D-K, E-L, F-M (Figure 41). It also appears that helix A and helix H share similar tilt angle. Helix G is the only lone helix. This comparison suggests that the N-terminal half of the MjNhaP1 structurally related with the C-terminal part.
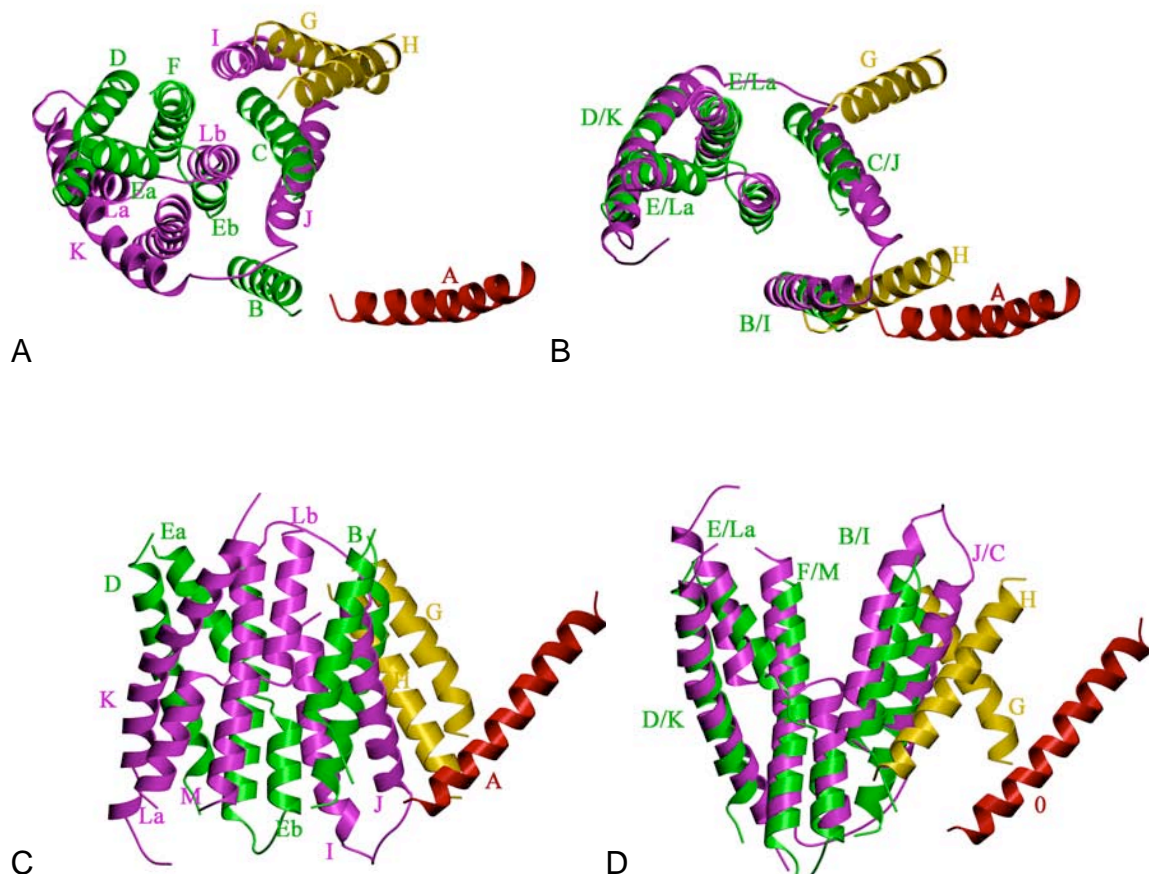
Figure 42   Inverted repeat in MjNhaP1. Helix H-M (purple) is superimposed onto helices B-F (green) in the same monomer. In (A,B) the helices are shown along the membranes axis and in (C,D) in the membrane plane. Due to ambiguous assignment helices A,G and H are coloured in red and gold.

To have a better understanding of this inverted repetition pattern, helices H-M of MjNhaP1 is superimposed to A-F in the same monomer of MjNhaP1. This further indicates that in the outer helix bundle of MjNhaP1 D, E, F and K, L, M are related by inverted repeat as they fit very well. However, in the dimer interface only helices B, C fit I and J, respectively, suggesting that they are related. This analysis gives strong indication that MjNhaP1 has originated most probably by gene duplication.

4 Discussion

4.1 Challenges associated with structural studies of NhaP1

Although structural biology of membrane protein is making headway, yet, this field can be said to be largely unconquered. Approximately 25% of all proteins are membrane proteins and yet less than 150 unique structures are available. The desired method of obtaining high-resolution structural information is by X-ray diffraction of 3D crystals. The pre-requisite for such well-ordered 3D crystals is high quantity of homogeneous protein preparation necessary for screening and optimization of various crystallization conditions. The greatest hindrance in 3D crystallization of recombinant membrane proteins comes in the preparative step where the protein needs to be over-expressed in high quantity and purified to homogeneity.

4.1.1 Expression

The published protocol for expression of MjNhaP1 yielded only 0.5-0.7 mg/ml of purified protein per litre culture. This yield of protein was limiting for optimizing the 3D crystals, which formed under more than one condition. Expression optimization of NhaP1$_{His}$ (MjNhaP1 clone with a C-terminal Hexa-histidine tag) started with exploring different conditions like temperature, media, bacterial strains, induction OD$_{600nm}$, duration of growth, expression under different promoters and different fusion tags. The change of the hexa-histidine tag from the C-terminus end of NhaP1 to the N-terminus end led to two-fold increase in expression level (Figure). Such a drastic effect due to a change in the position of fusion tags lacks a clear explanation and could be the outcome of several factors related to the cell metabolism. One rationale for the success could be that an N-terminal tag ensures that the bacterial transcription and translation machineries always encounter 5' and N-terminal sequences that are compatible with robust RNA synthesis and protein expression, respectively. A comprehensive analysis of codon usage identified over a dozen codons that are used frequently in *Methanococcus jannaschii*, but that are rarely used in *E.coli*. The addition of a hexa-histidine tag with a presence of protease cleavage site could have given a better starting codon usage for the transcription initiation.

A significant increase in the expression level of NhaP1$_{His}$ occurred by changing the method of induction for the promoter of *nhap1*. The classical method where the T7 polymerase was induced in the mid-log phase by IPTG was replaced by an auto-induction or self-induction method (Studier., 2005). In this protocol, T7 polymerase is auto-induced in the late-log growth phase due to depletion of carbon sources other than lactose. Initially the cells in an auto-inducing media use glucose as carbon source. Only when the glucose is depleted lactose is taken up which then starts the induction process. Moreover, the media capable of auto-induction contains magnesium and other sufficient rich nutrients, which remove limitations in cell growth. Also, phosphate in the medium acts as a buffer to maintain a pH near neutral. Under these conditions and a good aeration system, a high cell mass and therefore a high yield of target protein can result.

4.1.2   Purification

Having a monodisperse preparation of recombinant protein requires overcoming various obstacles. The first critical step is to choose the right detergent for solubilizing and purifying the protein, which can maintain the protein in an unaggregated state. MjNhaP1 has been successfully solublized and purified in DDM. DDM retains membrane proteins in a native-like structure and has been so far the most successful of all detergents for the crystallization of α-helical type membrane targets.

Nevertheless, the micelle size of 12-carbon atom-chain length of DDM had two disadvantages. First, DDM micelles were large enough to engulf impurities having similar molecular weight as MjNhaP1. This made it very difficult to remove the impurities, which were observed just beneath MjNhaP1 on the SDS page. Second, large DDM micelles size can hinder crystal contacts between neighbouring protein molecules. This could be the reason that 3D crystals of MjNhaP1 lacked growth in the third dimension and were plate like in appearance. Switching to OG, with an 8-carbon atom-chain length, could drastically remove the impurities. Regardless, the small micelle size OG could not keep MjNhaP1 stably in solution. Amongst the detergents surveyed, MjNhaP1 was particularly stable in maltoside detergents, including dodecylmaltoside, undecylmaltoside (UDM), decylmaltoside (DM), Cymal-7 and Cymal-5, (Appendix II). Optimization of purification and 3D crystallizations holds promise for these detergents.

MjNhaP1 has been successfully purified with a hexa-histidine tag at the C-terminus. In this work, we have also purified NhaP1 with a hexa histidine tag in the N-terminus, which holds the possibility of being removed by PreScission enzyme. Removal of the purification tags has been useful in 3D crystallization, for example, an improvement was observed in the quality of 3D crystals of rhomboid intramembrane serine proteases from *Pseudomonas aeruginosa* following the cleavage of the hexa-histidine tag by TEV-protease (Willis and Koth, 2008). However, the PreScission cleavage site could not be cleaved off on the column but in solution only. It is more useful to remove a tag on the column as it can help in more efficient elution and avoid the trouble of separating cleaved and uncleaved population.

A characteristic brown colour was observed in the elution from the nickel column. This was initially assumed to be lipids sticking to the protein or a mixed micelle of lipid and detergent. TLC revealed no characteristic lipid. A second speculation was towards presence of some sugar molecule sticking to the protein. It was found that increasing the detergent concentration minimized the colour. As mentioned above, MjNhaP1 is stable in detergent with a sugar head group. Perhaps the stability of the protein is enhanced with a sugar support. Such brown coloured protein is stable at room temperature for several days but never formed 3D crystals. However, such brown coloured batched of purified protein are able to form 2D crystals and during the process of dialysis the solution turns colourless.

4.2   Critical parameters in the determining the 3D map of NhaP1

Structure determination by electron crystallography is quite laborious and time-consuming as this methodology lacks in several advanced techniques available in X-ray crystallography. As there are no high-throughput screening techniques, it takes time and effort to produce high quality 2D crystals. The process of data collection is also quite tedious and the existing softwares for data processing is not nearly as user-friendly as the software packages used in X-ray crystallography. The critical factors, which allowed the successful determination of this intermediate resolution 3D map of NhaP1, are here summarized.

1. Data collection with highly tilted 2D crystals is a challenging task and requires considerable effort. When the tilt angle increases, the visible section of the EM grid diminishes and only few grid squares are visible. An increase in the probability of

successful image recording requires that the cryo-grid be densely occupied with well-ordered large crystals.

Majority of the high-resolution membrane protein structures bacteriorhodopsin, LHC II, Aquaporin 0 by electron diffraction of 2D crystals has been obtained from large crystalline sheets. In order to grow larger crystals, preferably sheets, extensive screening was carried out. Large vesicles are a common encounter but they were never well ordered. In some cases a mixed population of tubes and sheets were obtained. Sheets were always fewer and less well ordered compared to the tubes. A general tendency of NhaP1 to crystallize into tubes was observed under various reconstitution conditions. As mentioned earlier NhaP1$_{His}$ has been purified in OG in a monodisperse state. Although of high purity, NhaP1$_{His}$ in OG has been found to be unstable and form aggregates. But quite unexpectedly very broad, well-ordered crystalline tubes of 1.5µm-2µm could be obtained which showed good quality diffraction. This can occur if the aggregates are of one type and these aggregates stressed by a change in temperatures can lead crystal growth (Mosser, 2001). Furthermore, OG, which has a higher CMC than DDM, could have altered the overall kinetics of dialysis thereby enhancing crystal size.

2. Having a good cryo-specimen is one of the most crucial steps in obtaining good images of 2D crystals, which has to be optimized for each specimen. All images were collected with the JEOL3000SFF which is equipped with a helium-cooled top-entry specimen stage. This made it possible to quickly exchange EM grids until a suitable specimen had been obtained for data collection.

3-D data obtained from 2D crystals suffer from loss of information in the z-direction, which arises due to the missing of a cone-shaped part of the 3-D set of complex structure factors. A solution to minimize this missing cone is to have a good quantity of isotropic data at higher tilt angle. It is a common phenomenon to loose information in the direction perpendicular to the tilt axis as high tilt data collection is quite sensitive to specimen flatness. In the 3D reconstruction of NhaP1 a good number of reasonably isotropic images to a resolution of 10Å could be obtained for specimen tilted to 45°. Most of this "good data" was obtained with thick carbon films, around 100Å, coated on new, clean copper grids. The key to successful data collection at high tilt angle is, however, purely strategic trial-and-error repetition, and is still the only way known to eventually get a specimen grid with a reasonable yield of crystals lying flat.

4.3 The 3D map of MjNhaP1

The 3D map of MjNhaP1 at 7Å resolution is the first three dimensional information of a Na$^+$/H$^+$ exchanger from archaea. The fact that MjNhaP1 has opposite pH properties to that of *E. coli* NhaA makes it an interesting candidate for understanding the mechanism of pH regulation of such membrane transporters. By biochemical studies like site-directed mutagenesis followed by activity measurements, important residues for antiporter activity could be identified (Hellmer et al., 2003). In addition, projection maps of MjNhaP1 calculated by cryo-electron microscopy were helpful in mapping the conformational changes upon change of pH (Vinothkumar et al., 2005) .

The cryo-EM 3D map of MjNhaP1, these existing biochemical and structural information and a comparison with the well charateized *Ecoli* NhaA is a step towards understanding the working mechanism of this antiporter.

4.3.1 Structural and functional conservation

By ConSurf analysis, it is possible to map the phylogenetic information onto a protein tertiary structure to identify putative functional regions. Such an analysis of the NhaA crystal structure has shown that the core of the helix IV and helix XI, which forms the unwound part, is the evolutionarily most conserved region (Kozachkov et al., 2007). As shown in the sequence alignment, this conservation is also found in the corresponding helices of MjNhaP1 (Figure 34) suggesting an important role in transport activity and pH sensing. The unwound helices IV and XI of NhaA align to putative helix E and L of MjNhaP1. The highly coserved motifs TDP and GPRGVVP found in NhaP family of antiporters are located in these putavtive helices E and L, respectively. Functional studies in MjNhaP1 (Hellmer et al., 2003) show that mutation of the D132 in TDP motif and R347 in GPRGVVP leads to loss of antiporter activity.

Based on the sequence conservation and the good superimposition of corresponding helices IV and XI of the NhaA X-ray structure and MjNhaP1 3D map, we suggest that MjNhaP1 also has similar half-helical assembly formed by the putative helix E and L. As discussed earlier there are few other membrane protein structures that contain disrupted helices (reviewed in Screpanti and Hunte, 2007) that can be either membrane spanning or in a hairpin-like arrangement. Each of these helices contains a "α-helix extended peptide α-helix" motif. Such a structural element appears to be highly favourable for ion binding. Their location in the membrane non-polar

109

environment requires ion binding in desolvated states that ensures high selectivity on the basis of ion charge and size. Helices IV and XI are part of the inversion motif. Such an arrangement could also be ideal for ion coordination due to the presence of partially charged helix termini. Furthermore, compared to α-helices extended peptide may confer flexibility at lower energetic cost for conformational changed during the transport process.
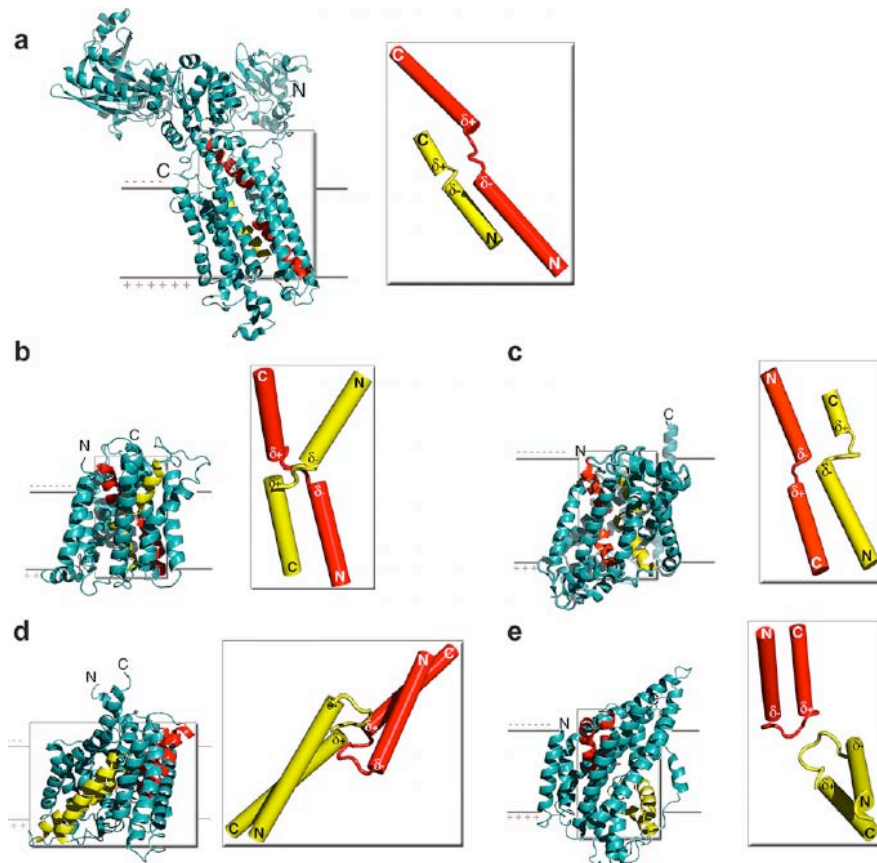
Figure 43 Crystal structures of transport proteins with discontinuous helices. (a) Ca^{2+}-ATPase (b) NhaA (c) LeuTAa (d) ClC Cl^{-}/H^{+} exchanger (e) GltPh. Figure adapted from (Screpanti and Hunte, 2007).

The effect of pH on the structure of MjNhaP1 was examined *in situ* by incubating the tubular crystals in pH8 buffer on the EM grid, and trapping any change by rapid freezing. Significant differences in the projection structures at pH4 and pH8 were evident by visual comparison (Figure 44). In particular, a peak between two of the helix densities (asterisk in Figure 43, MjNhaP1 at pH4) disappears at high pH, and the density peaks within the bundle change shape, suggesting a tilting or rotating movement of individual helices. A difference map indicated a significant rearrangement of densities in the helix bundle, and a moderate displacement of the helix bundle relative to the central dimer core (Vinothkumar et al.,2005).
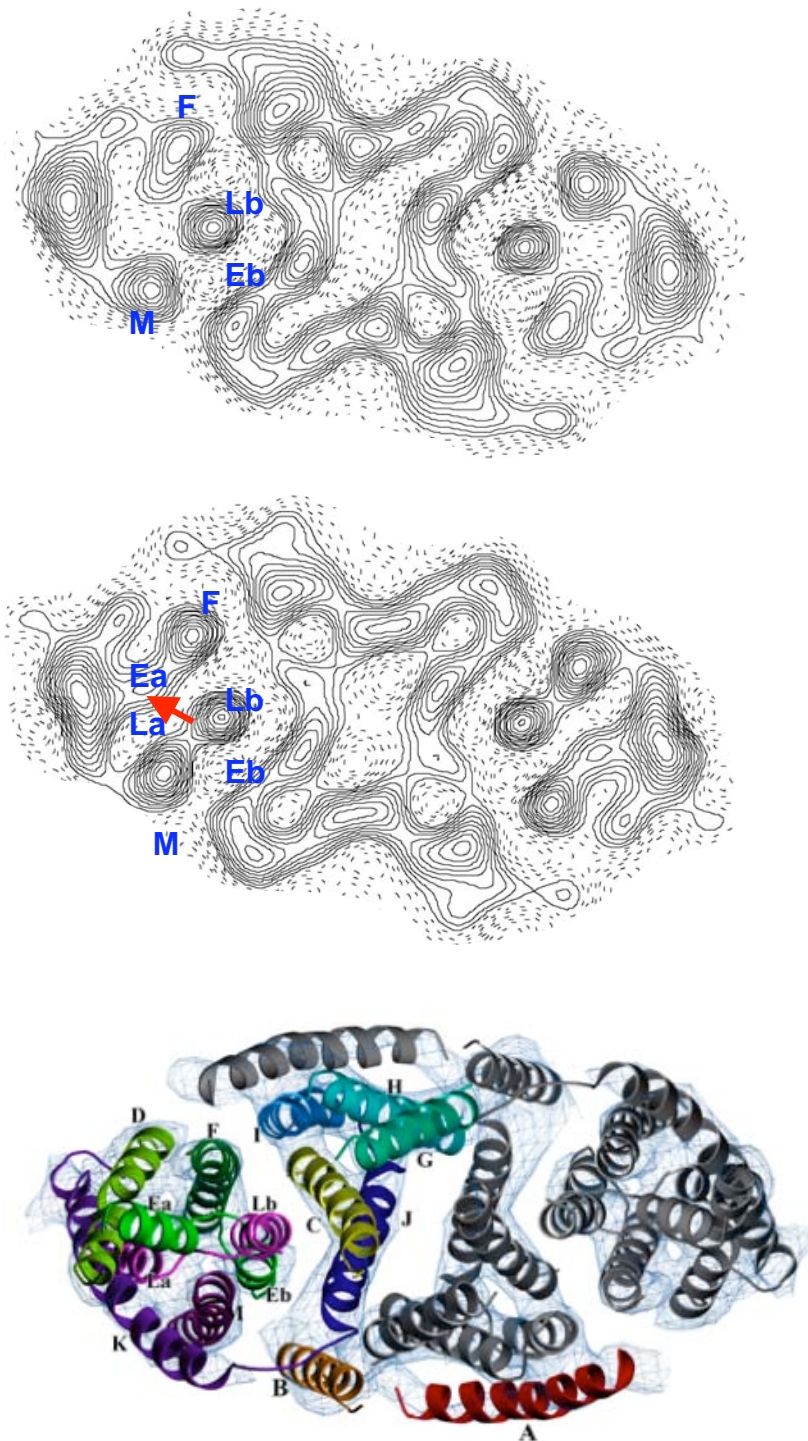
Figure 44 Helices important in antiporter activity in MjNhaP1. Projection map of MjNhaP1 (Vinothkumar et al., 2005) at (A)pH 8 (B) pH 4. The red arrow in (B) points to a density(peak) at pH 4 which disappears at pH 8 .Comparison of assigned helices in the MjNhaP1 model with the helices in the projection maps suggests that the peak which disappears at pH 8 is formed by half helices Ea and/or La.

A comparison of the projection map with the 3D map of NhaP1 showed that helices which show reorientation due to pH change are in the position of the putative helices F, E and L (Figure 43). All these gives strong indication that the disrupted helices E

and L and putative helix F in the outer bundle of MjNhaP1 molecule forms the prime functional entity that play a role in the transport mechanism of Na^+/H^+ antiporters in archaea.

The negative dipoles of the opposing short helices XIc and IVp of the IV and XI transmembrane segments of NhaA contribute to a delicately balanced electrostatic environment in the middle of the membrane. A lysine residue K300 in helix X of NhaA plays a crucial role in the charge compensation of this dipole in the middle of the membrane (Gonen et al., 2005). The sequence alignment suggests that R320 in MjNhaP1 probably takes the function of K300. The importance of R320 for MjNhaP1 has been shown by activity measurements (Hellmer et al., 2003). Overall, helix X of NhaA and putative helix K of MjNhaP1 have a stretch of conserved residues in the centre. Conserved residues have also been identified in flanking helices V in NhaA, facing the crossing of the IV and XI transmembrane helices. Biochemical and simulation studies have shown that these residues are crucial in the transport mechanism. D163 and D164 of helix V of NhaA have been proposed as the accessibility control switch and ion-binding site respectively (Arkin et al., 2007). Likewise, the homologous D161 in the FNDP motif of putative helix F MjNhaP1 is essential for transport activity as shown by mutagenesis (Hellmer et al., 2003). The remaining two helices, III and XII of NhaA that aligns with putative helices D and M in MjNhaP1 have so far not been assigned a specific role. However, mutagenesis has identified the D93 in helix D of MjNhaP1 to be essential for antiporter activity (Hellmer et al., 2003).

In the dimer interface, the two central helices C and J have the same orientation and position in both proteins. Structure based functional studies in the central helix IX and loop VIII-IX of NhaA have revealed that they contain amino acids that play role in multiple functions (Tzubery et al., 2008) act as pH sensor, connect TMS IX to TMS XI of the translocation machinery, line the cytoplasmic cation funnel leading to the active site and participate in the dimer interface. Like helix IX of NhaA, the corresponding helix J of MjNhaP1 is also kinked or distorted. Such a kinked or distorted helix appears flexible and participates in long-range conformational changes (Hunte et al., 2005). Cys accessibilty tests and cross-linking studies have shown that Phe-Phe interaction between F267 in helix IX and F344 in helix XI of NhaA is essential for antiporter activity. In addition, mutant F267C has a low H^+/Na^+ stoichiometry and unable to utilize and thus cannot confer resistance at alkaline pH in the presence of Na^+ (Tzubery et al., 2008). There exists a homologous residue F287 in the putative

helix J of MjNhaP1 for the NhaA F267, but no F aligns with F344. Hence, the F of putative helix J in MjNhaP1 probably interacts with some other residue in the translocation machinery. The in-tandem part of loop VIII-IX appears suitable to participate in the pH sensor of NhaA (Hunte et al., 2005). In our 3D map at 7Å resolution this loop region is visible and is superimposed by the VIII-IX loop region of the NhaA X-ray structure.

4.3.2 Functionally important motifs in eukaryotic Na⁺/H⁺ exchangers

Despite exchanging Na^+ for H^+, the Na^+/H^+ exchanger serves different functions in different cell types. In this work a comparison of sequences of distantly related Na^+/H^+ exchangers, bacterial, archael and eukaryotic (isoforms) has been carried out. This study suggests that these antiporters do not have long overall sequences of amino acids that are homologous. Generally, identical short amino acid sequences between proteins from different domains of life might indicate a common evolutionary origin or function (Frohlich and Young, 1996). It is clear from this alignment that the mammalian isoforms are closely related, but that there is less similarity when comparing them with bacteria or archael exchangers. This low similarity makes it difficult to identify amino acid residues that are functionally important between distantly related isoforms, though it appears as though some polar amino acids may be conserved.

A study on the NHE1 isoform has shown that the sequence VFFLFLLPPI in the hydrophobic segment corresponding to helix III of NhaA is involved in amiloride-analogue binding (Counillon et al., 1993). The alignment study (3.18) has shown that this common motif is also present in the two other human isoform NHE3, NHE6a and Nhx1 from *S.cerevesiae* and *A.thaliana*. These eukaryotic exchangers also contain a homologous Glu262 in the ES motif in the hydrophobic segment corresponding to helix IV in NhaA which is also present in the archael counterpart and studies have shown earlier that this amino acid is essential for antiporter activity (Fafournoux et al., 1991).

4.4 Signal peptide

Sequence based secondary structure prediction suggested 13 transmembrane helices for MjNhaP1. Sequence alignment of putative transmembrane segments of

MjNhaP1 with the 12 transmembrane helices of NhaA, indicates that the N-terminal transmembrane segment of MjNhaP1 is the additional or thirteenth helix. Our 3D model of MjNhaP1 also suggests that the position of this additional helix is most likely in the N-terminal part of the molecule. Comparing antiporters from different kingdoms shows that this N- terminal helix is present in other archaeal and eukaryotic antiporters but not in any of the bacterial ones. Our results with a web based signal peptide prediction server (SignalP 3.0, http://www.cbs.dtu.dk/services/SignalP) suggests the N-terminal segment of MjNhaP1 and all corresponding segments of the eukaryotic counterparts are most likely signal peptides. Generally, archaeal class I signal peptides are generally 20–30 amino acids long (Bardy et al., 2003) and the N-terminal helix in MjNhaP1 has been predicted to be approximately 21 amino acid long. In this work, MjNhaP1 has been heterologously expressed in *E.coli.* That could explain partly that absence of signal peptidases unique to archaea could leave this signal peptide uncleaved. There are no well-studied reports available so far about processing of signal sequences of integral cytoplasmic membrane proteins in archaea (Sandy Y. M. Ng, 2007). A recent proteomics survey of *Natronomonas pharaonis* and *Halobacterium salinarum* indicates that many, if not most, integral membrane proteins lack cleaved signal sequences (Falb et al., 2006).

Corresponding segments of the additional helix in MjNhaP1 in eukaryotic counterparts have been earlier described as cleaved or uncleaved signal peptides (Miyazaki et al., 2001; Sato and Sakaguchi, 2005; Wakabayashi et al., 2000). Generally, in eukaryotes, endoplasmic reticulum (ER) targeting signal sequences can be either cleaved or uncleaved and are responsible for initiating protein insertion into membranes (High, 1992; High and Dobberstein, 1992). These ER-targeting signal sequences contain a stretch of apolar amino acid residues which are recognized by the signal recognition particle (SRP) (Lutcke et al., 1992). Complex membrane proteins with several membrane-spanning helices achieve their final orientation by using signal-anchor and stop-transfer sequences (Blobel, 1980). The N-terminal region including a transmembrane segment TM1 of the human homolog Na^+/H^+ exchanger NHE1, has been predicted to contain a highly hydrophobic signal peptide (Wakabayashi et al., 2000). Experiments where loops were biotinylated in a MTSET-sensitive manner suggested that residues including cysteine at position 35 near the extracellular interface of TM1 were retained in the mature NHE1 protein. A mutant where 8 cysteines were replaced except for the most N-terminus one was labeled only after cells were permeabilized suggesting that Cys8 is also retained in the

mature protein and localized in the cytosol. It is therefore most likely that the signal peptide in NHE1 is not cleaved during protein processing, unless introduced individual cysteines somehow prevent the cleavage of protein by signal peptidases (Wakabayashi et al., 2000). Another isoform of the Na$^+$/H$^+$ exchanger, NHE6, localizes exclusively in the secretory pathway and the N-terminal hydrophobic segment has been identified as a signal peptide that directs the molecule to the Endoplasmic reticulum and later cleaved off (Miyazaki et al., 2001). By contrast, data shows that although the plant NHX isoforms can form the same membrane topology proposed for the human NHE family, it lacks the signal peptide (Sato and Sakaguchi, 2005). All these suggest that the fate of the signal peptide appear to be different in different isoforms of the eukaryotic family of Na$^+$/H$^+$ exchangers and the presence of an uncleaved signal peptide cannot be ruled out. Hence, the corresponding N-terminal hydrophobic segment in MjNhaP1 is also strongly indicative of representing an uncleaved signal peptide characteristic of the archaeal family of Na$^+$/H$^+$ antiporters.

4.4.1   Topology of MjNhaP1

The 3D map of MjNhaP1, web-based topology prediction programmes and the sequence alignment with several other Na$^+$/H$^+$ exchangers suggest the presence of 13 transmembrane segments in MjNhaP1. The medium resolution of the 3D map of MjNhaP1 does not give any information of the orientation of the molecule in the membrane bilayer. We attempt to propose the topology of this protein considering various existing facts.

1. The crystal structure of the homologous protein NhaA where there are 12 transmembrane segments showed that both its N- terminus and C-terminus are in the cytoplasm. Although the two proteins (NhaA and MjNhaP1) superimposes relatively well, this does not define the topology of MjNhaP1. There is a possibility that the extra putative transmembrane helix in MjNhaP1 has inverted the orientation with respect to NhaA. For example, in *E. coli*, the putative Arg and ornithine antiporter YdgI has an extra C-terminal transmembrane helix compared to its close homologues, PotE and YjdE. In this case the homologous proteins are oppositely oriented [reviewed in (Heijne, 2006)].

2. Generally, positively charged residues are more frequently found on the cytoplasmic compared to the non-cytoplasmic side of an integral membrane protein following the positive inside rule (Heijne, 1986; Nilsson et al., 2005). According to this, each protein is orientated such that the side containing the higher number of positively charged Arg and Lys residues faces the cytoplasm. The distribution of positive charges in the predicted secondary structure topology model of MjNhaP1 (Figure 15) are such that a total of seventeen Lys and Arg residues are found on one side compared to two on the other side of the membrane. This would mean that the N-terminus of MjNhaP1 should be in the periplasm and the C-terminus should be in the cytoplasm in contrast to the depiction by Hellmer and colleagues (Hellmer et al., 2003). Such topology prediction based on charge distribution can be supported by the secondary structure model of the *E. coli* homolog NhaA which had shown 19 positive (Lys and Arg) residues on the cytoplasmic side while only two of these positive residues were shown on the periplasmic side (Rothman et al., 1996). Years later, the X-ray structure (Hunte et al., 2005a) confirmed this prediction and revealed that NhaA with 12 transmembrane helices had both the C-terminus and N-terminus in the cytoplasm.

Membrane proteins with uncleaved signal anchor sequences of both type I (N_{exo}/C_{cyto} topology) and type II (N_{cyto}/C_{exo})_orientation have been identified (von Heijne, 1988). The final orientation that a signal anchor protein assumes in the membrane depends on the nature of the hydrophilic amino acid residues that flank the hydrophobic core of the signal-anchor sequence. Studies also show that the number and type of charged amino acid residues in the regions flanking the hydrophobic core of the signal anchor sequence determine membrane orientation (Beltzer et al., 1991; Parks and Lamb, 1991; Sato et al., 1990). Predictions of orientation of multiple membrane spanning proteins are prone to errors and require experimental verifications (High and Dobberstein, 1992).

4.5   Gene duplication in secondary transporters

Nearly the whole molecule of MjNhaP1 shows an inverted repeat. The outer bundle in MjNhaP1 contain two groups of three helices each, one group in the centre of the monomer and the other towards the periphery. In the outer bundle, the three

peripheral helices can be superimposed perfectly in an inverted manner on the three central. Likewise, helix B and C fit helix I and J very well. This kind of inverted repeat suggests a gene duplication event. Presence of inverted repeats or duplication domains is an interesting feature in several integral membrane protein structures. Such inverted duplication domains have been observed in several channels and transporters. These kinds of structural feautures influence the topoplogy and throw light on the evolution of membrane proteins (Pornillos and Chang, 2006). Amino acid sequences usually do not depict this structural repeat. In the ClC Cl$^-$/H$^+$ exchanger, the whole molecule shows an inverted internal repeat (Dutzler et al., 2002). The three-dimensional structure revealed that the N-terminal half of the polypeptide is structurally related to the C-terminal half. These two similar structures are oriented in opposite direction in the membrane and run antiparallel to create a pseudo two-fold symmetry axis within the membrane. A weak repetition pattern was observed in the amino acid sequence of the two halves only after knowing the three-dimensional structure.

Structural symmetry in terms of inverted repeats was also observed partly for the molecule NhaA, LeuTAa and GltPh. Two bundles in NhaA with three TMSs (III, IV, V and X, XI, XII) form the outer helix bundle, in which the ion transport occurs. The two bundles of domain A form a duplication motif with opposite orientation with respect to the membrane and two disrupted helices IV and XI are part of the inversion motif (Hunte et al., 2005a). In the LeuTAa transporter a pseudo twofold axis parallel to the membrane plane relates TMSs 1–5 and TMSs 6–10 (Yamashita et al., 2005). For the glutamate transporter homologue structure, GltPh a very good fit was observed for HP1 and HP2 (hairpins 1 and 2) (Yernool et al., 2004).
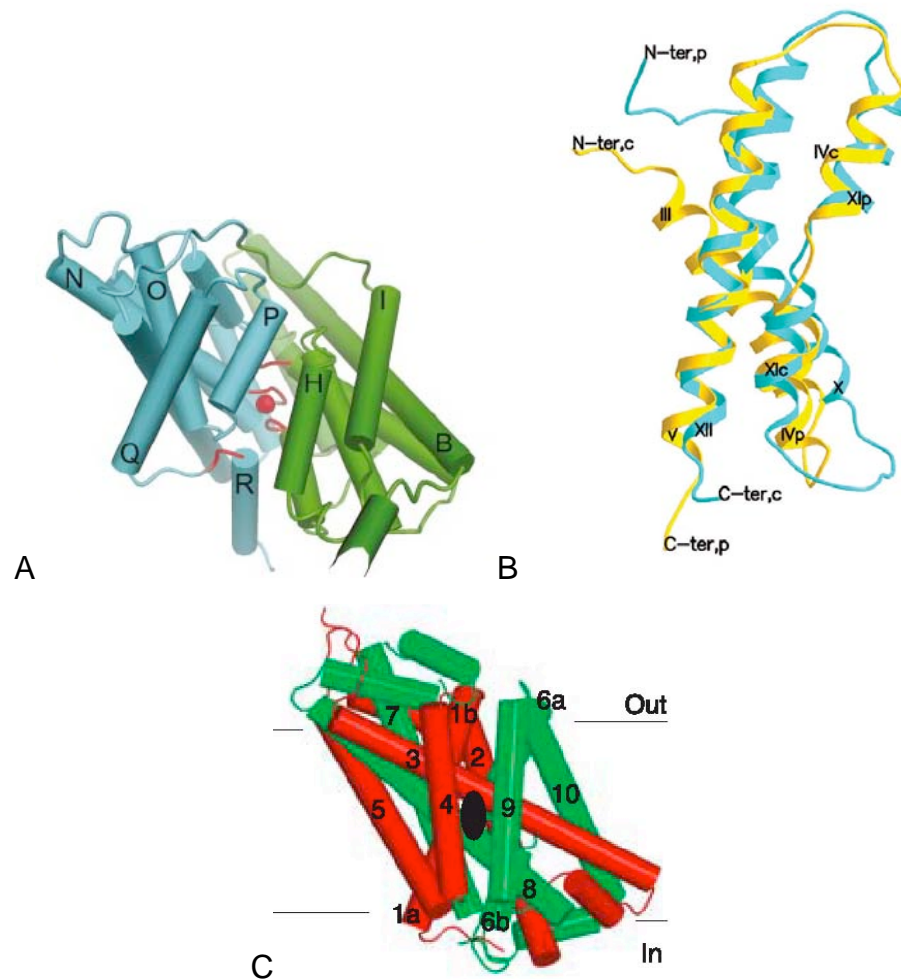
**Figure 45 Cylinder and ribbon representation of ClC chloride channel, NhaA and LeuTAa. A.
The X-ray structure of ClC chloride channel where the N-terminal half of the polypeptide (alpha-
helices B–I, green) is structurally related to the C-terminal half (J–Q, blue). B. In the NhaA
molecule, superimposition of TMS III, IV and V (yellow) onto TMS X, XI and XII (cyan) and their
loops show that the two elements are structurally related C. In the LeuTAa molecule a pseudo-
two-fold axis of symmetry relates TM1−TM5 (red) to TM6−TM10 (green).**

4.6   Summary and Outlook

In this work, the three-dimensional architecture of the Na^+/H^+ antiporter of *M.
jannaschii* has been determined by cryo-electron crystallography at 8Å resolution. So
far the three dimensional structure of only one representative of the Na^+/H^+
exchanger family, the *E.coli* NhaA, is known. Although the resolution at which the 3D
map of MjNhaP1 has been obtained is medium, a number of interesting features
have been revealed. The 3D map suggests the presence of a conserved structural

118

fold between *M. jannaschii* MjNhaP1 and *E.coli* NhaA, which in NhaA has been predicted to play a role in the transport activity. A model of MjNhaP1 could be generated by manual fitting of helices into the 3D map with the X-ray structure of NhaA as a template. A 13th helix could be identified in the model, which appear to mediate dimer interactions in the NhaP1 molecule. A sequence alignment study and the 3D model suggest that this additional helix is located in the N-terminal part of MjNhaP1 and functions as a signal peptide. Detailed analysis of the helices of MjNhaP1 revealed the presence of inverted repeats where the helices B to D can be superimposed with helices I to M suggesting that they arose from gene duplication. The 3D map has opened several questions and has brought forward many interpretation which needs to answered or confirmed.

1. MjNhaP1 in the active conformation

Cryo-electron crystallography enables study of conformational changes or intermediate states of membrane proteins. For example, analysis of 2D crystals of the K^+ channel, KirBac3.1 from *Magnetospirillum magnetotacticum*, had shown that opening of the ion conduction pathway could be achieved by bending of the inner helices and significant movements of the outer helices. This was achieved by studying differences in projection maps obtained from two distinct crystal forms: crystal form 1, the "closed conformation" as the pore in this conformation is hardly visible and crystal form 2, the pore is clearly identified and called the "open conformation" (Kuo et al., 2005). Similarly, images were recorded using tubular crystals of nicotinic acetylcholine receptor, which were activated and then trapped by rapid freezing. The map revealed an altered configuration of M2 α-helical segment compared to the closed structure (Unwin, 1995). Therefore, 2D crystals of MjNhaP1 give us the unique chance of trapping the antiporter in distinct, active, or inactive states. Having completed the 3D map of MjNhaP1 at pH 4, where it has to be locked, determination of 3D maps at pH 6.5, where it is active, and pH 8, where it is inactive will give an in-depth understanding of pH induced conformational changes.

2. Presence of uncleaved signal peptide

To verify whether the additional helix is a signal peptide, experimental evidence is necessary. In addition, such evidences would also give an idea about the topology of MjNhaP1. A technique called the fluorescence protease protection (FPP) assay is generally applied to determine the topology of membrane proteins (Lorenz et al., 2006). A restricted proteolytic digestibility of GFP-tagged transmembrane proteins is

carried out which allows identification of orientation of proteins in the membrane. For this method GFP fusion proteins are expressed and then treated with protease with and without selective permeabilization of the plasma membrane. The location of the tagged end can be identified on the basis of accessibility of proteases to exposed polypeptides versus their inaccessibility to polypeptides that are located in 'protected' intracellular regions such as the lumen of organelles. Creating two fusion proteins, one with an N-terminal GFP tag and another with C-terminal GFP tag, and identifying whether the tagged end is localized in the exoplasm or cytoplasm, should determine the topology of MjNhaP1.

The 3D map also suggests that this additional helix A mediates dimer interaction. This role of this helix A would also require further biochemical evidence. Analyzing the structural and functional behaviour of a mutant form of MjNhaP1, where the additional helix A is deleted, would illustrate its role in dimer formation.

3. High-resolution structure

Although the 3D map provides a first glimpse of the three-dimensional architecture of this antiporter, an atomic structure will be necessary to understand the transport mechanism in detail. The reproducibility of 3D crystals holds promise for a high-resolution structure in the future. In parallel, optimization of the expression level of MjNhaP1 in *E. coli* will be necessary to carry out various 3D crystallization trials for X-ray structure determination. The combination of a high-resolution X-ray structure modelled to different conformations at lower resolution will help in studying the mechanisms of transport and pH regulation in MjNhaP1.

5 References

Abramson, J., Smirnova, I., Kasho, V., Verner, G., Iwata, S. and Kaback, H.R. (2003a) The lactose permease of Escherichia coli: overall structure, the sugar-binding site and the alternating access model for transport. *FEBS Lett*, **555**, 96-101.

Abramson, J., Smirnova, I., Kasho, V., Verner, G., Kaback, H.R. and Iwata, S. (2003b) Structure and mechanism of the lactose permease of Escherichia coli. *Science*, **301**, 610-615.

Agard, D.A. (1983) A least-squares method for determining structure factors in three-dimensional tilted-view reconstructions. *J Mol Biol*, 167(4):849-52

Apse, M.P., Aharon, G.S., Snedden, W.A. and Blumwald, E. (1999) Salt tolerance conferred by overexpression of a vacuolar Na+/H+ antiport in Arabidopsis. *Science*, **285**, 1256-1258.

Arkin, I.T., Xu, H., Jensen, M.O., Arbely, E., Bennett, E.R., Bowers, K.J., Chow, E., Dror, R.O., Eastwood, M.P., Flitman-Tene, R., Gregersen, B.A., Klepeis, J.L., Kolossvary, I., Shan, Y. and Shaw, D.E. (2007) Mechanism of Na+/H+ antiporting. *Science*, **317**, 799-803.

Armstrong, C.M.a.H., B. (1998) Voltage-gated ion channels and electrical excitability. *Neuron*, **20**, 371-380.

Arora, A., Abildgaard, F., Bushweller, J.H. and Tamm, L.K. (2001) Structure of outer membrane protein A transmembrane domain by NMR spectroscopy. *Nat Struct Biol*, **8**, 334-338.

Baldwin J, H.R. (1988) Images of purple membrane at 2.8Å resolution obatined by cryo-electron microscopy. *J Mol Biol, 202(3):585-91.*

Bardy, S.L., Eichler, J. and Jarrell, K.F. (2003) Archaeal signal peptides--a comparative survey at the genome level. *Protein Sci*, **12**, 1833-1843.

Baumgartner, M., Patel, H. and Barber, D.L. (2004) Na(+)/H(+) exchanger NHE1 as plasma membrane scaffold in the assembly of signaling complexes. *Am J Physiol Cell Physiol*, **287**, C844-850.

Becher, B., Muller, V. and Gottschalk, G. (1992) N5-methyl-tetrahydromethanopterin:coenzyme M methyltransferase of Methanosarcina strain Go1 is an Na(+)-translocating membrane protein. *J Bacteriol*, **174**, 7656-7660.

Beltzer, J.P., Fiedler, K., Fuhrer, C., Geffen, I., Handschin, C., Wessels, H.P. and Spiess, M. (1991) Charged residues are major determinants of the transmembrane orientation of a signal-anchor sequence. *J Biol Chem*, **266**, 973-978.

Blobel, G. (1980) Intracellular protein topogenesis. *Proc Natl Acad Sci U S A*, **77**, 1496-1500.

Booy, F.P. and Pawley, J.B. (1993) Cryo-crinkling: what happens to carbon films on copper grids at low temperature. *Ultramicroscopy*, **48**, 273-280.

Bourguignon, L.Y., Singleton, P.A., Diedrich, F., Stern, R. and Gilad, E. (2004) CD44 interaction with Na+-H+ exchanger (NHE1) creates acidic microenvironments leading to hyaluronidase-2 and cathepsin B activation and breast tumor cell invasion. *J Biol Chem*, **279**, 26991-27007.

Bradford. (1976) A rapid and sensitive method for the quantitation of microgram quantities of protein utilizing the principle of protein-dye binding. *Anal Biochem*, 72, 248-54.

Brett, C.L., Donowitz, M. and Rao, R. (2005) Evolutionary origins of eukaryotic sodium/proton exchangers. *Am J Physiol Cell Physiol*, **288**, C223-239.

Brisson A, U.P. (1985) Quaternary structure of the acteylcholine receptor. *Nature*, **N**.

Carmel, O., Rahav-Manor, O., Dover, N., Shaanan, B. and Padan, E. (1997) The Na+-specific interaction between the LysR-type regulator, NhaR, and the nhaA gene encoding the Na+/H+ antiporter of Escherichia coli. *EMBO J*, **16**, 5922-5929.

Carpenter, E.P., Beis, K., Cameron, A.D. and Iwata, S. (2008) Overcoming the challenges of membrane protein crystallography. *Curr Opin Struct Biol.*

Charnock JS, R.A., Post RL. (1963) Studies of the mechansim of cation transport. II.A phosphorylated intermediate in the cation stimulated enzymic hydrolysis of adenosine triphosphate. *Aust J Exp Biol Med Sci.*, **41**, 675-686.

Cherezov, V., Rosenbaum, D.M., Hanson, M.A., Rasmussen, S.G., Thian, F.S., Kobilka, T.S., Choi, H.J., Kuhn, P., Weis, W.I., Kobilka, B.K. and Stevens, R.C. (2007) High-resolution crystal structure of an engineered human beta2-adrenergic G protein-coupled receptor. *Science*, **318**, 1258-1265.

Clamp, M., Cuff, J., Searle, S.M. and Barton, G.J. (2004) The Jalview Java alignment editor. *Bioinformatics*, **20**, 426-427.

Clore, G.M. and Gronenborn, A.M. (1997) NMR structures of proteins and protein complexes beyond 20,000 M(r). *Nat Struct Biol*, 849-853.

Corpet, F. (1988) "Multiple sequence alignment with hierarchical clustering." *Nucl. Acids Res*, **16(22):10881-90**.

Counillon, L., Franchi, A. and Pouyssegur, J. (1993) A point mutation of the Na+/H+ exchanger gene (NHE1) and amplification of the mutated allele confer amiloride resistance upon chronic acidosis. *Proc Natl Acad Sci U S A*, **90**, 4508-4512.

Crowther, R.A. (1996) MRC image processing programs. *J Struct Biol., 116(1),9-16.*

Csaky, T.Z. (1965) Transport through Biological Membranes. *Annu Rev Physiol*, **27**, 415-450.

Daleke, D.L. (2003) Regulation of transbilayer plasma membrane phospholipd asymmetry. *J. Lipid Res.*, **44**, 232-242.

Dall, P., Heider, K.H., Sinn, H.P., Skroch-Angel, P., Adolf, G., Kaufmann, M., Herrlich, P. and Ponta, H. (1995) Comparison of immunohistochemistry and RT-PCR for detection of CD44v-expression, a new prognostic factor in human breast cancer. *Int J Cancer*, **60**, 471-477.

Deisenhofer, J., Epp, O., Miki, K., Huber, R. and Michel, H. (1984) X-ray structure analysis of a membrane protein complex. Electron density map at 3 A resolution and a model of the chromophores of the photosynthetic reaction center from Rhodopseudomonas viridis. *J Mol Biol*, **180**, 385-398.

Deppenmeier, U., V. Müller, and G. Gottschalk. (1996) Pathways of energy conservation in methanogenic archae. *Arch. Microbiol.*, **165**, 149-163.

Dersch, P., Schmidt, K. and Bremer, E. (1993) Synthesis of the Escherichia coli K-12 nucleoid-associated DNA-binding protein H-NS is subjected to growth-phase control and autoregulation. *Mol Microbiol*, **8**, 875-889.

Dimroth, P. and Hilbi, H. (1997) Enzymic and genetic basis for bacterial growth on malonate. *Mol Microbiol*, **25**, 3-10.

Dover, N., Higgins, C.F., Carmel, O., Rimon, A., Pinner, E. and Padan, E. (1996) Na+-induced transcription of nhaA, which encodes an Na+/H+ antiporter in Escherichia coli, is positively regulated by nhaR and affected by hns. *J Bacteriol*, **178**, 6508-6517.

Downing, K.H. (1991) Spot-scan imaging in transmission electron microscopy. *Science*, **251**, 53-59.

Doyle, D.A., Morais Cabral, J., Pfuetzner, R.A., Kuo, A., Gulbis, J.M., Cohen, S.L., Chait, B.T. and MacKinnon, R. (1998) The structure of the potassium channel: molecular basis of K+ conduction and selectivity. *Science*, **280**, 69-77.

Dutzler, R., Campbell, E.B., Cadene, M., Chait, B.T. and MacKinnon, R. (2002) X-ray structure of a ClC chloride channel at 3.0 A reveals the molecular basis of anion selectivity. *Nature*, **415**, 287-294.

E. Pinner, Y.K., E. Padan, S. Schuldiner. (1993) Physiological role of nhaB, a specific Na+/H+ antiporter in Escherichia coli. . *J. Biol. Chem*, **268**, 1729-1734.

Elinder, F., Nilsson, J. and Arhem, P. (2007) On the opening of voltage-gated ion channels. *Physiol Behav*, **92**, 1-7.

Etana Padan, N.M., D. Taglicht, R. Karpel, S. Schuldiner. (1989) Deletion of ant in Escherichia coli reveals its function in adaptation to high salinity and an alternative Na+/H+ antiporter system(s). *J. Biol. Chem*, **264**, 20297-20302.

Fafournoux, P., Ghysdael, J., Sardet, C. and Pouyssegur, J. (1991) Functional expression of the human growth factor activatable Na+/H+ antiporter (NHE-1) in baculovirus-infected cells. *Biochemistry*, **30**, 9510-9515.

Falb, M., Aivaliotis, M., Garcia-Rizo, C., Bisle, B., Tebbe, A., Klein, C., Konstantinidis, K., Siedler, F., Pfeiffer, F. and Oesterhelt, D. (2006) Archaeal N-terminal protein maturation commonly involves N-terminal acetylation: a large-scale proteomics survey. *J Mol Biol*, **362**, 915-924.

Fernandez, C., Hilty, C., Wider, G., Guntert, P. and Wuthrich, K. (2004) NMR structure of the integral membrane protein OmpX. *J Mol Biol*, **336**, 1211-1221.

Fischer, R., Gartner, P., Yeliseev, A. and Thauer, R.K. (1992) N5-methyltetrahydromethanopterin: coenzyme M methyltransferase in methanogenic archaebacteria is a membrane protein. *Arch Microbiol*, **158**, 208-217.

Ford, R.C. and Holzenburg, A. (2008) Electron crystallography of biomolecules: mysterious membranes and missing cones. *Trends Biochem Sci*, **33**, 38-43.

Forgac, M. (1998) Structure, function and regulation of the vacuolar (H+)-ATPases. *FEBS Lett*, **440**, 258-263.

Franzin, C.M., Gong, X.M., Thai, K., Yu, J. and Marassi, F.M. (2007) NMR of membrane proteins in micelles and bilayers: the FXYD family proteins. *Methods*, **41**, 398-408.

Frohlich, O. and Young, L.G. (1996) Molecular cloning and characterization of EPI-1, the major protein in chimpanzee (Pan troglodytes) cauda epididymal fluid. *Biol Reprod*, **54**, 857-864.

Gerchman, Y., Olami, Y., Rimon, A., Taglicht, D., Schuldiner, S. and Padan, E. (1993) Histidine-226 is part of the pH sensor of NhaA, a Na+/H+ antiporter in Escherichia coli. *Proc Natl Acad Sci U S A*, **90**, 1212-1216.

Gerchman, Y., Rimon, A. and Padan, E. (1999) A pH-dependent conformational change of NhaA Na(+)/H(+) antiporter of Escherichia coli involves loop VIII-IX, plays a role in the pH response of the protein, and is maintained by the pure protein in dodecyl maltoside. *J Biol Chem*, **274**, 24617-24624.

Glaeser R M, D.K., DeRosier David, Chiu Wah, Frank Joachim. (2007) Electron Crystallography of Biological Macromolecules. *Oxford University Press, Inc.*, 139-166.

Gonen, T., Cheng, Y., Sliz, P., Hiroaki, Y., Fujiyoshi, Y., Harrison, S.C. and Walz, T. (2005) Lipid-protein interactions in double-layered two-dimensional AQP0 crystals. *Nature*, **438**, 633-638.

Vonck. (2000) Parameters affecting specimen flatness of two-dimensional crystals for electron crystallography. *Ultramicroscopy*, **85(3), 123-9**.

Hasler L. (1998) 2D crystallization of membrane proteins: Rationales and Examples. *J of Struct. Biol*, 121(2), 167-71.

Hamada, A., Hibino, T., Nakamura, T. and Takabe, T. (2001) Na+/H+ antiporter from Synechocystis species PCC 6803, homologous to SOS1, contains an aspartic residue and long C-terminal tail important for the carrier activity. *Plant Physiol*, **125**, 437-446.

Heijne, G.V. (1986) The distribution of positively charged residues in bacterial inner membrane proteins correlates with the trans-membrane topology. *EMBO J*, **5**, 3021-3027.

Heijne, G.V. (2006) Membrane-protein topology. *Nature Reviews*, **7**, 909-918.

Hellmer, J., Patzold, R. and Zeilinger, C. (2002) Identification of a pH regulated Na+/H+ antiporter of Methanococcus jannaschii. *FEBS Lett*, **527**, 245-249.

Hellmer, J., Teubner, A. and Zeilinger, C. (2003) Conserved arginine and aspartate residues are critical for function of MjNhaP1, a Na+/H+ antiporter of M. jannaschii. *FEBS Lett*, **542**, 32-36.

Henderson, R., Baldwin, J.M., Ceska, T.A., Zemlin, F., Beckmann, E. and Downing, K.H. (1990) Model for the structure of bacteriorhodopsin based on high-resolution electron cryo-microscopy. *J Mol Biol*, **213**, 899-929.

Higgins, C.F., Dorman, C.J., Stirling, D.A., Waddell, L., Booth, I.R., May, G. and Bremer, E. (1988) A physiological role for DNA supercoiling in the osmotic regulation of gene expression in S. typhimurium and E. coli. *Cell*, **52**, 569-584.

High, S. (1992) Membrane protein insertion into the endoplasmic reticulum--another channel tunnel? *Bioessays*, **14**, 535-540.

High, S. and Dobberstein, B. (1992) Mechanisms that determine the transmembrane disposition of proteins. *Curr Opin Cell Biol*, **4**, 581-586.

Hille. (2001) Ion channels of excitable membranes (3rd ed.). *Sinauer Associates Inc., Sunderland*.

Hiller, M., Krabben, L., Vinothkumar, K.R., Castellani, F., van Rossum, B.J., Kuhlbrandt, W. and Oschkinat, H. (2005) Solid-state magic-angle spinning NMR of outer-membrane protein G from Escherichia coli. *Chembiochem*, **6**, 1679-1684.

Huang, Y., Lemieux, M.J., Song, J., Auer, M. and Wang, D.N. (2003) Structure and mechanism of the glycerol-3-phosphate transporter from *Escherichia coli*. *Science*, **301**, 616-620.

Hunte, C., Koepke, J., Lange, C., Rossmanith, T. and Michel, H. (2000) Structure at 2.3 A resolution of the cytochrome bc(1) complex from the yeast Saccharomyces cerevisiae co-crystallized with an antibody Fv fragment. *Structure*, **8**, 669-684.

Hunte, C. and Michel, H. (2002) Crystallisation of membrane proteins mediated by antibody fragments. *Curr Opin Struct Biol*, **12**, 503-508.

Hunte, C., Screpanti, E., Venturi, M., Rimon, A., Padan, E. and Michel, H. (2005a) Structure of a Na$^+$/H$^+$ antiporter and insights into mechanism of action and regulation by pH. *Nature*, **435**, 1197-1202.

Hunte, C., Screpanti, E., Venturi, M., Rimon, A., Padan, E. and Michel, H. (2005b) Structure of a Na$^+$/H$^+$ antiporter and insights into mechanism of action and regulation by pH. *Nature*, **435**, 1197-1202.

Hwang, P.M., Choy, W.Y., Lo, E.I., Chen, L., Forman-Kay, J.D., Raetz, C.R., Prive, G.G., Bishop, R.E. and Kay, L.E. (2002) Solution structure and dynamics of the outer membrane enzyme PagP by NMR. *Proc Natl Acad Sci U S A*, **99**, 13560-13565.

Jain, M.K.a.W., R.C. (1988) Introduction to biological membranes. *2nd ed. New York: Wiley*.

Jung, H. (1998) Topology and function of the Na+/proline transporter of Escherichia coli, a member of the Na+/solute cotransporter family. *Biochim Biophys Acta*, **1365**, 60-64.

Kaesler, B. and Schonheit, P. (1989) The role of sodium ions in methanogenesis. Formaldehyde oxidation to CO2 and 2H2 in methanogenic bacteria is coupled with primary electrogenic Na+ translocation at a stoichiometry of 2-3 Na+/CO2. *Eur J Biochem*, **184**, 223-232.

Karpel, R., Alon, T., Glaser, G., Schuldiner, S. and Padan, E. (1991) Expression of a sodium proton antiporter (NhaA) in Escherichia coli is induced by Na+ and Li+ ions. *J Biol Chem*, **266**, 21753-21759.

Ketchem, R.R., Hu, W. and Cross, T.A. (1993) High-resolution conformation of gramicidin A in a lipid bilayer by solid-state NMR. *Science*, **261**, 1457-1460.

Khademi, S., O'Connell, J., 3rd, Remis, J., Robles-Colmenares, Y., Miercke, L.J. and Stroud, R.M. (2004) Mechanism of ammonia transport by Amt/MEP/Rh: structure of AmtB at 1.35 A. *Science*, **305**, 1587-1594.

Kozachkov, L., Herz, K. and Padan, E. (2007) Functional and structural interactions of the transmembrane domain X of NhaA, Na+/H+ antiporter of Escherichia coli, at physiological pH. *Biochemistry*, **46**, 2419-2430.

Krogh, A., Larsson, B., von Heijne, G. and Sonnhammer, E.L. (2001) Predicting transmembrane protein topology with a hidden Markov model: application to complete genomes. *J Mol Biol*, **305**, 567-580.

Krulwich, T.A., Lewinson, O., Padan, E. and Bibi, E. (2005) Do physiological roles foster persistence of drug/multidrug-efflux transporters? A case study. *Nat Rev Microbiol*, **3**, 566-572.

Kühlbrandt. (1994) Atomic model of plant light-harvesting complex by electron crystallography. *Nature, 367(6464), 614-21.*

Kuo, A., Domene, C., Johnson, L.N., Doyle, D.A. and Venien-Bryan, C. (2005) Two different conformational states of the KirBac3.1 potassium channel revealed by electron crystallography. *Structure,* **13**, 1463-1472.

Loll, P.J. (2003) Membrane protein structural biology: the high throughput challenge. *J Struct Biol*, **142**, 144-153.

Lorenz, H., Hailey, D.W., Wunder, C. and Lippincott-Schwartz, J. (2006) The fluorescence protease protection (FPP) assay to determine protein localization and membrane topology. *Nat Protoc*, **1**, 276-279.

Luckey, M. (2008) Membrane structural biology with biochemical and biophysical foundations. *Cambridge University Press*, 68-101.

Lutcke, H., High, S., Romisch, K., Ashford, A.J. and Dobberstein, B. (1992) The methionine-rich domain of the 54 kDa subunit of signal recognition particle is sufficient for the interaction with signal sequences. *Embo J*, **11**, 1543-1551.

McQuade, D.T., Quinn, M.A., Yu, S.M., Polans, A.S., Krebs, M.P. and Gellman, S.H. (2000) Rigid Amphiphiles for Membrane Protein Manipulation. *Angew Chem Int Ed Engl*, **39**, 758-761.

Medh, J.D. and Weigel, P.H. (1989) Separation of phosphatidylinositols and other phospholipids by two-step one-dimensional thin-layer chromatography. *J Lipid Res*, **30**, 761-764.

Meer, G.V. (2008) Membrane lipids: where they are and how they behave. *Nat Rev Mol Cell Biol*. 9(2): 112-24.

Mentzer, R.M., Jr., Lasley, R.D., Jessel, A. and Karmazyn, M. (2003) Intracellular sodium hydrogen exchange inhibition and clinical myocardial protection. *Ann Thorac Surg*, **75**, S700-708.

Mitchell. (1966) Chemiosmotic coupling in oxidative and photosynthetic phosphorylation. *Biol Rev Camb Philos Soc, 41(3), 445-502.*

Miyazaki, E., Sakaguchi, M., Wakabayashi, S., Shigekawa, M. and Mihara, K. (2001) NHE6 protein possesses a signal peptide destined for endoplasmic reticulum membrane and localizes in secretory organelles of the cell. *J Biol Chem*, **276**, 49221-49227.

Mosser, G. (2001) Two-dimensional crystallogenesis of transmembrane proteins. *Micron*, **32**, 517-540.

Mueckler, M. (1994) Facilitative glucose transporters. *Eur. J. Biochem*, **219**, 713-725.

Murakami, S., Nakashima, R., Yamashita, E. and Yamaguchi, A. (2002) Crystal structure of bacterial multidrug efflux transporter AcrB. *Nature*, **419**, 587-593.

Murata, K., Mitsuoka, K., Hirai, T., Walz, T., Agre, P., Heymann, J.B., Engel, A. and Fujiyoshi, Y. (2000) Structural determinants of water permeation through aquaporin-1. *Nature*, **407**, 599-605.

Nielsen, N., Malmendal, A. and Vosegaard, T. (2004) Techniques and applications of NMR to membrane proteins. *Mol Membr Biol*, **21**, 129-141.

Nilsson, J., Persson, B. and von Heijne, G. (2005) Comparative analysis of amino acid distributions in integral membrane proteins from 107 genomes. *Proteins*, **60**, 606-616.

Olof Emanuelsson1, S.B., Gunnar von Heijne3 & Henrik Nielsen2. (2007) "Locating proteins in the cell using TargetP, SignalP and related tools." *Nature Protocols*, 953-971.

Osborne, M.J., Siddiqui, N., Iannuzzi, P. and Gehring, K. (2004) The solution structure of ChaB, a putative membrane ion antiporter regulator from Escherichia coli. *BMC Struct Biol*, **4**:9.

Ostermeier, C., Iwata, S., Ludwig, B. and Michel, H. (1995) Fv fragment-mediated crystallization of the membrane protein bacterial cytochrome c oxidase. *Nat Struct Biol*, **2**, 842-846.

Overington, J.P., Al-Lazikani, B. and Hopkins, A.L. (2006) How many drug targets are there? *Nat Rev Drug Discov*, **5**, 993-996.

Padan, E. (2004) NhaA of *Escherichia coli*, as a model of a pH-regulated Na$^+$/H$^+$ antiporter. *Biochim Biophysic Act. 2004, 1658(1-2).2-13* .

Padan, E., Maisler, N., Taglicht, D., Karpel, R. and Schuldiner, S. (1989) Deletion of ant in Escherichia coli reveals its function in adaptation to high salinity and an alternative Na+/H+ antiporter system(s). *J Biol Chem*, **264**, 20297-20302.

Padan, E. and Schuldiner, S. (1994) Molecular physiology of Na+/H+ antiporters, key transporters in circulation of Na$^+$ and H$^+$ in cells. *Biochim Biophys Acta*, **1185**, 129-151.

Padan, E., Venturi, M., Gerchman, Y. and Dover, N. (2001) Na(+)/H(+) antiporters. *Biochim Biophys Acta*, **1505**, 144-157.

Padan, E.B., Masahiro Ito, terry A. Krulwich. (2005) Alkaline pH homeostasis in bacteria: new insights. *Biochim. Biophys. Acta*, **1717**, 67–88.

Palsdottir, H. and Hunte, C. (2004) Lipids in membrane protein structures. *Biochim Biophys Acta*, **1666**, 2-18.

Parks, G.D. and Lamb, R.A. (1991) Topology of eukaryotic type II membrane proteins: importance of N-terminal positively charged residues flanking the hydrophobic domain. *Cell*, **64**, 777-787.

Pavel, D. (1998) Comaparative molecular analysis of Na+/H+ exchangers: a unified model for Na+/H+ antiport? *FEBS Letters*, **424**, 1-5.

Pebay-Peyroula, E., Rummel, G., Rosenbusch, J.P. and Landau, E.M.,. (1997) X-ray structure of bacteriorhodopsin at 2.5 Å from microcrystals grown in lipidic cubic phases. *Science*, **277**, 1676-1681.

Pervushin, K., Riek, R., Wider, G. and Wuthrich, K. (1997) Attenuated T2 relaxation by mutual cancellation of dipole-dipole coupling and chemical shift anisotropy

indicates an avenue to NMR structures of very large biological macromolecules in solution. *Proc Natl Acad Sci U S A*, **94**, 12366-12371.

Post RL, S.A., Rosenthal As. (1965) A phosphorylated intermdeiate in adenosine triphosphate-dependent sodium and potassium transport across kidney membranes. *J Biol Chem.*, **240**, 1437-1445.

Rahav-Manor, O., Carmel, O., Karpel, R., Taglicht, D., Glaser, G., Schuldiner, S. and Padan, E. (1992) NhaR, a protein homologous to a family of bacterial regulatory proteins (LysR), regulates nhaA, the sodium proton antiporter gene in Escherichia coli. *J Biol Chem*, **267**, 10433-10438.

Rhinow, D. and Kuhlbrandt, W. (2008) Electron cryo-microscopy of biological specimens on conductive titanium-silicon metal glass films. *Ultramicroscopy*, **108**, 698-705.

Rich, I.N., Worthington-White, D., Garden, O.A. and Musk, P. (2000) Apoptosis of leukemic cells accompanies reduction in intracellular pH after targeted inhibition of the Na($^+$)/H($^+$) exchanger. *Blood*, **95**, 1427-1434.

Roosild, T.P., Greenwald, J., Vega, M., Castronovo, S., Riek, R. and Choe, S. (2005) NMR structure of Mistic, a membrane-integrating protein for membrane protein expression. *Science*, **307**, 1317-1321.

Rothman, A., Gerchman, Y., Padan, E. and Schuldiner, S. (1997) Probing the conformation of NhaA, a Na$^+$/H$^+$ antiporter from Escherichia coli, with trypsin. *Biochemistry*, **36**, 14572-14576.

Rothman, A., Padan, E. and Schuldiner, S. (1996) Topological analysis of NhaA, a Na+/H+ antiporter from Escherichia coli. *J Biol Chem*, **271**, 32288-32292.

Sadava, D. (2008) The Science of Biology, 4th Edition, by Sinauer Associates.

Sandy Y. M. Ng, B.C., David J. VanDyke and Ken F. Jarrell (2007) Archaeal signal peptidases. *Microbiology*, **157**, 305-314.

Sato, T., Sakaguchi, M., Mihara, K. and Omura, T. (1990) The amino-terminal structures that determine topological orientation of cytochrome P-450 in microsomal membrane. *Embo J*, **9**, 2391-2397.

Sato, Y. and Sakaguchi, M. (2005) Topogenic properties of transmembrane segments of Arabidopsis thaliana NHX1 reveal a common topology model of the Na+/H+ exchanger family. *J Biochem*, **138**, 425-431.

Schafer, G., Engelhard, M. and Muller, V. (1999) Bioenergetics of the Archaea. *Microbiol Mol Biol Rev*, **63**, 570-620.

Schmidt-Krey, I. (2007) Electron crystallography of membrane proteins: two-dimensional crystallization and screening by electron microscopy. *Methods*, **41**, 417-426.

Screpanti, E. and Hunte, C. (2007) Discontinuous membrane helices in transport proteins and their correlation with function. *J Struct Biol*, **159**, 261-267.

Skulachev, V.P. (1994) Chemiosmotic concept of the membrane bioenergetics: what is already clear and what is still waiting for elucidation? *J Bioenerg Biomembr*, **26**, 589-598.

Slepkov, E.R., Rainey, J.K., Sykes, B.D. and Fliegel, L. (2007) Structural and functional analysis of the Na+/H+ exchanger. *Biochem J*, **401**, 623-633.

Smith, J.M. (1999) Ximdisp--A visualization tool to aid structure determination from electron microscope images. *J Struct Biol*, **125**, 223-228.

Sobczak, I. and Lolkema, J.S. (2005) Structural and mechanistic diversity of secondary transporters. *Curr Opin Microbiol*, **8**, 161-167.

Speelmans, G., Poolman, B., Abee, T. and Konings, W.N. (1993) Energy transduction in the thermophilic anaerobic bacterium Clostridium fervidus is exclusively coupled to sodium ions. *Proc Natl Acad Sci U S A*, **90**, 7975-7979.

Studier, F.W. (2005) Protein production by auto-induction in high density shaking cultures. *Protein Expr Purif*, **41**, 207-234.

Subramaniam, S., Gerstein, M., Oesterhelt, D. and Henderson, R. (1993) Electron diffraction analysis of structural changes in the photocycle of bacteriorhodopsin. *Embo J*, **12**, 1-8.

Switzer. (1979) A highly sensitive silver stain for detecting proteins and peptides in polyacylamide gels. *Anal Biochem.* 1979, 98(1), 231-7.

Taglicht, D. (1991) Overproduction and purification of a functional Na+/H+ antiporter codes by nhaA (ant) from Escherichia coli. *Journal of Biological chemistry*.

Toyoshima, C., Nakasako, M., Nomura, H. and Ogawa, H. (2000) Crystal structure of the calcium pump of sarcoplasmic reticulum at 2.6 Å resolution. *Nature,* **405**, 647-655.

Tzubery, T., Rimon, A. and Padan, E. (2008) Structure-based functional study reveals multiple roles of transmembrane segment IX and loop VIII-IX in NhaA Na+/H+ antiporter of Escherichia coli at physiological pH. *J Biol Chem*, **283**, 15975-15987.

Unwin, N. (1995) Acetylcholine receptor channel imaged in the open state. *Nature*, **373**, 37-43.

Ussery, D.W., Hinton, J.C., Jordi, B.J., Granum, P.E., Seirafi, A., Stephen, R.J., Tupper, A.E., Berridge, G., Sidebotham, J.M. and Higgins, C.F. (1994) The chromatin-associated protein H-NS. *Biochimie*, **76**, 968-980.

Valpuesta, J.M., Carrascosa, J.L. and Henderson, R. (1994) Analysis of electron microscope images and electron diffraction patterns of thin crystals of phi 29 connectors in ice. *J Mol Biol*, **240**, 281-287.

Venturi, M., Rimon, A., Gerchman, Y., Hunte, C., Padan, E. and Michel, H. (2000) The monoclonal antibody 1F6 identifies a pH-dependent conformational change in the hydrophilic NH(2) terminus of NhaA Na(+)/H(+) antiporter of Escherichia coli. *J Biol Chem*, **275**, 4734-4742.

Vinothkumar, K.R., Smits, S.H. and Kuhlbrandt, W. (2005) pH-induced structural change in a sodium/proton antiporter from Methanococcus jannaschii. *Embo J*, **24**, 2720-2729.

von Heijne, G. (1988) Transcending the impenetrable: How Proteins come to terms with Membranes. *Biochim Biophys Acta*, **974**, 307-333.

Vonck, J. (2000) Structure of the bacteriorhodopsin mutant F219L N intermediate revealed by electron crystallography. *EMBO J*, **19**, 2152-2160.

W. Hilpert, B.S.a.P.D. (1984) Life by a new decarboxylation-dependent energy conservation mechanism with sodium as coupling ion. *EMBO J*, **3**, pp. 1665–1670.

Wakabayashi, S., Pang, T., Su, X. and Shigekawa, M. (2000) A novel topology model of the human Na(+)/H(+) exchanger isoform 1. *J Biol Chem*, **275**, 7942-7949.

Wang. (1997) The Na+/H+ exchanger potentiates growth and retinoic acid induced differntiation of P19 embryonal carcinoma cells. *J Biol Chem*, **272**, 26545-26549.

Wang, D.N. and Kuhlbrandt, W. (1991) High-resolution electron crystallography of light-harvesting chlorophyll a/b-protein complex in three different media. *J Mol Biol*, **217**, 691-699.

Ward, J., Cardoso de Almeida, M.L., Turner, M.J., Etges, R. and Bordier, C.,. (1987) An assay of membrane-bound Trypanosoma brucei phospholipase using an integral membrane protein substrate and detergent phase separation. *Mol. Biochem. Parasitol.*, **23**, 1-7.

West, I.C. and Mitchell, P. (1974) Proton/sodium ion antiport in *Escherichia coli. Biochem J*, **144**, 87-90.

White, S.H. and Wimley, W.C. (1999) Membrane protein folding and stability: physical principles. *Annu Rev Biophys Biomol Struct*, **28**, 319-365.

Williams, K.A. (2000) Three-dimensional structure of the ion-coupled transport protein NhaA. *Nature*, **403**, 112-115.

Williams, K.A., Geldmacher-Kaufer, U., Padan, E., Schuldiner, S. and Kuhlbrandt, W. (1999) Projection structure of NhaA, a secondary transporter from Escherichia coli, at 4.0 A resolution. *EMBO J*, **18**, 3558-3563.

Willis, M.S. and Koth, C.M. (2008) Structural proteomics of membrane proteins: a survey of published techniques and design of a rational high throughput strategy. *Methods Mol Biol*, **426**, 277-295.

Wilson, C.M. (1983) Staining of protein gels: comparisons of dyes and procedures. *Methods Enzymol, 91, 236.*

Y. Fujiyoshi, T.M., K. Morikawa, H. Yamagishi, Y. Aoki, H. Kihara and Y. Harada. (1991) Development of a superfluid helium stage for high-resolution electron microscopy. *Ultramicroscopy*, **38**, 241-251.

Yamashita, A., Singh, S.K., Kawate, T., Jin, Y. and Gouaux, E. (2005) Crystal structure of a bacterial homologue of Na^+/Cl^--dependent neurotransmitter transporters. *Nature*, **437**, 215-223.

Yernool, D., Boudker, O., Jin, Y. and Gouaux, E. (2004) Structure of a glutamate transporter homologue from Pyrococcus horikoshii. *Nature*, **431**, 811-818.

Zhao, F.Q. and Keating, A.F. (2007) Functional properties and genomics of glucose transporters. *Curr Genomics*, **8**, 113-128.

Zhou, Y., Morais-Cabral, J.H., Kaufman, A. and MacKinnon, R. (2001) Chemistry of ion coordination and hydration revealed by a K^+ channel-Fab complex at 2.0 Å resolution. *Nature*, **414**, 43-48.

Abbreviations

2D Two-dimensional

3D Three-dimensional

AHT Anhydrotetracyclin

AI Auto-Induction

ANS 8-Anilino-1-naphthalenesulfonic acid

BSA Bovine Serum Albumin

b-ME 2-mercaptoethanol

BN Blue Native

BP blue Bromophenolblue

C10E6 Polyoxyethylene (6) decyl ether

C12E8 Polyoxyethylene (8) dodecyl ether

CBB Coomassie Brilliant Blue

CCD Charged Couple Device

CD Circular Dichroism

CHAPS [3-[(3-Cholamidopropyl)-dimethylammonio]-1-propane sulfonate

CHAPSO [3-[(3-Cholamidopropyl)dimethylammonio]-2-hydroxyl-

1- propanesulfonate

CMC Critical micelle concentration

CPA Monovalent cation/proton antiporter

CTF Contrast transfer function

CV Column volume

Cryo-EM Cryo Electron microscopy

Cymal 6 n-Cyclohexyl-1-hexyl-b-D-maltoside

DM n-Decyl-b-D-maltoside

DDM n-Dodecyl-b-D-maltoside

DHPC 1,2-Diheptadecanoyl-sn-glycero-3-phosphocholine

DPPC 1,2-Dipalmitoyl-sn-glycero-3-phosphocholine

DAG Diacyl glycerol

EM Electron microscopy

IPTG Isopropyl-b-D-thiogalactopyranoside

IQ IQ 1 indicates a signal more than seven times the background, and IQ 7

indicates a signal equal to background after correction for the background.

IQ = 7 °— [(intensity of noise) / (intensity of signal)].

LB Luria Broth

LDAO n-Dodecyl-N,N-dimethylamine-N-oxide

LPR Lipid to protein ratio

MAS-NMR Magic-Angle Spinning-Nuclear Magnetic Resonance

MFS Major facilitator superfamily

MME Monomethylether

MPD 2-Methyl-2-4-pentanediol

MS Mass spectrometry

NCS Non-crystallographic symmetry

NMR Nuclear magnetic resonance spectroscopy

NG n-Nonyl-b-D-glucopyranoside

OG n-Octyl-b-D-glucopyranoside

PA Phosphatidic acid

PC Phosphatidyl choline

PDB Protein Data Bank

PE Phosphatidyl ethanolamine

PEG Polyethylene glycol

PG Phosphatidyl glycerol

PI Phosphatidyl inositol

POPC 1-Palmitoyl-2-oleoyl-sn-glycero-3-phosphocholine

RT Room temperature

S/N Signal-to-noise ration

SAD Singlewavelength anomalous dispersion

SDS Sodium dodecylsulfate

SOB/SOC

TB Terrific broth

TLC Thin-layer chromatography

TM Transmembrane

TX-100 Triton X-100

Tris Tris -(hydroxymethyl-aminomethan)

WT Wild-type

ZW-3,12 n-dodecyl-N,N-dimethyl-3-amino-1-propanesulfonate

Appendix I: Merging Statistics

	Image	Refined Tilt angle (°)	Resolution limit used for origin refinement(Å)	Phase Residual (IQ 1-4)	Magnification
1	5930*	-1.20	8	13.215	x 70000
2	15930*	0.320	8	11.83	x 70000
3	5283	-0.850	8	14.51	x 53000
4	4540*	-0.516	8	14.99	x 70000
5	14540*	0.356	8	14.19	x 70000
6	4533	2.16	8	15.29	x 70000
7	5289	0.979	8	16.05	x 53000
8	5290	1.378	8	13.03	x 53000
9	5264	-0.465	8	13.44	x 53000
10	5268	0.665	8	11.77	x 53000
11	5927	-1.515	8	14.47	x 70000
12	15927	0.487	8	11.87	x 70000
13	4534	-2.477	8	11.94	x 70000
14	6424*	4.539	8	14.22	x 70000
15	16424*	-2.703	8	12.70	x 70000
16	15970	8.960	8	19.25	x 70000
17	5961	11.044	8	15.13	x 70000
18	15972	-10.829	8	18.45	x 70000
19	4910	9.650	8	16.69	x 70000
20	5948	-6.955	8	13.83	x 70000
21	5949	-8.227	8	12.44	x 70000
22	5966	-10.44	8	15.49	x 70000
23	5964	-11.278	8	13.44	x 70000
24	5951	-9.448	8	13.61	x 70000

25	5730	22.97	8	14.99	x 70000
26	5944	-20.533	8	14.91	x 70000
27	5978	-24.584	8	15.11	x 70000
28	5984	-13.744	8	14.57	x 70000
29	5971	-11.60	8	16.73	x 70000
30	5246*	-26.26	8	17.82	x 70000
31	15246*	-27.64	8	15.63	x 70000
32	5255*	-35.01	8	13.37	x 70000
33	15255*	-35.872	8	16.22	x 70000
34	5987	3615	8	21.49	x 70000
35	5249*	27.14	8	17.14	x 70000
36	15249*	28.56	8	18.03	x 70000
37	5252	26.70	8	14.60	x 70000
38	5258*	35.66	8	13.11	x 70000
39	15258*	33.43	8	13.92	x 70000
40	5257	33.996	8	13.92	x 70000
41	5259*	35.78	8	17.03	x 70000
42	15259*	31.69	8	16.29	x 70000
43	5753*	32.22	8	16.74	x 70000
44	15753*	-31.56	8	18.66	x 70000
45	6025	-37.48	8	18.12	x 70000
46	5775	-32.30	8	22.52	x 70000
47	7813	-46.48	8	14.18	x 70000
48	78311*	52.20	8	17.84	x 70000
49	178311*	52.80	8	9.33	x 70000
50	7830*	47.91	8	11.09	x 70000
51	17830*	46.11	8	13.06	x 70000

52	7835*	-44.33	8	19.42	x 70000
53	17835*	43.01	8	14.68	x 70000
54	19832	52.91	8	15.38	x 70000
55	9825	-55.30	8	22.61	x 70000
56	9838	-49.28	8	14.03	x 70000
57	9468	-40.89	8	18.66	x 70000
58	19484	-48.50	8	15.43	x 70000
59	19469	-48.69	8	21.62	x 70000
60	7816	43.67	8	20.43	x 70000
61	7826	50.74	8	13.59	x 70000
62	7805	44.76	8	17.56	x 70000
63	7828	-37.54	8	16.91	x 70000
64	19500*	-46.88	8	23.54	x 70000
65	9500*	-53.29	8	23.37	x 70000
66	9832	-49.11	8	19.13	x 70000
67	17806	37.69	8	17.10	x 70000
68	9829	37.14	8	24.75	x 70000
69	9455	-54.76	8	11.60	x 70000
70	9483	-46.59	8	17.98	x 70000
71	9837	43.03	8	15.96	x 70000
72	19847*	-43.85	8	12.73	x 70000
73	29847*	38.03	8	16.31	x 70000
74	9496	-45.925	8	24.37	x 70000

*Images where both lattices were processed and included for the 3D map caluclation.

Appendix II: Gel filtration profile
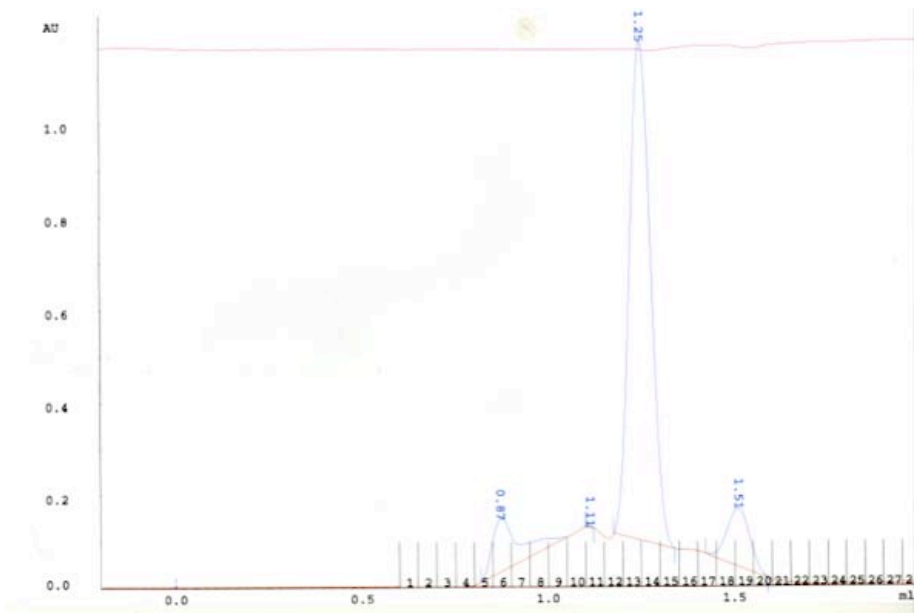
Cymal 5
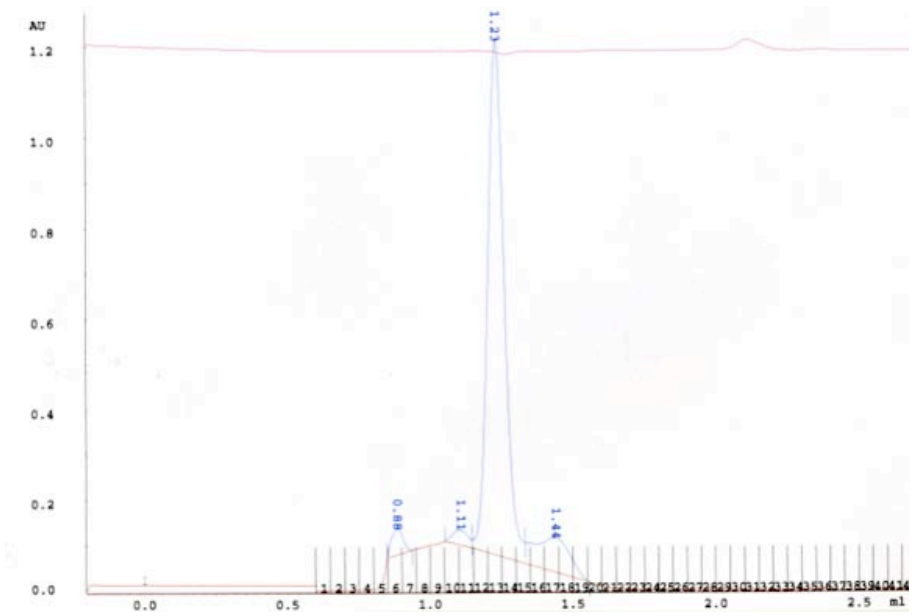
Cymal 7
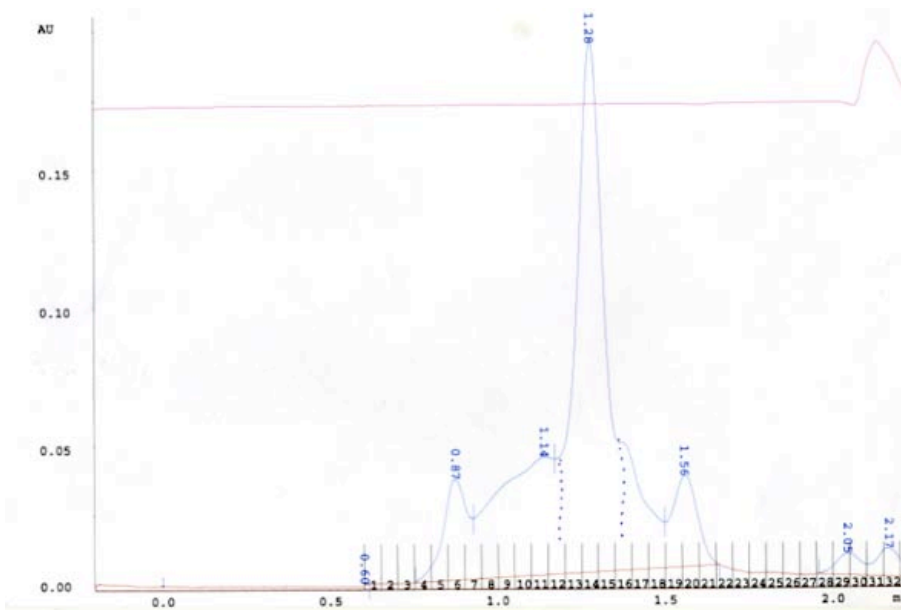
Decyl maltoside (DM)
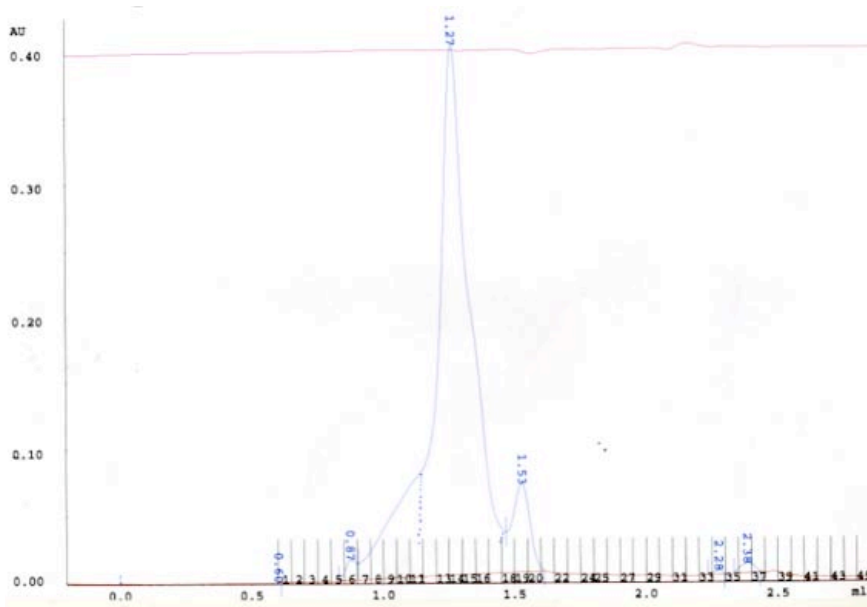
Undecyl maltoside (UDM)

Gel filtration profile of MjNhaP1 applied on a calibrated Superdex 200 column eluted in pH4 buffer. Total volume of the column is 3ml and the void volume is 0.8ml. The analysis was carried out to check for stability of the protein in different detergents. The results show that NhaP1 is more stable in maltoside detergents at pH4.0. 2-3 x cmc values of the detergents were used in the buffer for the gel filtration.

Curriculum Vitae

Panchali Goswami

Born 14th August 1977 in Dibrugarh (India)

Educational Qualifications

Masters of science (M.Sc. Molecular Biology and Biotechnology), July 2000 – 2002

Tezpur University, Assam, India

Dissertation work: Institute of Microbial Technology (Imtech), Chandigarh, India

Bachelor of science (B.Sc.), March 1997 - April 2000, Gauhati University, Assam, India

Professional Experience

Trainee-research associate (Feb 2003-Dec 2003)- Unichem Laboratories Ltd, Bangalore, India

Important Conferences/ Workshops Experiences

1) Participated in the EMBO workshop on "Cryo-electron microscopy" in EMBL Heidelberg, Aug2006

2) Participated in the master class for " Systems approaches to membrane proteins" organized by EMBN-Train, MPSi & E-MeP-Lab. March 2007, in Leeds, UK.

3) Poster and oral presentation at the Gordon Research Conference on 3D electron microscopy, June 15-20, 2008, Lucca (Barga), Italy

Awards and Scholarships

1.Tezpur University Gold Medal for securing highest grade point in M.Sc final examination in the Dept. of Molecular Biology& Biotechnology for the year 2002.

2.Prime Minister of India's invitee to the Republic day parade for excellent academic performance in the year 2001

3. Department of Biotechnology, India Merit Scholarship 2000

4.North-eastern Council Merit scholarship 2001-2002

5. Assam State merit Scholarship 1994-1996

List of Publications

1.Kedrov A, Wegmann S, Smits SH, **Goswami P**, Baumann H, Muller DJ.

Detecting molecular interactions that stabilize, activate and guide ligand-binding of the sodium/proton antiporter MjNhaP1 from Methanococcus jannaschii.

J Struct Biol. 2007 Mar 12;

2: Yildiz O, Vinothkumar KR, **Goswami P**, Kühlbrandt W.

Structure of the monomeric outer-membrane porin OmpG in the open and closed conformation.

EMBO J. 2006 Aug 9;25(15):3702-13.

3.**Goswami P**, Vonck J, Hizlan D, Yildiz Ö, Kühlbrandt W et al. Three-dimensional structure of NhaP1 from *Methanococcus jannaschii* reveals common motifs of monovalent cation-proton antiporters (Manuscript in preparation)

4. E. Dafic, O. Klein, **P. Goswami**, W. Kühlbrandt, W. Mäntele. Infrared spectroscopic study of the structural and functional properties of the Na+ /H+ antiporter MjNhaP1 from *Methanococcus jannaschii* (manuscript submitted)

Acknowledgemets

Frankfurt would'nt have been wonderful without Shweta. She had seen me through thick and thin, helped me with my work and together we had discovered Europe.

Being a part of Asha-Frankfurt chapter I got a chance to work for my country, which was a diversion from a stressful work schedule. Through "Asha" I have acquired friends like Kasturi, Parotish, Sandeep and Sanket. They have always been there, in good as well as bad times.

My husband Siddhartha has given me immense support and had been very understanding all throughout. I owe a lot to my Parents and my brother (Rup) and sister (Jina) for their encouraging words.

I consider myself very lucky for the support I had received from my teachers all throughout for my career. I would like to take this opportunity to thank Madhab Talukdar, Dr. Partha Baruah, Dr. Alak Buragohain. Dr. Bhaskarjyoti Sharma, Dr. Asish Mukherjee and Dr. Suvendra Ray.

My days in Unichem laboratory Ltd. helped me in my scientific venture and I thank all my ex-colleagues for it.

Without Dr. Ramadoss I would'nt have been able to come this far. I still and forever will consider him to be my Godfather in science.

Last and not least I thank my grandmother who made me realize the importance of education. She has herself completed her studies under extreme difficulty. Putting her needs aside she had helped me in all education related issues. I dedicate my thesis to her, as I know this would have been her greatest gift had she been alive.